Optical Properties of Low-Dimensional Semiconductor Nanostructures under High Pressure

J. S. Reparaz

Director: Prof. A. R. Goñi
Co-director: Dr. M. I. Alonso
Tutor: Prof. Javier Rodriguez-Viejo

Tesis Doctoral

Departamento de Física
Universidad Autónoma de Barcelona - ICMAB

October 7, 2008

A mi Padre... a quien extraño cada día de mi vida.

Abstract

In this work, the optical and vibrational properties of low dimensional semiconductor systems have been studied by means of Raman spectroscopy and photoluminescence experiments in a diamond anvil pressure cell. The investigated systems can be classified into three groups: SiGe alloys, Ge/Si quantum dots, and CdSe/ZnCdMgSe quantum dots.

The vibrational properties of $Si_{1-x}Ge_x$ alloys have been studied by measuring the compositional dependence of their optical-phonon deformation potentials ($\tilde{K}_{11}$ and $\tilde{K}_{12}$). For this purpose SiGe/Si(100) strained layers were grown by molecular beam epitaxy and characterized combining Raman scattering with the high pressure technique. From these determined parameters it is possible to compute widely used quantities such as the *strain-shift coefficient* or the *Grüneisen parameter* in the whole compositional range. The main advantage of this method is that it is independent of the studied material system, providing a solution to determine the deformation potentials in alloys.

The strain status of self-assembled Ge/Si dots as a function of Si cap layer thickness was investigated measuring their phonon pressure coefficient. A biaxial to hydrostatic strain status transition was found for the dots, as the cap layer thickness increases. This result provides a guide for a correct choice of the strain tensor in quantum dot systems.

The built-in strain in CdSe/ZnCdMgSe dots was also studied using Raman scattering. It was possible to estimate its contribution to the fundamental emission of the dots relative to quantum confinement effects. Interdiffusion of Mg from the barrier to the dots was also observed in resonant conditions, which were achieved using the high pressure technique.

The high pressure measurements combined with Raman spectroscopy have proved to be very useful techniques to study low dimensional semiconductor structures. The results obtained in this work are not only original from a fundamental perspective but also from an experimental point of view, since the present combination of these techniques provides an ingenious alternative to determine physical properties that would be rather complicated to study using other methods.

Contents

Chapter 1

Theoretical Background

1.1 Band Structure and Phonons in Semiconductors

1.1.1 Band Structure

The detailed study of the electronic band structure is the key to understand the behavior of the electrons in solids, as well as their interaction with the lattice vibrations (phonons). The properties of a solid containing of the order of 10^{23} atoms/cm^3 are very complicated to predict. Several approaches to solve this problem were followed in the past providing a great amount of work in this field. For example, calculations of the band structure were performed using methods as $k \cdot p$, tight binding or LCAO, pseudo-potentials, etc.

In this section a simple basic frame to understand the electronic and vibrational properties of semiconductors will be presented. It is not the author's purpose to give a detailed derivation of the fundamental equations governing the band structure, but to present the main ideas to understand the physical origin of the electronic band structure, phonon dispersion relations, and electron-phonon interaction, responsible, for instance, for the Raman effect.

First we write the Hamiltonian describing a perfect crystal as:

$$\mathcal{H} = \sum_i \frac{p_i^2}{2m_i} + \sum_j \frac{P_j^2}{2M_j} + \frac{1}{2}\sum_{j'j}^{-} \frac{Z_j Z_{j'} e^2}{4\pi\varepsilon_0 |R_j - R_{j'}|} - \sum_{ji} \frac{Z_j e^2}{4\pi\varepsilon_0 |r_i - R_j|} + \frac{1}{2}\sum_{ij}^{-} \frac{e^2}{4\pi\varepsilon_0 |r_i - r_j|}, \tag{1.1}$$

where r_i is the position of the ith electron, R_j the position of the jth nucleus, Z is the atomic number of the nucleus, p_i and P_j are the momentum operators of the electron and nucleus, respectively, e is the electronic charge, and $\bar{\sum}$ means that the summation is only over pairs of indices which are not identical. This many particle Hamiltonian cannot be solved without a large list of simplifications:

- **Valence electron approximation**

  In the valence electron approximation we reduce the number of electrons in the problem by taking into account only the valence electrons, neglecting the core electrons. We will take advantage from the fact that the core electrons are tightly bound to the nucleus forming the so-called *ion core*. Thus, the core electrons will no longer appear explicitly. For example, in the case of Si the electronic structure can be written as $[1s^2][2s^2 2p^6]3s^2 3p^2$, where the 3s and 3p electrons are the only ones that should be taken into account.

- **Born-Oppenheimer or adiabatic approximation**

  This approximation relies on the fact that ions are much heavier than electrons so they move much slowly. Typically, the energy scales involved in the ionic motion is of the order of tens of meV, whereas the excitation energies for electrons is of the order of 1 eV. Converting these values to frequencies we obtain 10^{13} s^{-1} and 10^{15} s^{-1} for lattice and electron vibrations, respectively. That is, the electronic frequencies are two orders of magnitude larger than the ionic vibrations, therefore the electrons *see* the ions essentially stationary. Based on this, we rewrite the Hamiltonian in Eq. (1.1) decoupling in part the movement of the electrons from that of the lattice as:

  $$\mathcal{H} = \mathcal{H}_{ions}(R_j) + \mathcal{H}_e(r_i, R_{j0}) + \mathcal{H}_{e-ion}(r_i, \delta R_j), \tag{1.2}$$

  where $\mathcal{H}_{ions}(R_j)$ is the Hamiltonian describing the ionic motion under the influence of the ionic potentials plus the time averaged electronic potentials, $\mathcal{H}_e(r_i, R_{j0})$ is the Hamiltonian for the electrons with the ions in their equilibrium positions R_{j0}, and $\mathcal{H}_{e-ion}(r_i, \delta R_j)$ describes the changes in the electronic energies as a result of the displacements δR_j of the ions from their equilibrium positions.

  The purely electronic contribution to the Hamiltonian in (1.2), $\mathcal{H}_e(r_i, R_{j0})$, is the one responsible for the electronic excitation spectra in semiconductors, but still another approximation must be done in order to deal with the problem.

- **Mean Field approximation**

  Taking only the electronic part in (1.2), we rewrite it as follows:

$$\mathcal{H}_e = \sum_i \frac{p_i^2}{2m_i} + \frac{1}{2}\sum_{i,i'}^{-} \frac{e^2}{4\pi\varepsilon_0 \left|r_i - r_{i'}\right|} - \sum_{i,j} \frac{Z_j e^2}{4\pi\varepsilon_0 \left|r_i - R_{j0}\right|}, \quad (1.3)$$

  where the first term is the kinetic energy of the electrons, the second is the Coulomb repulsion between electrons, and the last term is the Coulomb attraction between the nucleus in their equilibrium positions and the electrons. This Hamiltonian is still difficult to solve since $\sim 10^{23}$ electrons are present in the solid. The *mean field* approximation replaces the Coulombian terms in (1.3) by an average potential. The resulting Hamiltonian is given by:

$$\mathcal{H}_e = \sum_i \left[\frac{p_i^2}{2m_i} + V(r_i)\right] \Longrightarrow \mathcal{H}_{1e} = \frac{p^2}{2m} + V(r), \quad (1.4)$$

  where $\mathcal{H}_{1e}$ is the one electron Hamiltonian and $V(r)$ is the average potential. The first term in (1.4) is the free electron Hamiltonian with plane waves as solutions. The energy spectrum is described by a parabolic dispersion relation as $E = \frac{\hbar^2 k^2}{2m}$. The presence of the potential V(r) gives rise to the opening of the gap, and to the typical band structure of semiconductors. In order to obtain quantitative results, the one electron potential $V(r)$ is obtained, for example, using *first principle* calculations or *semi-empirical* methods.

The last step to obtain the band structure is to take into account the rotational and translational symmetry of the crystalline structure. In this way, the wave functions that are solutions of (1.4) must have the same symmetry than the crystalline structure. By using group theory it is possible to obtain these symmetries for each lattice structure and, thus, for the wave functions. Fig. 1.1 shows the calculated band structure for Si and Ge in some highly symmetric directions of the Brillouin zone. As observed in the figure, the band structure of these two materials is indirect since the minimum transition energy is not at the zone center but in the $\Gamma \rightarrow X$ direction in Si, and $\Gamma \rightarrow$ L in Ge. This transition is known as the indirect band gap, resulting in ~ 1.1 and ~ 0.7 eV for Si and Ge, respectively.

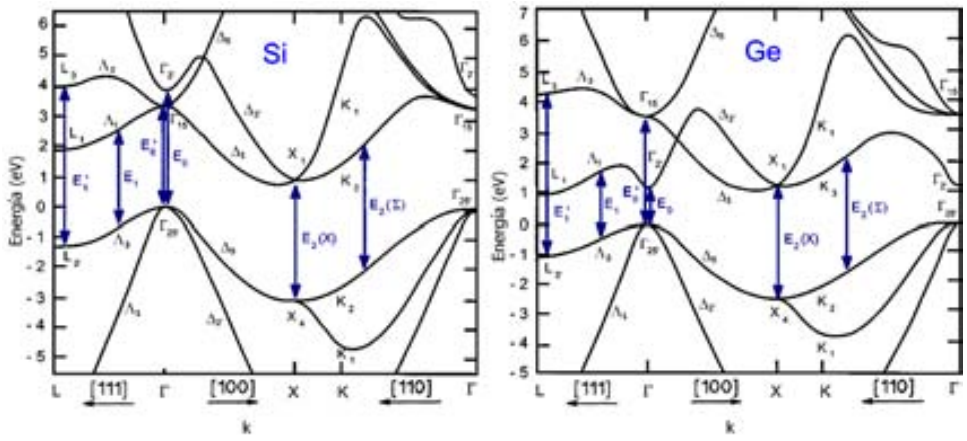

Figure 1.1: Left: Calculated Si band structure for high symmetry lines in the Brillouin zone. Right: Idem for Ge. In both cases the minimum excitation energy (gap) is not in the zone center (Γ point), but in the $\Gamma \rightarrow$ X direction for Si, and $\Gamma \rightarrow$ L for Ge.

1.1.2 Phonons in Semiconductors

It is also relevant for this work to consider the first term of the Hamiltonian (1.2) which describes the nuclear motions. We will only take into account the valence electrons since we assume that the core electrons are rigidly attached to the nucleus.

$$\mathcal{H}_{ion}(R_1, ..., R_n) = \sum_j \frac{P_j}{2M_j} + \sum_{j,j'}^{-} \frac{1}{2} \frac{Z_j Z_{j'} e^2}{4\pi\varepsilon \left|R_j - R_{j'}\right|} - \sum_{i,j} \frac{Z_j e^2}{4\pi\varepsilon \left|r_i - R_j\right|} \tag{1.5}$$

It is difficult to solve the Hamiltonian (1.5) since the movement of the ions is coupled to that of the valence electrons. Although nowadays the electronic part can be calculated with help of computers, the analytical approach to solve the problem is to rewrite the Hamiltonian as $\mathcal{H}_{ion} = \mathcal{H}_0(R_{10}, ..., R_{n0}) + \mathcal{H}'(\delta R_{10}, ..., \delta R_{n0})$, treating the electronic part as a perturbation. Staying at the first order in the perturbed Hamiltonian, that is, taking the quadratic term in the energy, is known as **harmonic approximation**. Higher order terms leading to thermal expansion or phonon annihilation cannot be explained within this approximation, nevertheless it is suitable for obtaining the phonon dispersion curves.

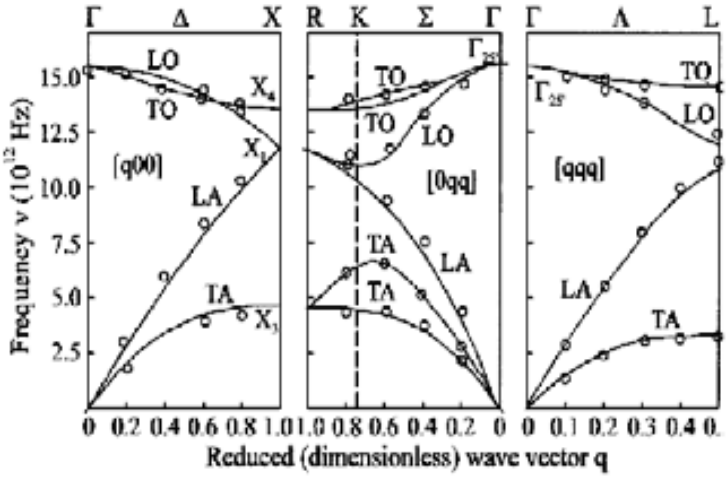

Figure 1.2: Calculated phonon dispersion relations for Si. Since the diamond structure has two atoms per primitive cell, six phonon branches (three acoustical and three optical) are obtained. At the zone center (q=0) the LO and TO vibrations are degenerated due to the non-polar nature of the bondings.

Phonon dispersion curves along high-symmetry directions can be measured by inelastic neutron scattering or high resolution x-ray inelastic scattering. Figure 1.2 shows the phonon dispersion curves for Si. Since for diamond and zinc-blende type lattices there are two atoms per unit cell, hence, there are six phonon branches: three acoustical (A, lower energy curves), and three optical modes (O). Along high-symmetry directions such as the [100] or [111], the phonons can be classified as transverse (T) or longitudinal (L), according to whether their displacements are perpendicular or parallel to the direction of the wave vector **q**. For the acoustic branches the velocities of these sound waves are determined by the shear modulus for the TA branch and by the bulk elastic modulus for the LA branch. Since it is easier to shear a solid than to compress it, the TA branch is lower in energy than the LA. The optical branches (TO, LO) are degenerated at the zone center due to the non-polar nature of the Si bondings, in contrast to the III-V compounds for which a splitting between these two modes exists due to the polar nature of the bonds.

1.1.3 Electron-Phonon Interaction

Until now we have described separately the motion of the electrons [$\mathcal{H}_e$, see Eq. (1.2)] and ions ($\mathcal{H}_{ion}$) within the Born-Oppenheimer approximation, but a description of the electron-phonon interaction is still lacking ($\mathcal{H}_{e-ion}$). Within the spirit of this approximation we assume that the electrons can follow the ions almost instantaneously, so that the electron-phonon interaction can be expanded as a Taylor series in the ions displacements δR_j as:

$$\mathcal{H}_{e-ion}(r_i, \delta r_j) = \sum_j \left(\frac{\partial \mathcal{H}_e}{\partial R_j}\right)\Bigg|_{R_{j0}} \cdot \delta R_j \tag{1.6}$$

Usually the electronic Hamiltonian $\mathcal{H}_e$ is not known. In this work we shall consider the vibrations in diamond or zinc-blende structures with two atoms per unit cell. As we have discussed before, these vibrations can be grouped in four types: LA, TA, LO, and TO phonons.

Considering the physical properties studied in this work, we will consider electron-phonon interaction of two types:
i) Deformation potential interaction is present in crystals with two or more atoms per primitive cell, a long-wavelength optical phonon involves relative displacements of atoms within the primitive unit cell leading to a change in the electronic energies. We can write this interaction as

$$\mathcal{H}_{e-OP} = D_{n,k} \cdot \frac{\mathbf{u}}{a_0}, \tag{1.7}$$

where $D_{n,k}$ is the optical phonon deformation potential for the energy band indexed by n and k. Since the this interaction does not depend on the phonon wavevector it is a *short range* interaction: the Fourier transform of a function of long range in $\mathbf{q}$ is of short range in $\mathbf{r}$ and vice versa.

ii) The **Fröhlich** interaction develops in polar crystals with at least two atoms per primitive cell. The LO phonon induces an oscillating macroscopic polarization, leading to an electric field E_{LO}. This interaction is not present in Si or Ge since they are not polar, whereas it is mostly responsible for the electron-phonon coupling in III-V or II-VI semiconductors like GaAs, AlAs, CdSe, ZnSe, etc.

1.2 Interaction between Light and Matter

We have splitted the general Hamiltonian (1.2) into three contributions arising from the electrons, phonons, and from the electron-phonon interaction.

By studying these contributions independently, we have described the electronic excitation spectra, the phonon dispersion curves, and the different types of electron-phonon interaction. In this section, the interaction between light and matter will be presented in order to understand the phenomena that occur when exciting a semiconductor with electromagnetic radiation. The previous derivation starting from the Hamiltonian will not be followed for the sake of simplicity. Nevertheless, it is worth to mention that if light has to be included in the description of Hamiltonian (1.2) we would have to make two main modifications:

- $\mathbf{p} \rightarrow \mathbf{p} - \frac{e}{c}\mathbf{A}$, where $\mathbf{p}$ is the momentum operator of each particle, $\mathbf{A}$ is the potential vector of the electromagnetic field, e the electron charge, and c the speed of light. This modification in the momentum is due to the presence of an electromagnetic field and gives rise to an interaction between the e.m. field and the particles.

- We should also add a term of the form $e\phi$ to the Hamiltonian, representing the interaction between the charged particles and the electric field.

The constitutive equations provide a way to describe the interaction between light and matter. In their macroscopic form these equations describe this interaction via the susceptibility:

$$P = \epsilon_0 \chi E, \tag{1.8}$$

where ϵ_0 is the electrical susceptibility of the vacuum, P is the polarization of the medium, χ is the susceptibility, and E is the applied electric field.

This equation shows that when light traveling in vacuum finds a region of space containing matter (i.e. $\epsilon \neq \epsilon_0$), the atoms will react to the incident e.m. field by creating a polarization field via the susceptibility (χ). This will produce scattering of the incident e.m. field, which can be elastic and/or inelastic. As an example, absorption of light by materials is no other than an extreme case of light scattering. The most usual scattering processes are divided into these two groups:

- **Elastic scattering**: Rayleigh and Mie. The differences between these two is the wavelength involved, being the one by Rayleigh the appropriate for describing scattering at small wavelengths

- **Inelastic scattering**: Raman, Brillouin, Compton. Raman and Brillouin scattering reefers to scattering of light by optical and acoustic phonons, respectively. Compton scattering is the scattering of X-Rays by electrons.

Since we will be mainly concerned with Raman scattering, I will not describe the other types of scattering. Consider a medium with susceptibility χ, and an incident plane electromagnetic wave as:

$$E(r,t) = E_i(k_i,\omega_i)cos(k_i \cdot r - \omega_i t) \tag{1.9}$$

When an e.m. field is present in the medium this reacts creating a polarization field with the same frequency and wavevector of the incident wave. In addition, if the sample is at a finite temperature the vibrations of the atoms (phonons) will produce fluctuations on χ. The resulting response of the medium will be given by Eq. (1.8). Taking into account that the atomic displacements (Q) are small, we can expand the susceptibility as:

$$\chi(k_i,\omega_i,Q) = \chi_0(k_i,\omega_i) + (\partial\chi/\partial Q)_0 Q(r,t) + ..., \tag{1.10}$$

using Eq. (1.8) and the incident wave in (1.9) we obtain for the polarization the following expression:

$$P(r,t,Q) = P_0(r,t) + P_{ind}(r,t,Q), \tag{1.11}$$

where $P_0(r,t)$ is the contribution arising from the response of the medium with no phonons present and $P_{ind}(r,t,Q)$ is the contribution of phonons:

$$P_0(r,t) = \epsilon_0\chi_0(k_i,\omega_i) \cdot E_i(k_i,\omega_i)cos(k_i \cdot r - \omega_i t) \tag{1.12}$$

$$P_{ind}(r,t,Q) = (\partial\chi/\partial Q)_0 Q(r,t) \cdot E_i(k_i,\omega_i)cos(k_i \cdot r - \omega_i t) \tag{1.13}$$

Finally, assuming that the atomic displacements associated with a phonon can be expressed as planes waves:

$$Q(r,t) = Q(q,\omega_0)cos(q \cdot r - \omega_0 t), \tag{1.14}$$

and introducing this dependence into Eq. (1.13) we rewrite P_{ind} to determine its frequency and wavevector obtaining:

$$\begin{aligned} P_{ind}(r,t,Q) = \frac{1}{2}(\partial\chi/\partial Q)_0 Q(q,\omega_0)F_i(k_i,\omega_i t) \\ \times\{cos[(k_i+q)\cdot r - (\omega_i+\omega_0)t] \\ +cos[(k_i-q)\cdot r - (\omega_i-\omega_0)t]\} \end{aligned} \tag{1.15}$$

This induced polarization consists of two sinusoidal waves: a *Stokes* component with wavevector $k_S = k_i - q$ and frequency $\omega_S = \omega_i - \omega_0$, and an *anti-Stokes* component with wavevector $k_S = k_i + q$ and frequency $\omega_S = \omega_i + \omega_0$.

Notice that both frequency and wavevector are conserved in the Raman process, so that the wavevector of the one phonon Raman process must be approximately twice the wavevector of the incident light. Considering visible light we have $2k_i \approx 10^5 \mathrm{cm}^{-1}$, which corresponds to about 1/100 of the Brillouin zone in a typical semiconductor. Hence, one phonon Raman scattering probes only the zone center phonons. Notice that we can obtain high-order processes like two-phonon Raman scattering by expanding (1.10) to higher orders.

In order to obtain the scattered intensity we calculate the time-averaged scattered polarization $P_{ind}(r,t,Q)$ in Eq. (1.13). After some calculation we arrive to the following expression:

$$I_s \propto |e_i \cdot \Re \cdot e_s| \tag{1.16}$$

where I_s is scattered intensity, e_i and e_s are the incident and scattered polarization directions, and $\Re$ is the Raman tensor. The Raman tensor properties are closely related to the symmetry operations of the crystal, which determine the transitions that are allowed or forbidden, i.e., the so-called Raman selection rules.

Finally, it is worth to present the complete result for the Raman transition probability since effects like resonant-Raman scattering are not obtained in the previous formulation. The complete result to third order in perturbation theory obtained using Feynman diagrams is as follows:

$$\begin{aligned} P_{ph} = \left(\frac{2\pi}{\hbar}\right) \Bigg| \sum_{n,n'} \frac{\langle i|\mathcal{H}_{eR}|n'\rangle\langle n'|\mathcal{H}_{e-ion}|n\rangle\langle n|\mathcal{H}_{eR}|i\rangle}{[\hbar\omega_i - (E_n - E_i)][\hbar\omega_i - \hbar\omega_0 - (E_{n'} - E_i)]} \Bigg|^2 \\ \times \delta[\hbar\omega_i - \hbar\omega_0 - \hbar\omega_s], \end{aligned} \tag{1.17}$$

where $\langle i|$ is the initial state, and $\langle n|$, $\langle n'|$ are intermediate states. $\mathcal{H}_{eR}$ is the Hamiltonian of the electron-radiation interaction, $\mathcal{H}_{e-ion}$ is the electron-phonon Hamiltonian, E_j is the energy of the $\langle j|$ state. The frequencies of the incident and scattered wave and phonon are denoted as ω_i, ω_s, and ω_0, respectively.

Under resonant conditions the contribution from the non-resonant states can be regarded as constant. Taking only the strongest term in the Feynman diagrams we arrive to the following expression for the case of resonant excitation:

$$P_{ph} \approx \left(\frac{2\pi}{\hbar}\right) \left| \frac{\langle 0|\mathcal{H}_{eR}(\omega_i)|a\rangle\langle a|\mathcal{H}_{e-ion}|a\rangle\langle a|\mathcal{H}_{eR}(\omega_s)|0\rangle}{(E_a - \hbar\omega_i)(E_a - \hbar\omega_s)} + C \right|^2 \tag{1.18}$$

where E_a is the energy of an intermediate state denoted by $\langle a|$, and C is a constant arising from the non-resonant states. From this simplification it is possible to observe two important and limiting cases of enhanced P_{ph} that correspond to $E_a = \hbar\omega_i$ and $E_a = \hbar\omega_s$, known as **incoming** and **outgoing** resonance, respectively. This happens when the intermediate state energy coincides with a real energy state of the semiconductor plus/minus the energy of the involved phonon.

1.3 Strain Effects in Semiconductors

In this section the effect of strain in the band structure of semiconductors and, consequently, in their optical properties will be described. In a simple picture, a stress applied to a solid leads to a displacement of the atoms from their equilibrium positions, i.e. a phonon may be represented by a *strain wave* throughout the solid. To obtain the shift in the electronic energies due to the presence of a strain we will consider the gradient of the atomic displacements:

$$d_{ij} = \frac{\partial(\delta R_i)}{\partial R_j}, \tag{1.19}$$

the purely symmetric part of this quantity is known as **strain tensor** and represents the change in the inter-atomic distances when applying a stress to the crystal. If we decompose this tensor into a symmetric and anti-symmetric components we obtain the following two tensors:

$$\epsilon_{ij} = \frac{1}{2}\left(\frac{\partial\delta R_i}{\partial R_j} + \frac{\partial\delta R_j}{\partial R_i}\right), f_{ij} = \frac{1}{2}\left(\frac{\partial\delta R_i}{\partial R_j} - \frac{\partial\delta R_j}{\partial R_i}\right), \tag{1.20}$$

where e_{ij} is the **strain tensor** and f_{ij} is a pure rotation of the crystal. The strain tensor represents a deformation of the solid changing, consequently, the electronic energies in contrast to the anti-symmetric part f_{ij} that does not change the electronic energies, since it represents a pure rotation of the crystal. For the zinc-blende structure it can be shown using group theory that the strain tensor ϵ_{ij} can be decomposed into the sum of three linearly independent matrices which are the basis of every possible deformation:

$$\mathbf{M}^{hyd} = \frac{1}{3}\begin{bmatrix} \epsilon_{11}+\epsilon_{22}+\epsilon_{33} & 0 & 0 \\ 0 & \epsilon_{11}+\epsilon_{22}+\epsilon_{33} & 0 \\ 0 & 0 & \epsilon_{11}+\epsilon_{22}+\epsilon_{33} \end{bmatrix}$$

$$\mathbf{M}^{[100]} = \frac{1}{3}\begin{bmatrix} 2\epsilon_{11}-(\epsilon_{22}+\epsilon_{33}) & 0 & 0 \\ 0 & 2\epsilon_{22}-(\epsilon_{11}+\epsilon_{33}) & 0 \\ 0 & 0 & 2\epsilon_{33}-(\epsilon_{11}+\epsilon_{22}) \end{bmatrix}$$

$$\mathbf{M}^{[111]} = \begin{bmatrix} 0 & \epsilon_{12} & \epsilon_{13} \\ \epsilon_{12} & 0 & \epsilon_{23} \\ \epsilon_{13} & \epsilon_{23} & 0 \end{bmatrix} \tag{1.21}$$

The matrix $\mathbf{M}^{hyd}$ has a nonzero trace and from the definition of the strain tensor components in (1.20) it follows that its trace is equal to the relative volume change $\Delta V/V$ associated with a certain strain. The traceless strain matrices $\mathbf{M}^{[001]}$ and $\mathbf{M}^{[111]}$ describe a shear of the crystal produced by uniaxial stress along the [001] and [111] directions, respectively. As a consequence, three deformation potentials are required to describe the effects of a general strain on a band extremum.

For the description of the effect of strain on the electronic properties of semiconductors Bardeen and Shockley introduced the concept of the deformation potentials. These deformation potentials were introduced in the context of the electron-phonon coupling between long-wavelength ($q = 0$) acoustic phonons and the valence electrons but their definition has general validity. A pure hydrostatic strain which is applied, for example in high pressure experiments with a diamond anvil cell, shifts the electronic states but does not split them. The linear components of these shifts are represented by the volume deformation potential a_i in (eV) defined as:

$$a_i = \frac{dE_i}{d(lnV)} = \frac{\Delta E_i}{tr(\epsilon)}, \tag{1.22}$$

where E_i denotes the energy of state i and V the volume of the crystal. Instead of the hydrostatic deformation potential one often finds in the literature the corresponding pressure coefficient dE_i/dP which is related to the deformation potential through the bulk modulus B:

$$a_i = B \cdot \frac{dE_i}{dP} \tag{1.23}$$

Absolute values for a_i are difficult to obtain experimentally, as usually only the pressure dependence of gaps are measured, which yields only the relative deformation potential between the bands. Typically, the pressure

coefficient of the direct band gap at the Γ point of III-V compounds is of the order of +100 meV/GPa. For the indirect band gap $\Gamma - X$ it is about an order of magnitude smaller and negative in sign (-10 meV/GPa) and for the indirect $\Gamma - L$ gap it is about +50 meV/GPa. Thus, at some pressure the X valley become the lowest conduction band (direct-to-indirect crossover), for example, in bulk GaAs this crossing occurs around 4 GPa.

In contrast to the hydrostatic case, when a uniaxial strain is applied to a crystal (or sub-crystal as 2D layer) its symmetry is reduced. In some cases this leads to a splitting of degenerated states. Pikus and Bir have derived the Hamiltonian within the $k \cdot p$ framework for a general strain. In the absence of spin-orbit coupling this Hamiltonian is written as:

$$\begin{aligned} H_{PB} =& a(e_{xx} + e_{yy} + e_{zz}) + 3b[(L_x^2 - L^2/3)e_{xx} + c.p.] \\ &+ \frac{6d}{\sqrt{3}}\left(\frac{1}{2}(L_xL_y + L_yL_x)e_{xy} + c.p.\right), \end{aligned} \tag{1.24}$$

where a, b, and d are the three *Pikus-Bir* deformation potentials corresponding to strain tensors with symmetries Γ_1, Γ_3, and Γ_4, respectively, c.p. stands for cyclic permutation and L_j are the angular momentum operators. The deformation potentials b and d are associated with splittings in the [100] and [111] directions, whereas a is associated with an hydrostatic deformation of the crystal.

1.4 Effect of Quantum Confinement on Electrons

The effect of quantum confinement on electrons became important in the semiconductor area after the development of sophisticated growth techniques such as molecular beam epitaxy (MBE) and metal-organic chemical vapor deposition (MOCVD), since they allow to grow low-dimensional structures. The confinement effect should be taken into account when any dimension of a system is comparable to the particle or quasi-particle wavelength, defined by de Broglie as:

$$\lambda = \frac{h}{p} = \frac{h}{mv}\sqrt{1 - \frac{v^2}{c^2}}, \tag{1.25}$$

where h is Planck's constant, m is the particle rest mass, v is the particle velocity, and c is the speed of light in vacuum. Typical examples of structures showing quantum confinement are two-dimensional structures referred as **quantum wells** (QWs), one-dimensional as **nanowires**, and zero-dimensional as **quantum dots** (QDs). An important discovery in this field was the **quantum Hall effect** (QHE) in a two dimensional electron gas, discovered by *Klauss Von Klitzing* in 1980 for which he was awarded the Nobel Prize in 1985.

A typical and very useful example of confinement is given by a particle with effective mass m^* confined in a one-dimensional system by infinite potential barriers in the z direction. The allowed wavevectors and energy of the Bloch wave functions are given by:

$$k_{zn} = \frac{2\pi}{\lambda_n} = n\pi/L, \tag{1.26}$$

$$E_n = \frac{\hbar^2 {k_{zn}}^2}{2m^*} = \frac{\hbar^2}{2m^*}\frac{n^2\pi^2}{L^2}, \tag{1.27}$$

where $n = 1, 2, 3, ...$ are the indexes of each energy level and L is the thickness of the potential well (see Fig. 1.3). Thinking of a real quantum well sample, in general the thickness L is subjected to fluctuations due to intrinsic inaccuracies of the growth mechanism, leading to the inhomogeneous broadening of the confined levels (see Fig. 1.3). The energy dispersion δE as a function of the potential well thickness fluctuations δL can be calculated from Eq. (1.27) as:

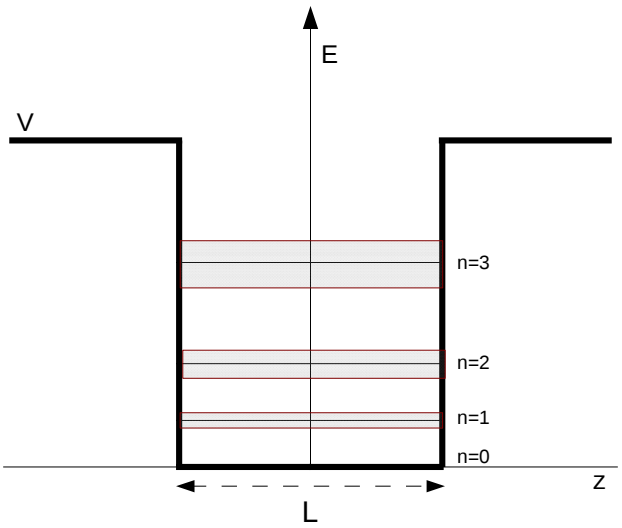

Figure 1.3: Scheme of a one-dimensional potential well with a barrier V. Four levels are shown denoted as n=0,1,2,3. The horizontal band around each level corresponds to changes in the energy of each level due to fluctuations in the thickness (L) of the potential well.

$$\delta E = \frac{\hbar^2 n^2 \pi^2}{m^* L^3} \delta L = \frac{2E_n}{L} \delta L \tag{1.28}$$

This result shows that this broadening increases quadratically with the level number. In adittion, if we consider a fixed value for the level number n this broadening increases as the well thickness decreases. This is a purely quantum effect and should not be confused with the inhomogeneous broadening observed, for example, in a distribution of QDs (or QWs) of different size.

Bibliography

For a complete reference of the Theoretical Background presented in this chapter the reader should reefer to the following sources:

- *"Fundamentals of Semiconductors"*, Peter Y. Yu and Manuel Cardona, Springer.
- *"High Pressures in Semiconductors Physics II Vol. 55"*, Editors: Tadeusz Suski and William Paul, Academic Press.
- *"The Classical Theory of Fileds"*, L.D. Landau and E.M. Lifshitz, Butterworth Heinmann.
- *"Quantum Mechanics (Non-Relativistic Theory)"*, L.D. Landau and E.M. Lifshitz, Butterworth Heinmann.

Chapter 2

Experimental Techniques

2.1 Pressure Techniques

One of the pioneers in high pressure physics was P. W. Bridgman who was awarded the Nobel prize in 1946 for introducing the concept of *anvil cell*, widely used nowadays. Hydrostatic pressure is created through the deformation of some sealing material with a hole in it serving as pressure chamber, and which is placed between two pistons. Bridgman used tungsten carbide which is very hard but opaque and, thus, does not allow for optical measurements. The introduction of diamonds as anvils [1] was an important milestone on the way to perform optical experiments under high hydrostatic pressure.

2.1.1 Diamond Anvil Cell

The diamond anvil cell (DAC) is a device particularly suited to perform optical measurements under high hydrostatic pressure. The chamber volume where the sample is placed is defined inside a 200-300 μm hole drilled into a metal gasket which is closed from the top and bottom by the flat parallel faces of two diamond anvils (see fig.2.1). The sample is subjected to pressure when the two diamonds are pushed together decreasing the chamber volume, while slightly deforming the gasket. Depending on the pressure range and sample volume, different cells have been built and most of them comprise a movable piston which holds one of the diamonds and some kind of lever mechanism to apply the pressing force. The cell used in the experiments presented here (fig. 2.1) was designed by *Syassen* and *Holzapfel* [2] and allows for measurements up to 25 GPa. Due to the large aperture angle of 36°, it is also suitable for Raman experiments.

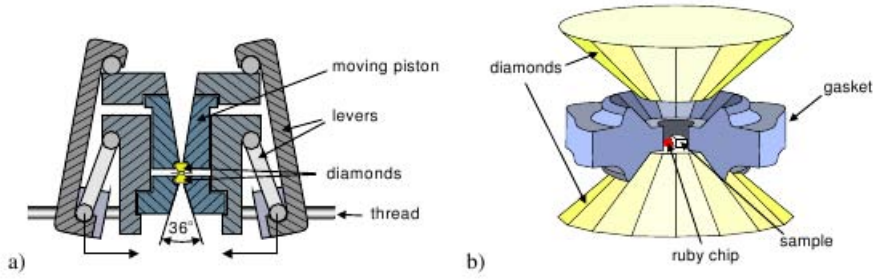

Figure 2.1: Sketch of the diamond anvil cell. *Left:* Lever mechanism to move the upper piston. The end points of the levers are driven by two threads. When using the cell in a cryostat two long rods connect the threads with a gear outside the cryostat. *Right:* Illustration of the two diamonds and the gasket.

The gasket is made of a nickel-chromium alloy referred to as Inconel X-7501, which is chosen for its mechanical strength and hardness. The fabrication process of the raw gaskets (small discs of 8 mm in diameter and 250 μm in thickness) induces strain in the material, which has to be released to regain its natural hardness. Therefore, they have to run through a tempering procedure. The discs are then pressed with the diamonds creating a faceted indentation of about 100 μm thickness and 500 μm diameter. This cold forming step represents an additional hardening. Finally, a hole of 200-300 μm in diameter is drilled into its center. This hole is the actual sample chamber which will be loaded with a sample whose dimensions must not exceed 100x100x50 μm^3 and a small ruby ball for the pressure determination.

Various organic liquids and condensed gases have been used as pressure medium to assure hydrostatic conditions in the sample chamber. ^{4}He is often chosen for low temperature measurements due to its nearly hydrostatic behavior up to 60 GPa. In addition, its superfluid phase below 2.2 K simplifies the filling up of the cell. For room temperature applications a 4:1 mixture of methanol and ethanol is used. This mixture can be used only up to ≈13 GPa, since at this pressure it solidifies becoming a non-hydrostatic medium. A review of common high pressure techniques can be found in Ref. [3].

2.1.2 Pressure Determination

The pressure in the anvil cell is determined in situ via the pressure dependent shift of the ruby fluorescence. For that purpose a small ruby ball is placed together with the sample inside the pressure chamber. The ruby is Cr^{3+}

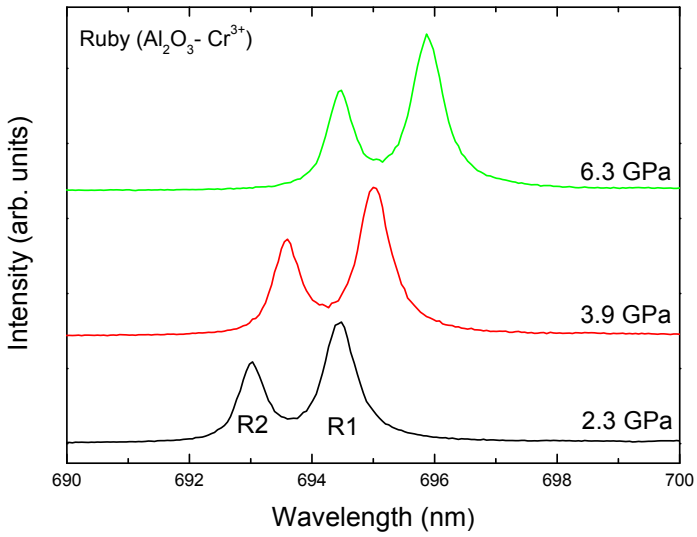

Figure 2.2: Typical Ruby spectra under three different pressures. The two lines R1 and R2 arising for the Cr^{3+} impurities are shown. The R1 line is the one used for pressure determination at all temperatures.

doped Al_2O_3 (Sapphire) and shows a well known strong red fluorescence. The crystal symmetry of ruby is rhombohedral, so that the Cr^{3+} ions and their six nearest neighbors form a distorted octahedron whose symmetry is C_3 [4]. The resulting crystal field leads to a splitting of the degenerated energy levels of the 3d electrons of Cr^{3+} giving rise to the two strong fluorescent transitions denoted R1 and R2 with energies E(R1) = 14418 cm^{-1} and E(R2) = 14447 cm^{-1}. Applying external pressure decreases the inter-atomic distances and, therefore, the crystal field increases. The level splitting increases resulting in a net reduction of the R1 and R2 transitions energies. The dependence of the ruby fluorescence on hydrostatic pressure has been determined up to 80 GPa [5]:

$$P = \frac{A}{B}\left\{\left[1 + \left(\frac{\lambda - \lambda_0}{\lambda_0}\right)\right]^B - 1\right\}, \tag{2.1}$$

where A = 1904 GPa, B = 7.665, λ_0 and λ are the wavelengths of the R1 at ambient and given pressure, respectively. As small balls of ruby might be strained internally the values for λ_0 may differ for each ball representing an error source for the pressure determination. In Fig. 2.2 we show typical

spectra of ruby fluorescence at several pressures inside the DAC and with methanol-ethanol as pressure medium.

For a precise determination of the pressure the dependence of the R1 luminescence on temperature has to been taken into account. The pressure coefficients A and B are independent of temperature to a good approximation [6, 7], whereas the energy of the R1 and R2 lines shifts with temperature. At low temperatures only the low energy R1 line is visible. The temperature dependence of the R1 line is best described by a two-phonon Raman-process model [8], which yields:

$$\nu_R(T) - \nu_R(0) = \alpha \left(\frac{T}{\Theta}\right)^4 \int_0^{\Theta/T} \frac{x^3}{e^x - 1} dx, \tag{2.2}$$

where $\nu(T)$ is the energy of the R1 band at temperature T and ambient pressure and $\nu(0)$ that at $0K$. The parameters Θ and α have been determined by fitting Eq. (2.2) to a comprehensive set of experimental data ($\Theta = 760$ K and $\alpha = 419$ cm^{-1} [9]).

In some of the experiments where samples grown on a Si(100) substrate were investigated, the zone center optical phonon of the substrate was used for pressure calibration. The fact that this phonon is intense makes it suitable for a good pressure determination. As a consequence, loading the ruby balls into the cell is avoided, making the procedure easier. The pressure calibration for this phonon was done using the previous ruby calibration as:

$$P = 41.13 - \sqrt{1691.6 + 16.1 \times (520.7 - \omega_{Si})} \tag{2.3}$$

where P is the pressure in GPa, and ω_{Si} is the frequency of the Si phonon in cm^{-1}.

2.1.3 Low Temperature Pressure Technique

When using the DAC at low temperatures with ^{4}He as pressure medium, the loading of the cell is more difficult since it cannot be sealed outside the cryostat. Thus, the DAC has to be loaded with the sample and a ruby chip but the diamonds must not close the sample chamber completely. The cell is placed into the cryostat and is immersed in fluid ^{4}He which will be pumped (with mechanical pump) to lower its equilibrium temperature till the transition to the superfluid state at 2.2 K occurs. Under this condition the superfluid ^{4}He easily enters into the cell, filling it completely. Finally, the DAC can be sealed by carefully approaching the diamonds. As ^{4}He instantly crystallizes when subjected to pressure at 2 K the cell has to be heated well

above the melting point to relax non-hydrostatic strain. When cooling down again into the solid phase it is assumed that the pressure on the sample is mostly hydrostatic. The same procedure applies if the pressure is about to be changed. It is crucial to reach a point in the phase diagram well above the melting line such that ^{4}He is liquid during the pressure change.

2.2 Raman Spectroscopy

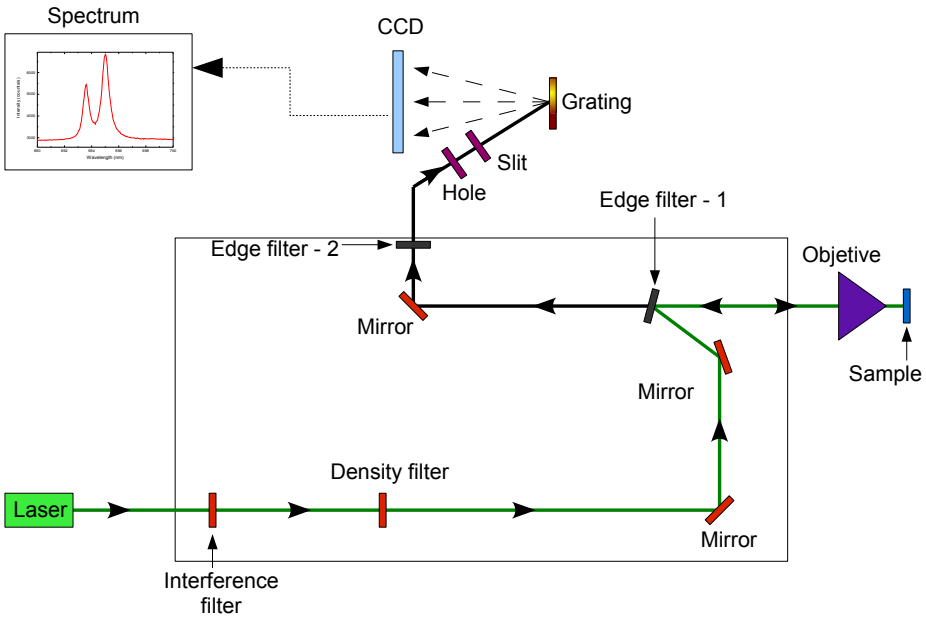

Figure 2.3: Schematic diagram of the LabRam HR 800 spectrometer. Two holographic edge filters are used to filter the laser light.

Although the inelastic scattering of light was predicted by Smekal in 1923, it was not until 1928 that it was observed in practice. The Raman effect was named after one of its discoverers, the Indian scientist Sir C. V. Raman who observed the effect by means of sunlight (1928, together with K. S. Krishnan and independently by Grigory Landsberg and Leonid Mandelstam). Raman won the Nobel Prize in Physics in 1930 for this discovery accomplished using sunlight, a narrow band photographic filter to create monochromatic light and a "crossed" filter to block this monochromatic light. He found that light of changed frequency passed through the "crossed" filter. Subsequently the

mercury arc lamp became the principal light source, first with photographic detection and then with spectrophotometric detection. Currently lasers are used as light sources.

In this work, Raman spectra were collected using a commercial spectrometer optimized for this purpose. One of the most important experimental complications of this technique is that the energy of the Raman excitations (phonons) is of the order of tens of meV, which means that for studying this effect we need a device that can filter the incident laser but with a very narrow bandwidth. This can be achieved in two different ways: i) Filtering the incident laser with successive gratings, ii) Using an holographic notch or edge filter.

A Jobin Yvon LabRam HR 800 spectrometer based on the edge filter method was used for all the experiments. Fig. 2.3 shows a sketch of the spectrometer. The laser filtering procedure is achieved by two successive edge filters. With this configuration it is possible to measure as close as 50 cm^{-1} from the laser. Another important feature is provided by a confocal microscope in order to perform micro-Raman experiments. The confocal geometry which is tuned by changing the aperture of the pinhole (HOLE in Fig. 2.3), allows for having spatial resolution in the focus direction. An important difference with the grating filtered spectrometer is the loss intensity due to its successive gratings. In the holographic spectrometer only one grating is used, thus, reducing this loss of light in the filtering step. This makes the Labram HR 800 suitable for low signal experiments such as Raman spectroscopy.

Bibliography

[1] A. W. Lawson and T.-Y. Tang. A Diamond Bomb for Obtaining Powder Pictures at High Pressures. Rev. Sci. Instruments 21, 815 (1975).

[2] K. Syassen and W. B. Holzapfel. In K. D. Timmerhaus and M. S. Barber (editors) Physics of Solids Under High Pressure, volume 1, p. 223 (1979).

[3] A. Jayaraman. Diamond anvil cell and high-pressure physical investigations. Rev. Mod. Phys. 55, 65 (1983).

[4] S. Sugano and Y. Tanabe. Absorption Spectra of Cr3+ in Al2O3. Journal of the Physical Society of Japan 13(8), 880 (1958).

[5] H. K. Mao, J. Xu and P. M. Bell. Calibration of the ruby pressure gauge quasi-hydrostatic conditions. J. Geophys. Res 91, 4673 (1986).

[6] R. A. Noack and W. B. Holzapfel. Calibration of the ruby pressure scale at low temperatures. In K. D. Timmerhaus and M. S. Barber (editors) High Pressure Science and Technology, p. 748 (Plenum Press, New York, 1979, 1979).

[7] G. J. Piermarini and S. Block. Ultrahigh pressure diamond-anvil cell and several semiconductor phase transition pressures in relation to the fixed point pressure scale. Rev. Sci. Instruments 46, 973 (1975).

[8] D. E. McCumber and M. D. Sturge. Linewidth and Temperature Ruby. Journal of Applied Physics 34(6), 1682 (1963).

[9] J. Yen and M. Nicol. Temperature dependence of the ruby luminescence measuring high pressures. Journal of Applied Physics 72(12), 5535 (1992).

Chapter 3

Results and Discussion

3.1 Phonon Deformation Potentials in strained SiGe alloys

Although a great amount of work has been done in Si/Ge systems due to their applications in Si-based technology, some fundamental issues are not properly addressed to date. Strained SiGe alloys are an example of such disappointing state of the art. The complete compositional dependence of their **phonon deformation potentials** have not been previously determined. In this section, previous results in these fields will be presented in order to provide the reader with a complete view on these topics. Finally, in the last subsection, a general conclusion will be given.

3.1.1 Motivation and Previous Work

Strain and Composition determination

The study of the strain status and composition in strained SiGe alloys was subject of interest since the early 80s. After the first high quality strained $Si_{1-x}Ge_x$ alloys were grown [1], *Cerdeira et. al.* [2] studied the zone center optical branches using Raman scattering. In this work, only these phonon branches will be taken into account, which in systems like Si or Ge are degenerated due to the non-polar nature of the bondings. Fig. 3.1 shows a typical spectrum of a $Si_{0.35}Ge_{0.65}$ alloy extracted from Ref. [2] where four dominant peaks are observed at about 300 cm^{-1}, 400 cm^{-1}, 500 cm^{-1} and 520 cm^{-1}. These correspond to scattering by optical phonons involving Ge-Ge, Si-Ge, Si-Si and Si-Si (substrate) stretching vibrations, respectively. The origin of these peaks is well understood [3], and their dependence with composition was measured by *Alonso et. al.* [4]. Although disorder could introduce

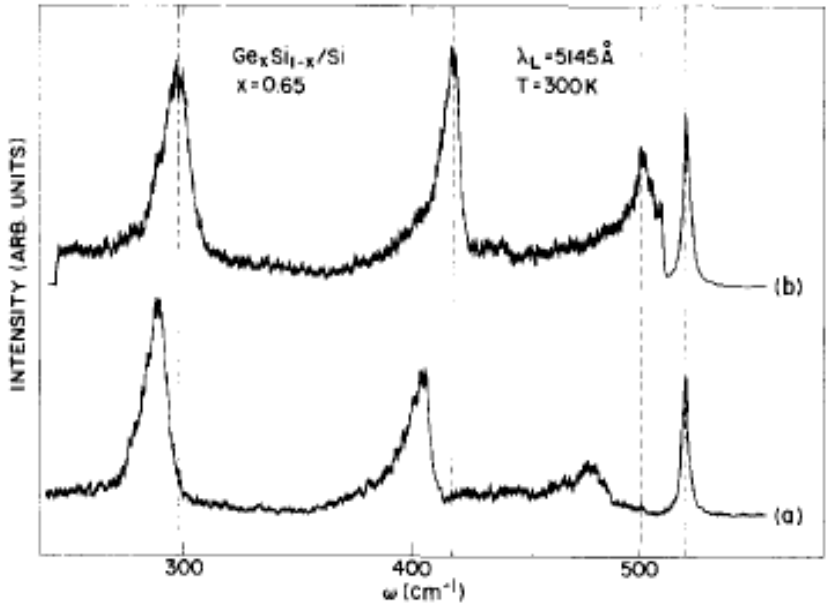

Figure 3.1: Raman Spectrum of $Si_{1-x}Ge_x$ for x=0.65: a) Single incommensurate layer and b) Strained superlattice. Extracted from Ref. [2]

alterations, the selection rules for Raman scattering in compositionally disordered c-$Si_{1-x}Ge_x$ alloys are the same as for pure c-Si or c-Ge [4]. The strain and composition dependence of the phonon frequency in a pseudomorphic $Si_{1-x}Ge_x$/Si alloy can be written as:

$$\delta\omega = \omega(x, \epsilon_{ij}) - \omega_0(x) = \omega_0(-\tilde{K}_{11} \cdot \alpha/2 + \tilde{K}_{12})\epsilon_{\|}, \tag{3.1}$$

where ω_0 is the frequency for zero strain, $\epsilon_{\|}$ is the in-plane strain, α=$2C_{12}/C_{11}$ with C_{ij} the elastic constants, and $\tilde{K}_{ij}$ are the phonon deformation potentials (PDPs) as defined by *Anastassakis* and *Cardona*[5]. Since no values for the PDPs of the alloys were available, interpolations between the values for pure Si and Ge were used for intermediate concentrations.

From Eq. (3.1) it follows that to determine the strain status of SiGe alloys we should first know the values of ω_0, $\tilde{K}_{11}$ and $\tilde{K}_{12}$. *Alonso and Winer* grew a series of unstrained alloys in the whole compositional range and measured the phonon frequency at zero strain (ω_0) for the Ge-Ge, Si-Ge and Si-Si vibrational modes. Their results can be summarized in the following equations, where x is the Ge content:

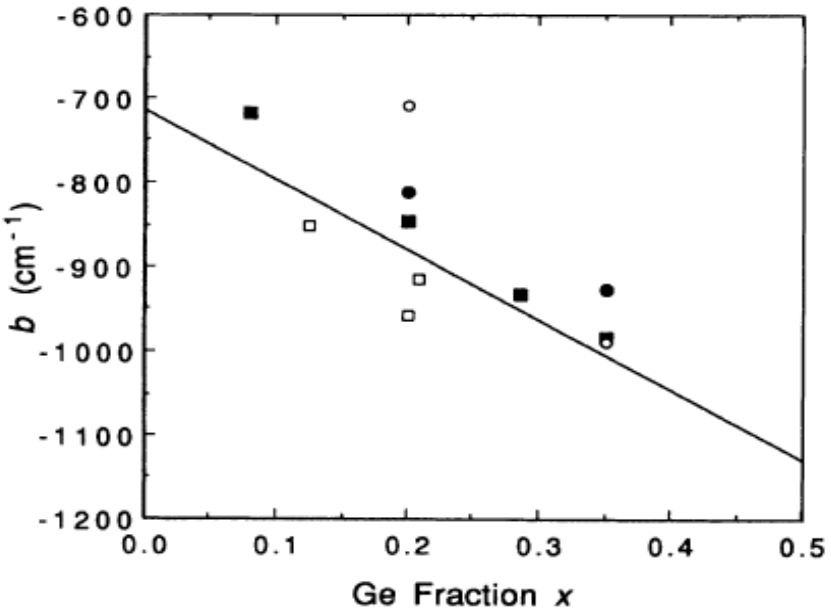

Figure 3.2: Strain shift coefficient for $Si_{1-x}Ge_x$ alloys as a function of Ge concentration. The solid and opened squares are values for the Si-Si mode. Solid and opened circles are values for the Ge-Ge and Si-Ge modes, respectively. Extracted from Ref. [6].

$$\omega_0^{Ge-Ge} = 284 + 5 \cdot x + 12 \cdot x^2 \tag{3.2}$$

$$\omega_0^{Si-Ge} = 400 + 29 \cdot x - 95 \cdot x^2 + 213 \cdot x^3 - 170 \cdot x^4 \tag{3.3}$$

$$\omega_0^{Si-Si} = 520 - 68 \cdot x \tag{3.4}$$

No experimental values of the PDPs were known at that moment since an independent determination of both presents some difficulties. The most direct experimental technique would be to perform uniaxial stress measurements from where the PDPs are directly extracted, but this approach is problematic since bulk SiGe alloys of any composition are not easy to grow. An alternative approach by *Cerdeira* that was used for several years to deal with the Raman spectra of strained layers was to define the **phonon strain shift coefficient** following Eq. (3.1). Thus, we can rewrite this equation in a more simple form as $\delta\omega = b_s \cdot \Delta\epsilon$, where b_s is defined as the strain shift coefficient, being a linear combination of the PDPs.

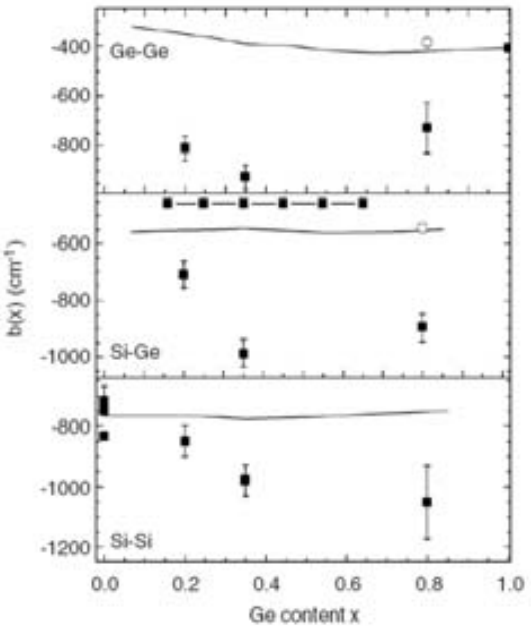

Figure 3.3: Strain shift coefficients for the three Raman modes as a function of Ge molar fraction x. Solid lines are the results of the calculations, opened and closed symbols are measurements from Refs.[8, 9, 10]. Extracted from Ref. [7].

Subsequent work was focused mainly to obtain b_s for the intermediate compositional range. *Lockwood et. al.* [6] followed *Cerdeira*'s approach with samples between 0 and 0.5 in Ge content. Fig. 3.2 shows their experimental results obtained for the strain shift coefficient of the Ge-Ge, Si-Ge and Si-Si modes. The absolute value of the obtained coefficients is rather large, especially in the middle of the composition range. Nevertheless, the used layers were very thick, well beyond the critical thickness, so that an overestimation of b_s is possible if the samples were partially relaxed, which is very likely. For the high Ge content range *Stoehr et. al.* reported results complementing the work of *Lockwood et. al.* Few experimental data were available in this range since as the Ge content increases the strain of the epilayer increases producing dislocations and, consequently, relaxation of the epilayer. This is the main reason why experimental data of b_s for the whole compositional range were lacking in the literature.

Recently *Pezzoli et. al.* [7] presented calculations of b_s for the whole compositional range using a modified Keating model. Fig. 3.3 shows their

results together with values from the literature. This figure summarizes all the available data to that moment. A great dispersion between the b_s values with almost no agreement between experiment and theory leads to a bad determination of the strain status of SiGe alloys.

This problem was solved growing a series of samples by MBE in the whole compositional range and measuring directly the PDPs by combining Raman spectroscopy from the cleaved edge with high pressure measurements [see Eqs. (3.5)]. The grown samples were strained $Si_{1-x}Ge_x$/Si(001) layers. The uniaxial component of the applied strain reduces the crystal symmetry leading to a splitting of optical branches into a doublet (in-plane directions) and a singlet (growth direction). Thus, the singlet to doublet splitting was measured using Raman scattering from the growth direction and cleaved edge of the samples. Although these measurements should be enough for an independent determination of $\tilde{K}_{11}$ and $\tilde{K}_{12}$, ω_0 is still lacking. It was found that for a good determination of the PDPs is crucial to have an accurate value of this quantity. In the present approach ω_0 is no longer necessary since the determination of the pressure coefficient of the singlet introduces an additional equation independent of ω_0, which, by combining the singlet and doublet equations, allows to avoid the ω_0 dependence. The equations for the singlet, doublet, and singlet pressure dependence are written as:

$$\begin{aligned}
\Omega_s - \omega_0 &= \frac{\omega_0 \epsilon_\parallel}{C_{11}}[C_{11}\tilde{K}_{12} - C_{12}\tilde{K}_{11}] \\
\Omega_d - \omega_0 &= \frac{\omega_0 \epsilon_\parallel}{2C_{11}}[C_{11}(\tilde{K}_{11} + \tilde{K}_{12}) - 2C_{12}\tilde{K}_{12}] \\
\frac{d(ln\Omega_s)}{dP} &= \frac{1}{6B_0^{SiGe}}(\tilde{K}_{11} + 2\tilde{K}_{12}) + \frac{1}{3}\left(\frac{1}{B_0^{SiGe}} - \frac{1}{B_0^{Ge}}\right)(\tilde{K}_{12} - \tilde{K}_{11} \cdot \frac{\alpha}{2})
\end{aligned} \tag{3.5}$$

where B_0^x is the bulk modulus and all the other quantities were previously defined.

As was already mentioned, it is possible to combine the first two equations in (3.5) to obtain a system independent of ω_0. Consequently, to determine $\tilde{K}_{11}$ and $\tilde{K}_{12}$ we have to measure Ω_s, Ω_d, and $\frac{d(ln\Omega_s)}{dP}$. Finally, the phonon strain shift coefficients are easily calculated using Eq. (3.1)

In the next section the article entitled *"Composition dependence of the phonon strain shift coefficients in SiGe alloys revisited"* is presented. The compositional dependence for both PDPs and phonon strain shift coefficient for the three vibrational modes is experimentally determined for the first time.

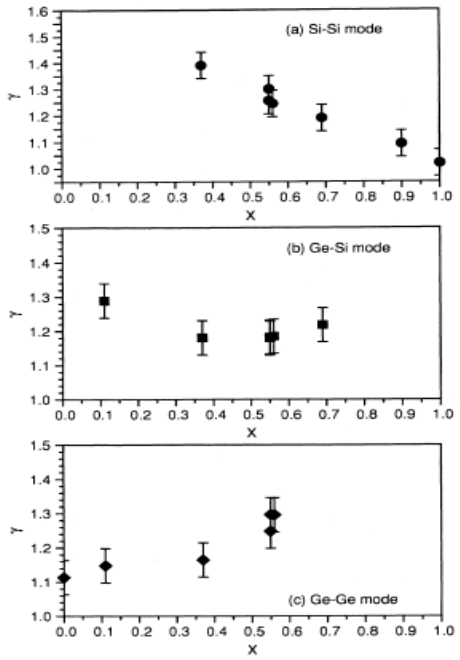

Figure 3.4: The Grüneisen parameters for Ge-Ge, Si-Ge and Si-Si modes as a function of the Si content x. Extracted from Ref. [12]

Grüneisen Parameter

A confusing literature is also found concerning the Grüneisen parameter for zone center optical phonons in SiGe alloys. This parameter is usually defined as:

$$\gamma_\nu = \frac{B_0}{\omega_0^\nu}\left(\frac{d\omega^\nu}{dP}\right) = -\frac{1}{6}(\tilde{K}_{11} + \tilde{K}_{12}), \tag{3.6}$$

where B_0 is the bulk modulus of the material, ω_0^ν is the zero-strain frequency, $d\omega^\nu/dP$ is the pressure derivative of the phonon frequency, and ν refers to a vibrational mode. *Renucci et. al.* [11] have measured first this parameter in bulk $Si_{0.54}Ge_{0.56}$ alloys. They obtained the phonon pressure coefficient and computed the Grüneisen parameter, which resulted in 30% bigger values than for pure Ge ($\gamma^{Ge} \approx 1$). The main contribution to this subject was made by *Sui et. al.* [12]. They have grown polycrystalline SiGe samples covering almost all the compositional range. Their results for the Grüneisen parameter are shown in Fig. 3.4. Similarly to *Renucci et. al.*, they have found an increase of this parameter for intermediate Ge contents.

As was already mentioned, a precise determination of the phonon pressure coefficient of the singlet component is necessary to obtain $\tilde{K}_{11}$ and $\tilde{K}_{12}$. Once these potentials are determined its easy to compute the Grüneisen parameter using Eq. (3.6). For this purpose another set of samples in the whole compositional range was grown. A completely different result to that by *Sui et. al.* came out. From our measurements the Grüneisen parameter was found to be approximately independent on composition. These results are presented in the next subsection under the title *"Measurement of phonon pressure coefficients for a precise determination of deformation potentials in SiGe alloys"*. The importance of this contribution can be summarized as follows: i) They correct all the previous determinations by *Renucci* and *Sui*, ii) They are the key to accurately determine the PDPs ($\tilde{K}_{11}$, $\tilde{K}_{12}$).

3.1.2 Experiments and Results

Article n: 1

Title: Composition dependence of the phonon strain shift coefficients in SiGe alloys revisited

Authors: J. S. Reparaz, A. Bernardi, A. R. Goñi, M. I. Alonso, and M. Garriga.

Journal: Applied Physics Letters

Article n: 2

Title: Measurement of phonon pressure coefficients for a precise determination of deformation potentials in SiGe alloys

Authors: J. S. Reparaz, A. Bernardi, A. R. Goñi, M. I. Alonso, and M. Garriga.

Journal: Physica Status Solidi b

Composition dependence of the phonon strain shift coefficients of SiGe alloys revisited

J. S. Reparaz,[a] A. Bernardi, A. R. Goñi, M. I. Alonso, and M. Garriga
Institut de Ciència de Materials de Barcelona-CSIC, Esfera UAB, 08193 Bellaterra, Spain

(Received 21 November 2007; accepted 31 January 2008; published online 26 February 2008)

By combining Raman scattering from the cleaved edge and under hydrostatic pressure, we have accurately determined the tetragonal phonon deformation potentials of strained $Si_{1-x}Ge_x$ alloys in the entire compositional range for the Ge-like, Si-like, and mixed Si–Ge optical modes. A known biaxial strain is induced on thin alloy layers by pseudomorphic epitaxial growth on silicon and subsequent capping. We also determine the strain shift coefficient of the three modes, which are essentially independent of Ge content between 0.4 and 1. This is key information for an effective use of Raman scattering as strain-characterization tool in SiGe nanostructures. © *2008 American Institute of Physics*. [DOI: 10.1063/1.2884526]

A precise knowledge of the phonon deformation potentials (DPs), i.e., the derivative of the optical phonon frequency with respect to an elastic deformation of the lattice, is crucial for an effective use of Raman scattering as powerful strain-characterization tool in compound semiconductor microstructures.[1] In particular, for the SiGe material system, there is a great deal of discrepancy between different literature sources about the exact values of the DPs mainly for intermediate Ge concentrations.[2–7] There might be many reasons for such differences (up to a factor of 2) such as strain relaxation effects for epitaxial layers exceeding the critical thickness,[3] the use of polycrystalline samples,[4] or, as pointed out in Ref. 5, due to large uncertainties in the determination of the phonon frequency for the unstrained alloy as compared with literature data obtained for bulk materials.[8,9] Such disappointing state-of-the-art is surprising in view of the technological importance of strained SiGe/Si heterostructures and the great potential of Raman scattering to measure built-in strain in nanostructured materials such as superlattices,[2] self-assembled quantum dots,[10–13] and complementary metal-oxide semiconductor devices.[14]

In practice, for the spectroscopical determination of strain one needs to know the so-called strain shift coefficient, defined as the ratio of the phonon frequency shift over the strain that induces the shift: $b_s=\Delta\omega/\Delta\varepsilon$. For the most frequent case of Raman measurements in backscattering geometry from the (001) surface, the strain is directly determined from the frequency shift of the Raman-allowed *singlet* component of the optical phonons using the expression for the strain shift coefficient given by[2,6]

$$b_s = \omega_0(-\tilde{K}_{11}\cdot\alpha/2 + \tilde{K}_{12}). \quad (1)$$

Here, ω_0 is the frequency of the unstrained phonon mode, $\tilde{K}_{ij}$ are the dimensionless phonon deformation potentials, as defined in Ref. 1, and $\varepsilon_\perp=-\alpha\varepsilon_\parallel$ represents the relation between the strain in growth direction and in-plane strain. For the case of a strictly bisotropic stress like in epitaxially grown pseudomorphic layers holds $\alpha=2C_{12}/C_{11}$, where C_{ij} are the elastic constants of the material. A confusing situation is found in the literature for the accepted values of the strain shift coefficient of the optical phonons in $Si_{1-x}Ge_x$ alloys:[2–7] For intermediate Ge concentrations in the range of $0.3\leqslant x\leqslant 0.8$, the values of b_s for the Ge–Ge and the Si–Si mode are twice as large and about 50% higher than for the pure materials, respectively. This is not only counterintuitive but recently appeared theoretical evidence[15] for b_s being fairly constant over the whole concentration range, holding this for the three optical modes of the SiGe alloy.

In order to clarify this inconsistency, we have grown a set of five strained epitaxial SiGe layers on Si with Ge concentrations between 0.1 and 0.75 and measured the shift and splitting of the optical phonons caused by the strain due to the lattice mismatch between alloy and substrate. From these measurements and that of the pressure coefficient of the singlet, we were able to accurately determine two phonon deformation potential constants, $\tilde{K}_{11}$ and $\tilde{K}_{12}$, as a function of alloy composition. We obtained for the strain shift coefficient of the Ge–Ge, Si–Ge, and Si–Si alloy modes the same flat dependence on Ge content from pure Ge down to $x\sim 0.4$, followed by a slight increase for lower concentrations. Our results are in good qualitative agreement with the calculations of Ref. 15, based on a modified Keating model.

A series of samples containing a strained $Si_{1-x}Ge_x$ alloy layer was grown by molecular beam epitaxy on Si(001) substrates at a temperature of 400 °C.[16] The growth sequence consists of deposition of a 100-nm-thick Si buffer layer, followed by the SiGe alloy layer with thickness below critical to ensure pseudomorphism and, finally, a 300 nm-thick Si cap layer. A thick cap layer is crucial to avoid elastic strain relaxation of the SiGe layer after cleavage for micro-Raman measurements from the cleaved edge. The nominal thicknesses of the alloy layers with a Ge concentration $x=0.73$, 0.55, 0.38, and 0.26 were 7, 10, 7, and 15 nm, respectively. For these layer thicknesses, we estimate an upper bound of 0.2 cm^{-1} for the frequency shift due to phonon-confinement effects,[17] which is negligible compared to other error sources. For the lowest Ge content of 0.10, a multilayer SiGe/Si structure with a total alloy thickness of 200 nm was deposited to increase the Raman signal without exceeding the critical thickness. The strain and composition of the alloys were determined by x-ray reciprocal space mapping along the (224) diffraction direction and for the lattice constant dependence on composition, we used the relation given elsewhere.[18,19] All alloys showed good pseudomorphic growth to Si.

[a]Electronic mail: sebareparaz@hotmail.com.

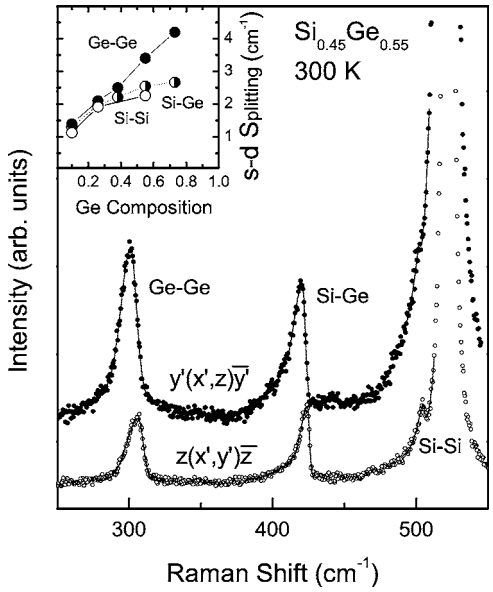

FIG. 1. Representative Raman spectra of a strained alloy layer with Ge content $x=0.55$ measured at room temperature in different scattering configurations with crossed linearly polarized light. Peak assignment to the optical modes of the alloy is indicated. Solid lines represent the results of least-squares fits to the spectra using asymmetric Gaussians. The inset shows the values of the singlet-doublet splitting for the three optical alloy modes as a function of Ge concentration.

Raman spectra were collected in backscattering geometry at room temperature using the 514.5 nm line of an Ar^+ laser. Raman peak positions are determined with an error of less than 0.5 cm^{-1}. Special care was taken to keep laser power as low as possible to avoid laser heating and the consequent but spurious redshift of the Raman peaks, mainly when exciting at the cleaved edge. A laser power density of 1.5 kW/cm^2 turned out to be adequate. Measurements under pressure were carried out using the diamond anvil cell (DAC) technique. A 4:1 mixture of methanol and ethanol was employed as the pressure-transmitting medium. Pressure was monitored *in situ* by the shift of the Si longitudinal optical phonon. Samples with similar alloy composition but without cap layer were grown for the Raman experiments under pressure. Samples loaded into the DAC were previously thinned to about 30 μm by mechanical polishing.

The threefold degeneracy of the optical phonon modes at the Brillouin-zone center is lifted at the alloy layer due to the tetragonal distortion of the lattice caused by the bisotropic stress induced by its lattice mismatch to Si. The zone-center phonons split into a singlet (s, vibrations in growth direction) and a doublet (d, in-plane vibrations) component which are apparent in Raman spectra with different linearly polarized light configurations owing to the following selection rules: the singlet component is observed in backscattering from the growth direction using the geometry $z(xy)\bar{z}$, whereas, the doublet component appears in spectra measured in backscattering from the cleaved edge $x'(zy')\bar{x}'$, where x, y, z, x', and y' are the [100], [010], [001], [110], and $[\bar{1}10]$ crystallographic directions, respectively. Figure 1 shows two representative spectra of the alloy with 0.55 Ge content. Geometries with crossed linear polarization were chosen on purpose in order to suppress contributions from second-order Raman processes by acoustic phonons in Si, which would have hampered the precise determination of the peak position mainly for the Ge–Ge mode. The position of all Raman peaks was determined by a conventional least-squares fitting procedure using asymmetric Gaussians for the alloy modes and a Lorentzian for the Raman peak of the Si layers. The frequency splitting between peaks measured using both scattering geometries is indicative of a tetragonal strain in the alloy layer. Splitting values of the three alloy modes are plotted as a function of alloy composition in the inset of Fig. 1. The Ge–Ge mode splitting increases linearly with Ge concentration, whereas, for the other modes, the increase of the splitting is sublinear.

The hydrostatic strain-induced shift of the phonon frequencies and the singlet-doublet splitting, which are linear on the strain $\Delta\varepsilon=(a_{\mathrm{Si}}-a_0(x))/a_0(x)$ given by the lattice mismatch, can be written in terms of the adimensional phonon deformation potentials as[1,20]

$$\frac{\omega_s+2\omega_d}{3\omega_0}=1+\frac{2-\alpha}{6}(\tilde{K}_{11}+2\tilde{K}_{12})\Delta\varepsilon, \tag{2}$$

$$\frac{\omega_s-\omega_d}{\omega_0}=-\frac{1+\alpha}{2}(\tilde{K}_{11}-\tilde{K}_{12})\Delta\varepsilon. \tag{3}$$

Using these equations, one should be able to determine the phonon DPs of the alloys from the measured frequencies of the singlet and doublet components. This method, however, presents a major drawback which concerns large uncertainties derived from the estimation of the unstrained frequency ω_0 from literature data.[5,8] As an alternative, we propose to get rid of ω_0 by division of Eq. (2) by Eq. (3), adding a third equation which corresponds to the hydrostatic pressure coefficient of the singlet frequency. For that purpose, we have performed Raman measurements using the DAC for every concentration. The logarithmic derivative of the phonon frequency over pressure is readily calculated as:[13]

$$6\frac{d\ln\omega_s}{dP}=-\frac{\tilde{K}_{11}+2\tilde{K}_{12}}{B_0^{\mathrm{SiGe}}}+(2\tilde{K}_{12}-\alpha\tilde{K}_{11})\left(\frac{1}{B_0^{\mathrm{SiGe}}}-\frac{1}{B_0^{\mathrm{Si}}}\right), \tag{4}$$

where B_0 is the bulk modulus of the corresponding material. For the alloys, B_0 was obtained by linear interpolation between the values of the pure elements. The second term in Eq. (4) represents the correction to the phonon pressure coefficient due to the different elastic properties of alloy and Si substrate, which tends to reduce the lattice mismatch strain with increasing pressure. This correction amounts up to 15% for high Ge concentrations, hence, it has to be taken into account for an accurate determination of the phonon DPs. The key point is that ω_0 does not appear explicitly in Eq. (4).

We obtain a system of two linear equations with two unknowns, which is easily solved to obtain the phonon deformation potentials $\tilde{K}_{11}$ and $\tilde{K}_{12}$ plotted in Fig. 2 as a function of Ge concentration for the three optical modes of the SiGe alloy. The values corresponding to the pure materials are the ones tabulated in Ref. 1, but for Ge, they were increased in absolute value by 13.5% in order to account for the correct Grüneisen parameter $\gamma=(\tilde{K}_{11}+2\tilde{K}_{12})/6$ obtained from hydrostatic pressure experiments.[21] As already performed for GaAs (Ref. 22) and Si,[23] such a correction is necessary because of a systematic underestimation of the applied stress due to surface strain relaxation in the uniaxial-stress Raman experiments performed with a laser energy above the band gap of the material. Despite the relatively large error bars for Si rich alloys, the overall picture that

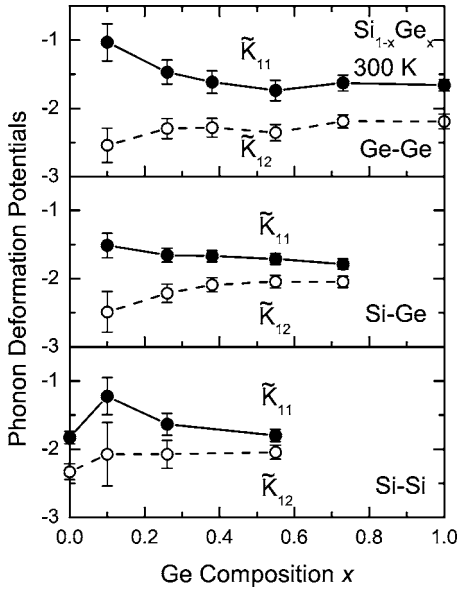

FIG. 2. Dependence on Ge concentration of the phonon deformation potentials $\tilde{K}_{11}$ and $\tilde{K}_{12}$ of the Ge–Ge, Si–Ge, and Si–Si optical modes for the SiGe material system. Solid lines are guides for the eyes.

comes out of Fig. 2 is that both deformation potentials for all SiGe alloy modes are essentially constant, exhibiting $\tilde{K}_{11}$ and $\tilde{K}_{12}$, a slight tendency to decrease or increase in absolute value with decreasing Ge content, respectively.

Using Eq. (2) and the values for the DPs of Fig. 2, one can calculate ω_0, and hence, the strain shift coefficient b_s for all phonon modes of the alloy. The resulting values are plotted in Fig. 3 as a function of the composition of the SiGe alloy. The curves represent the results of a least-squares fit to the experimental data using for all modes the same phenomenological expression given by $b_s=b_4(x-1)^4+b_0$,where x is the Ge content and b_4 and b_0 are adjustable parameters. Interestingly, $b_4=-190(15)$ cm^{-1} has a common value for all three optical modes, whereas, b_0 are $-460(20)$ cm^{-1}, $-555(15)$ cm^{-1}, and $-650(20)$ cm^{-1} for the Ge–Ge, Si–Ge, and Si–Si phonon mode, respectively. Numbers in parenthesis are the corresponding error bars. These values are in good agreement with the ones obtained by Volodin *et al.*[9] for high Ge content.

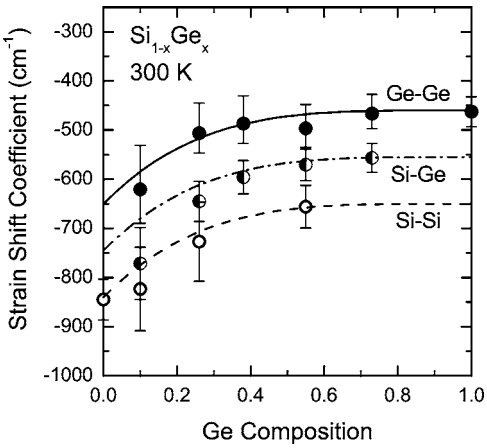

FIG. 3. Phonon strain shift coefficient b_s of the Ge–Ge, Si–Ge, and Si–Si optical modes of $Si_{1-x}Ge_x$ alloys as a function of composition. The curves represent the results of a fit to the data points using the same phenomenological polynomial function.

A comparison between our b_s values and the collection of data in Fig. 3 of Ref. 15 suggests a much better agreement with the calculations within the modified Keating model, which predict constant strain shift coefficients. This settles the issue about the discrepancies between the different experimental and theoretical reports of the literature. The main conclusion is that the strain shift coefficients of the Ge–Ge and Si–Si modes, to a good approximation, depend only slightly on composition. The strain shift coefficient of the Si–Ge mode is just the arithmetic average of the coefficients of the other two modes. Thus, the results of Fig. 3 are of great practical importance for they provide accurate values for the strain shift coefficient of the optical phonons of $Si_{1-x}Ge_x$ alloys to be used for the proper determination of the strain status of SiGe nanostructures by Raman scattering.

A.R.G. is an ICREA Research Professor. We are grateful to A. Crespi, X. Martí, J. Rius, and J. Santiso for x-ray diffraction measurements. J.S.R. acknowledges an AlBan fellowship, A.B. a FPI fellowship and PDL an I3P-CSIC grant. This work was supported by the Spanish Ministerio de Educación y Ciencia through Grant No. MAT2006-02680. Measurements were performed at MATGAS 2000 A.I.E.

[1] E. Anastassakis and M. Cardona, Semicond. Semimetals **55**, 117 (1998).
[2] F. Cerdeira, A. Pinczuk, J. C. Bean, B. Batlogg, and B. A. Wilson, Appl. Phys. Lett. **45**, 1138 (1984).
[3] D. J. Lockwood and J.-M. Baribeau, Phys. Rev. B **45**, 8565 (1992).
[4] Z. Sui, H. H. Burke, and I. P. Herman, Phys. Rev. B **48**, 2162 (1993).
[5] J. C. Tsang, P. M. Mooney, F. Dacol, and J. O. Chu, J. Appl. Phys. **75**, 8098 (1994).
[6] M. Stoehr, D. Aubel, S. Juillaguet, J. L. Bischoff, L. Kubler, D. Bolmont, F. Hamdani, B. Fraisse, and R. Fourcade, Phys. Rev. B **53**, 6923 (1996).
[7] S. Nakashima, T. Mitani, M. Ninomiya, and K. Matsumoto, J. Appl. Phys. **99**, 053512 (2006).
[8] M. I. Alonso and K. Winer, Phys. Rev. B **39**, 10056 (1989).
[9] V. A. Volodin, M. D. Efremov, A. S. Derya, and L. V. Sokolov, Semiconductors **45**, 1314 (2006).
[10] K. L. Teo, L. Qin, Z. X. Shen, and O. G. Schmidt, Appl. Phys. Lett. **80**, 2919 (2002).
[11] A. Bernardi, M. I. Alonso, J. S. Reparaz, A. R. Goñi, P. D. Lacharmoise, J. O. Ossó, and M. Garriga, Nanotechnology **18**, 475401 (2007).
[12] P. H. Tan, D. Bougeard, G. Abstreiter, and K. Brunner, J. Appl. Phys. **98**, 113517 (2005).
[13] J. S. Reparaz, A. Bernardi, A. R. Goñi, P. D. Lacharmoise, M. I. Alonso, M. Garriga, J. Novák, and I. Vávra, Appl. Phys. Lett. **91**, 081914 (2007).
[14] J. Schmidt, G. Vogg, F. Bensch, S. Kreuzer, P. Ramm, S. Zollner, R. Liu, and P. Wennekers, Mater. Sci. Semicond. Process. **8**, 267 (2005).
[15] F. Pezzoli, E. Grilli, M. Guzzi, S. Sanguinetti, D. Chrastina, G. Isella, H. von Känel, E. Wintersberger, J. Stangl, and G. Bauer, Mater. Sci. Semicond. Process. **9**, 541 (2006).
[16] D. D. Perovic, B. Bahierathan, H. Lafontaine, D. C. Houghton, and D. W. McComb, Physica A **239**, 11 (1997).
[17] E. B. Gorokhov, V. A. Volodin, D. V. Marin, D. A. Orekhov, A. G. Cherkov, A. K. Gutakovskii, V. A. Shvets, A. G. Borisov, and M. D. Efremov, Semiconductors **39**, 1168 (2005).
[18] J. P. Dismukes, L. Ekstrom, and R. J. Paff, J. Phys. Chem. **68**, 3021 (1964).
[19] R. Lange, K. E. Junge, S. Zollner, S. S. Iyer, A. P. Powell, and K. Eberl, J. Appl. Phys. **80**, 4578 (1996).
[20] G. L. Bir and G. E. Pikus, *Symmetry and Strain-Induced Effects in Semiconductors* (Halsted, New York, 1974).
[21] C. Ulrich, E. Anastassakis, K. Syassen, A. Debernardi, and M. Cardona, Phys. Rev. Lett. **78**, 1283 (1997).
[22] P. Wickbold, E. Anastassakis, R. Sauer, and M. Cardona, Phys. Rev. B **35**, 1362 (1987).
[23] E. Anastassakis, A. Cantarero, and M. Cardona, Phys. Rev. B **41**, 7529 (1990).

Measurement of phonon pressure coefficients for a precise determination of deformation potentials in SiGe alloys

J. S. Reparaz[1], A. R. Goñi[1,*], A. Bernardi[1], M. I. Alonso[1], M. Garriga[1]

[1] Institut de Ciència de Materials de Barcelona-CSIC, Esfera UAB, 08193 Bellaterra, Spain

Received XXXX, revised XXXX, accepted XXXX
Published online XXXX

PACS 63.50.Gh, 78.30.-j, 78.30.Am, 62.50.-p

* Corresponding author: e-mail goni@icmab.es, Phone +34-93-5801853, Fax +34-93-5805729

For an effective use of Raman scattering as strain characterization tool in SiGe nanostructures a precise knowledge of the phonon deformation potentials (DPs) is strictly necessary. The optical phonon DPs can be determined by means of Raman scattering measurements from the cleaved edge of a biaxially strained SiGe alloy layer grown pseudomorphically on silicon and subsequently capped. Due to uncertainties in the literature values of the unstrained phonon frequencies it turns out that the desired degree of accuracy is only attained by complementing the Raman measurements from the edge with that of the hydrostatic pressure coefficient of the optical phonons. For that purpose we have grown by molecular beam epitaxy up to seven partially strained $Si_{1-x}Ge_x$ alloys on Si spanning the entire compositional range and measured the dependence on hydrostatic pressure of the frequency of the Ge-like, Si-like and mixed Si-Ge optical modes. After correcting for the pressure dependent biaxial stress induced by the Si substrate on the alloy layer and taking into account the dependence on alloy composition of the bulk modulus we obtain a fairly constant value of the Grüneisen parameter around 1.0 for all three optical modes in the whole range of Ge contents. We also determined the strain shift coefficients for the three modes, which are essentially independent of Ge content between 0.4 and 1. Our results are in very good agreement with recent calculations of the SiGe phonon deformation potentials using a modified Keating model, which settles the longstanding issue about the large discrepancies between results from different experiments.

1 Introduction Raman scattering has demonstrated to be a powerful strain-characterization tool in compound semiconductor microstructures [1]. The accuracy of such a determination, though, depends much on the precise knowledge of the phonon deformation potentials (DPs), i.e., the derivative of the optical phonon frequency with respect to an elastic deformation of the lattice. In this respect, the situation found in the literature for the SiGe material system is particularly disappointing. There is a great deal of discrepancy between different sources about the values of the DPs mainly for intermediate Ge concentrations [2–7]. As pointed out in Ref. [5] the most probable reason for such differences arises from the fact that the actual value of the phonon frequency for the *unstrained* alloy is obtained from the literature data for bulk materials [8,9] although it appears to be sample dependent. In a recent paper [10], however, we demonstrate that it is possible to circumvent the problem posed by the exact knowledge of ω_0, the unstrained frequency of any particular phonon mode, by using its hydrostatic pressure coefficient as an additional input parameter. In this way, we were able to complement information about shifts and splitting of the phonon modes measured from the cleaved edge in samples containing strained SiGe alloy layers of different composi-

tions to obtain a linear system of two equations with two unknowns, which is solved for a precise determination of the dimensionless phonon deformation potential constants, $\tilde{K}_{11}$ and $\tilde{K}_{12}$, as defined in Ref. [1]. Needless to say that ω_0 does not appear explicitly in these equations.

In this work we present the results on the hydrostatic pressure coefficient of the three optical modes of SiGe alloys in the entire range of compositions used for the precise determination of the DPs reported in Ref. [10]. For that purpose we have grown a set of seven thick, partially strained epitaxial SiGe layers on Si with Ge concentrations between 0.1 and 1.0 and used the diamond- anvil cell technique to measure the pressure-induced shift of the optical phonons by Raman scattering. We found that the Grüneisen parameter (the logarithmic derivative of the frequency with respect to volume) for all three phonon modes is close to 1.0, being independent of the Ge content. In this way and using the results of Ref. [10], we obtained for the Ge-Ge, Si-Ge and Si-Si alloy modes the value of the so-called strain shift coefficient, defined as the ratio of the phonon frequency shift over the strain that induces that shift, as a function of alloy composition. Our results are in good qualitative agreement with recent calculations based on a modified Keating model [11].

2 Experimental A series of samples containing a thick, partially relaxed $Si_{1-x}Ge_x$ alloy layer with x=0.19, 0.26, 0.39, 0.47, 0.55, 0.74 and 1.00 was grown by molecular beam epitaxy on Si(001) substrates at a temperature of 400 °C. The growth sequence consists of deposition of a 100 nm-thick Si buffer layer followed by the SiGe alloy layer with thickness ranging between 100 and 500 nm. Such large values which are in most cases beyond the critical thickness for the given Ge content [12] were necessary to attain reasonable signal-to-noise ratios for Raman scattering inside the pressure cell. Thus, partial or even total strain relaxation of the SiGe layers is unavoidable, mainly for the higher Ge concentrations. Nevertheless, we point out that within the linear approximation (constant bulk modulus independent of pressure) the amount of strain relaxation is irrelevant for the determination of the pressure coefficient of the phonon frequency. The same holds for the correction due to the presence of the Si substrate which has a different bulk modulus than the alloy layer grown pseudomorphically on top. Finally, the composition of the alloys was determined by x-ray reciprocal space mapping along the (224) diffraction direction.

Raman spectra were collected with a LabRam HR800 system equipped with a large working distance microscope objective in backscattering geometry at room temperature using the 514.5 nm line of an Ar^+ laser. Raman peak positions are determined with an error of less than 0.5 cm^{-1}. A laser power density of 1.5 kW/cm^2 turned out to be adequate to avoid laser heating and the consequent but spurious redshift of the Raman peaks. Measurements under pressure were carried out using the diamond anvil cell

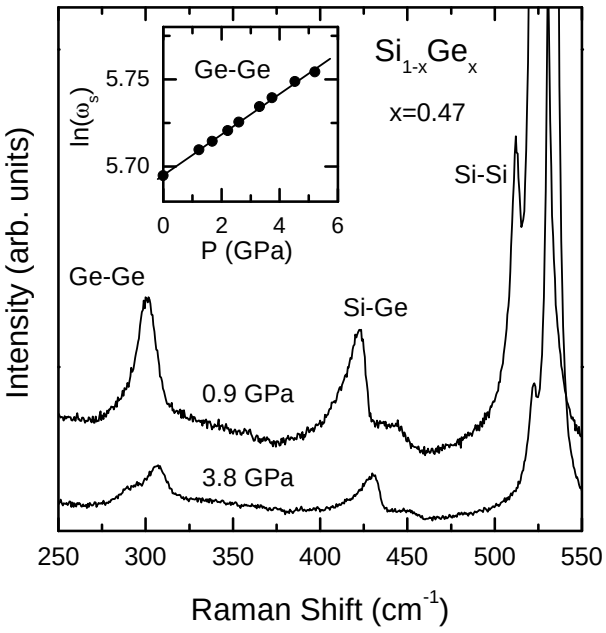

Figure 1 Two representative Raman spectra of an alloy layer with Ge content x=0.47 measured at hydrostatic pressures of 0.9 and 3.8 GPa. Peak assignment to the optical modes of the alloy is indicated. The inset shows, as an example, the values of the logarithm of the frequency for the Ge-Ge optical alloy mode as a function of pressure. The straight line represents a least-squares fit through the data points.

(DAC) technique. A 4:1 mixture of methanol and ethanol was employed as the pressure-transmitting medium. Pressure was monitored *in situ* by the shift of the Si longitudinal optical phonon, which was previously calibrated using the pressure shift of the ruby R1 line [13]. Samples loaded into the DAC were previously thinned to about 30 μm by mechanical polishing.

3 Results and Discussion The three-fold degeneracy of the optical phonon modes at the Brillouin-zone center is lifted at the alloy layer due to the tetragonal distortion of the lattice caused by the bisotropic stress induced by its lattice mismatch to Si. The zone-center phonons split into a singlet (s, vibrations in growth direction) and a doublet (d, in-plane vibrations) component. For the case of Raman measurements in backscattering geometry from the (001) surface the shift of the frequency ω_s of the Raman-allowed *singlet* component of the optical phonons is linear on the strain $\Delta\varepsilon = \frac{a_{Si}-a_0(x)}{a_0(x)}$ given by the lattice mismatch according to

$$\omega_s = \omega_0 + b_s \cdot \Delta\varepsilon. \quad (1)$$

The expression for the strain shift coefficient as a function of the DPs is given by [2,6]

$$b_s = \omega_0 \cdot (-\tilde{K}_{11} \cdot \alpha/2 + \tilde{K}_{12}). \quad (2)$$

For the case of a strictly *bisotropic* stress like in epitaxially grown pseudomorphic layers holds $\alpha = \frac{2C_{12}}{C_{11}}$, where C_{ij} are the elastic constants of the material.

In addition, the frequency shift induced by the external hydrostatic pressure in the diamond anvil cell can be also written in terms of the phonon deformation potentials as [14, 1]

$$\omega_s = \omega_0 \cdot \left(1 + \frac{\gamma P}{B_0^{SiGe}}\right), \quad (3)$$

$$\gamma = -\frac{\tilde{K}_{11} + 2\tilde{K}_{12}}{6}, \quad (4)$$

where γ is the mode Grüneisen parameter. By adding the contributions from Eqs. (1) and (3) one readily obtains for the logarithmic derivative of the phonon frequency over pressure following expression [15]

$$\frac{dln\omega_s}{dP} = \frac{\gamma}{B_0^{SiGe}} + \frac{b_s}{3\omega_0} \cdot \left(\frac{1}{B_0^{SiGe}} - \frac{1}{B_0^{Si}}\right). \quad (5)$$

The second term in Eq. (5) represents the correction to the phonon pressure coefficient due to the different elastic properties of alloy and Si substrate, which tends to reduce the lattice mismatch strain with increasing pressure. This correction amounts up to 15% for high Ge concentrations, hence, it has to be taken into account for an accurate determination of the Grüneisen parameters.

Figure 1 shows two representative spectra of the alloy with a Ge content of 0.47 measured at pressures of 0.9 and 3.8 GPa. The assignment of the optical modes corresponding to the Ge-Ge, Si-Ge and one of the Si-Si alloy vibrations is indicated [8]. To increase the signal-to-noise ratio in the DAC detection is not polarized. Thus, it is not possible to suppress contributions from second-order Raman processes by acoustic phonons in the Si substrate. This gives rise to the features around 300 and 450 cm^{-1}, which sometimes might interfere with the precise determination of the peak position mainly for the Ge-Ge mode. The position of all Raman peaks was determined by a conventional least-squares fitting procedure using asymmetric Gaussians for the Ge-Ge and Si-Ge alloy modes and a Lorentzian for the Si-Si ones. All alloy modes shift to higher frequencies with increasing pressure. As an example, we plot in the inset to Fig. 1 the logarithm of the Ge-Ge mode frequency as a function of pressure. A great advantage of this representation is that in the pressure range up to 5 GPa $ln(\omega_s)$ exhibits for all optical modes a totally linear dependence on pressure irrespective of alloy composition. Thus, the slope $\frac{dln\omega_s}{dP}$ fully characterizes the pressure behavior of the phonon modes. In contrast, a parabolic dependence is very often encountered within the conventional practice of plotting frequency against pressure, which leads to different results for the linear pressure coefficient depending on the criteria used to account for the curvature.

Using the slopes determined from linear fits to the $ln(\omega_s)$-vs.-P data points and the frequency values for zero pressure we obtained the linear pressure coefficients of the optical phonons of the alloys plotted in Fig. 2 (closed symbols) as a function of Ge content. The solid curves are guides to the eye. These data were used to complement the Raman measurements from the cleaved edge of fully stressed alloy layers for the precise determination of the phonon deformation potentials $\tilde{K}_{11}$ and $\tilde{K}_{12}$, as previously reported in Ref. [10]. With this knowledge of the DPs we make use of Eq. (5) to calculate the correction to the linear pressure coefficient due to the pressure-induced changes in the biaxial strain caused by the Si substrate. The resulting coefficients, which are plotted in Fig. 2 as open circles, correspond to the values that would be obtained for the *bulk* alloy material, i.e. for free-standing alloy samples. As pointed out before, the higher the Ge concentration, the larger is the correction due to the significant difference in bulk modulus between alloy and Si substrate. We emphasize that whereas for the Ge-Ge and Si-Ge modes at intermediate Ge concentrations the pressure coefficients obtained in Ref. [4] are about 30% larger than ours, we find very good agreement with the results of calculations within a modified Keating model [11]. We believe that in the for-

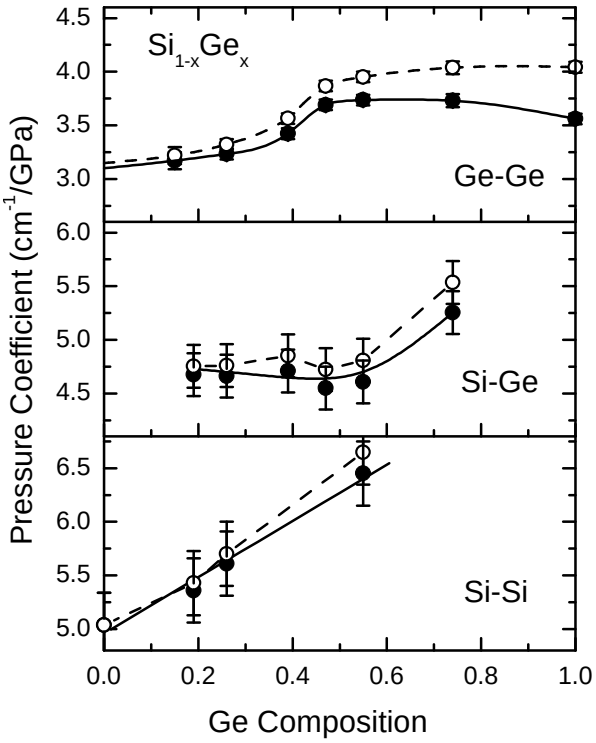

Figure 2 (closed symbols) Dependence on Ge concentration of the phonon linear pressure coefficient of the Ge-Ge, Si-Ge, and Si-Si optical modes for the SiGe material system. Open circles correspond to the values of the pressure coefficient after correction for the effect of the biaxial stress caused by the Si substrate. Solid lines are guides to the eye.

mer case the discrepancy is likely due to the polycrystalline character of the samples employed in Ref. [4].

The mode Grüneisen parameters γ are thus extracted from the corrected values of the linear pressure coefficients using Eq. (5). For the alloys the bulk modulus B_0 was obtained by linear interpolation between the ones of the pure elements [16]. Figure 3 shows the resulting γ values of the optical phonon modes of the alloys for the whole range of compositions. A striking result concerns the fact that the Grüneisen parameters of all three modes are almost constant and very similar in absolute value, being its average equal to 1.00±0.05. This is in frank contrast with several literature sources, where γ values as large as 1.3 to 1.4 are reported for intermediate Ge concentrations [4,6]. Furthermore, a constant γ implies that the observed variation of the phonon pressure coefficient with alloy composition (see Fig. 2) is due only to a change in bulk modulus. This is actually very intuitive since the Grüneisen parameters of the pure materials differ only by 5%, thus, no appreciable dependence on composition is to be expected.

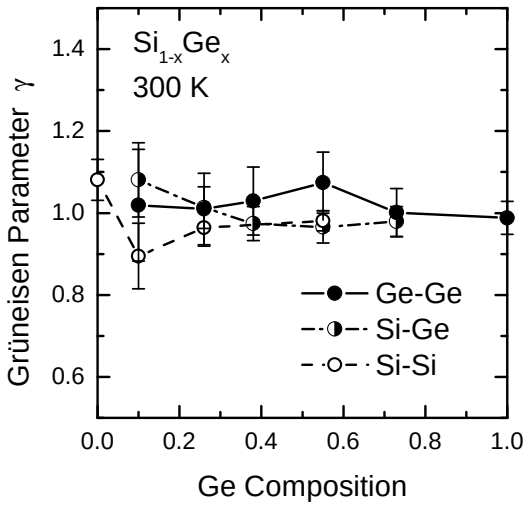

Figure 3 Mode Grüneisen parameter γ of the Ge-Ge (full circles), Si-Ge (half-filled circles) and Si-Si (open circles) optical phonons of $Si_{1-x}Ge_x$ alloys as a function of composition.

Due to its practical importance it is very instructive to compare our results for the strain shift coefficient b_s for all phonon modes of the alloy with the available literature data. b_s is readily obtained from the values for the DPs of Ref. [10] using Eq. (2). Results are plotted in Fig. 4 (full data points) as a function of composition. The dot-dashed curves represent the results of a least-squares fit to the experimental data using for all modes the same phenomenological expression given by

$$b_s = b_4 \cdot (x-1)^4 + b_0,$$

where x is the Ge content and b_4, b_0 are adjustable parameters. Interestingly, $b_4 = -190(15)$ cm^{-1} has a common value for all three optical modes, whereas b_0 is $-460(20)$ cm^{-1}, $-555(15)$ cm^{-1} and $-650(20)$ cm^{-1} for the Ge-Ge, Si-Ge and Si-Si phonon mode, respectively. Numbers in parentheses are the corresponding error bars.

Until very recently, a confusing situation was found in the literature for the accepted values of the phonon strain shift coefficients in $Si_{1-x}Ge_x$ alloys [2–7]. As illustrated in Fig. 4, for intermediate Ge concentrations in the range $0.3 \leq x \leq 0.8$ the values of b_s are 50 to 100% higher than for the pure materials, respectively. This is not only counterintuitive but recently appeared theoretical evidence [11] for b_s being nearly constant over the whole concentration range, holding this for the three optical modes of the SiGe alloy. In fact, our data are in fairly good agreement with these calculations within the modified Keating model. The agreement is also good with the b_s values of the Ge-Ge mode obtained by Volodin *et al.* [9] for high Ge content (solid straight line with small diamonds in Fig. 4).

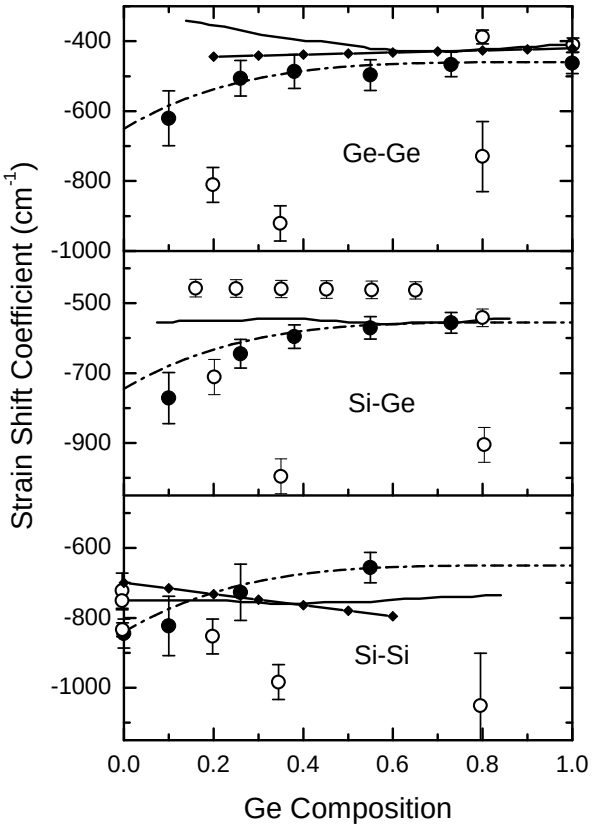

Figure 4 Phonon strain shift coefficient b_s of the Ge-Ge, Si-Ge and Si-Si optical modes of $Si_{1-x}Ge_x$ alloys as a function of composition. Closed symbols represent our results [10], open circles correspond to the experimental results of Refs. [17,7,18,11] and solid curves are the results of the Keating-model calculations [11]. The solid straight lines with the small diamonds represent the experimental results of Ref. [9].

4 Conclusions The measurements of the linear pressure coefficient for the optical phonon modes in the entire compositional range of SiGe alloys were crucial for the precise determination of the corresponding strain shift coefficients. In this way, we have settled the issue about the discrepancies between the different experimental and theoretical values for b_s. Hence, these results are of great practical relevance for they provide accurate strain shift coefficients for the optical phonon modes to be used for the proper determination of the strain status of SiGe nanostructures by Raman scattering.

Acknowledgements A.R.G. is an ICREA Research Professor. We are grateful to A. Crespi, X. Martí, J. Rius and J. Santiso for x-ray diffraction measurements. J.S.R. acknowledges financial support from the AlBan fellowship Program. A.B. acknowledges an FPI fellowship. This work was supported in part by the Spanish Ministerio de Educación y Ciencia through grant MAT2006-02680. Measurements were performed at the Nanotechnology Laboratory of MATGAS 2000 A.I.E.

References

[1] E. Anastassakis and M. Cardona, Semicond. Semimetals **55**, 117 (1998) and references therein.
[2] F. Cerdeira, A. Pinczuk, J. C. Bean, B. Batlogg, and B. A. Wilson, Appl. Phys. Lett. **45**, 1138 (1984).
[3] D. J. Lockwood and J. M. Baribeau, Phys. Rev. B **45**, 8565 (1992).
[4] Z. Sui, H. H. Burke, and I. P. Herman, Phys. Rev. B **48**, 2162 (1993).
[5] J. C. Tsang, P. M. Mooney, F. Dacol, and J. O. Chu, J. Appl. Phys. **75**, 8098 (1994).
[6] M. Stoehr, D. Aubel, S. Juillaguet, J. L. Bischoff, L. Kubler, D. Bolmont, F. Hamdani, B. Fraisse, and R. Fourcade, Phys. Rev. B **53**, 6923 (1996).
[7] S. Nakashima, T. Mitani, M. Ninomiya, and K. Matsumoto, J. Appl. Phys. **99**, 053512 (2006).
[8] M. I. Alonso and K. Winer, Phys. Rev. B **39**, 10056 (1989).
[9] V. A. Volodin, M. D. Efremov, A. S.Derya, and L. V. Sokolov, Semicond. **45**, 1314 (2006).
[10] J. S. Reparaz, A. Bernardi, A. R. Goñi, M. I. Alonso, and M. Garriga, Appl. Phys. Lett. **92**, 081909 (2008).
[11] F. Pezzoli, E. Grilli, M. Guzzi, S. Sanguinetti, D. Chrastina, G. Isella, H. von Känel, E. Wintersberger, J. Stangl, and G. Bauer, Mat. Sci. Semicond. Processing **9**, 541 (2006).
[12] D. D. Perovic', B. Bahierathan, H. Lafontaine, D. C. Houghton, and D. W. McComb, Physica A **239**, 11 (1997).
[13] H. K. Mao, J. Xu, and P. M. Bell, J. Geophy. Res. **91**, 4673 (1986).
[14] G. L. Bir and G. E. Pikus, Symmetry and Strain-induced Effects in Semiconductors (Halsted Press, New York, 1974).
[15] J. S. Reparaz, A. Bernardi, A. R. Goñi, P. D. Lacharmoise, M. I. Alonso, M. Garriga, J. Novák, and I. Vávra, Appl. Phys. Lett. **91**, 081914 (2007).
[16] Numerical Data and Functional Relationships in Science and Technolog, Landolt-Börnstein, New Series Vol. 17, edited by O. Madelung, H. Weiss, and M. Schulz (Springer, Heidelberg, 1982), Sec. 2, p. 64 and 107.
[17] J. Schmidt, G. Vogg, F. Bensch, S. Kreuzer, P. Ramm, S. Zollner, R. Liu, and P. Wennekers, Mat. Sci. Semicond. Processing **8**, 267 (2005).
[18] K. Brunner, EMIS Datarev., 115 (1999).

3.1.3 Conclusions

In this section results on the compositional dependence of phonon deformation potentials in SiGe alloys were presented. From these potentials the Grüneisen parameter and phonon strain shift coefficient are readily calculated. Concerning the Grüneisen parameter, discrepancies with previous results were found for the intermediate compositional range. The performed measurements indicate that this parameter is approximately constant with Ge content.

The determination of the singlet to doublet splitting in strained alloys provided the key for a precise measurement of $\tilde{K}_{11}$ and $\tilde{K}_{12}$ and, using our results for the Grüneisen parameter, the problem of the frequency at zero strain (ω_0) determination was avoided. An interesting property of this approach is that the applied method is independent of the studied material system.

Finally, the compositional dependence of these potentials has been fully addressed in the two presented publications. These results are important also concerning applications since for a good determination of the strain status in SiGe alloys and other SiGe-based nanostructures a precise knowledge of the strain-shift coefficient is mandatory.

Bibliography

[1] J. C. Bean, L. C. Feldman, A. T. Firoy, and R. T. Lynch Appl. Phys. Lett. **44**, 102 (1984).

[2] F. Cerdeira, A. Pinczuk, J. C. Bean, B. Batlogg, and B. A. Wilson, Appl. Phys. Lett. **45**, 1138 (1984).

[3] M. A. Renucci, J. B. Renucci, and M. Cardona, *in Light Scattering in Solids*, edited by M. Balkanski (Flammarion, Paris, 1971), p. 326.

[4] M. I. Alonso, and A. K. Winer, Phys. Rev. B **39**, 10056 (1989).

[5] *"Fundamentals of Semiconductors"*, Peter Y. Yu and Manuel Cardona, Springer.

[6] D. J. Lockwood, and J. M. Baribeau, Phys. Rev. B **45**, 8565 (1992).

[7] F. Pezzoli, E. Grilli, M. Guzzi, S. Sanguinetti, D. Chrastina, G. Isella, H. von Knel, E. Wintersberger, J. Stangl, and G. Bauer, Mat. Sci. Semicond. Processing **9**, 541 (2006).

[8] J. Schmidt, G. Vogg, F. Bensch, S. Kreuzer, P. Ramm , S. Zollner, *et. al.*, Mat. Sci. Semicond. Process. **8**, 267 (2005).

[9] S. Nakashima, T. Mitani, M. Ninomiya, and K. Matsumoto, J. Appl. Phys. **99**, 053512 (2006).

[10] F. Cerdeira, C. J. Buchenauer, F. H. Pollak, and M. Cardona, Phys. Rev B **5**, 580 (1972).

[11] J. B. Renucci, M. A. Renucci, and M. Cardona, Sol. Stat. Comm. **9**, 1651 (1971).

[12] Z. Sui, H. H. Burke, and I. P. Herman, Phys. Rev. B **48**, 2162 (1993).

3.2 Ge/Si Quantum Dots

The determination of the strain status of capped quantum dots has been a subject of interest during the last decades. A precise knowledge of the strain within the dots is crucial to study their elastic and opto-electronic properties. Concerning Ge/Si systems not much experimental work is found in this field, leading in some cases to incorrect values of the strain in the dots. The reason behind this situation is that the strain status for these systems is highly dependent on dot shape and aspect ratio. In this sense, the lack of knowledge about the strain status makes uncertain the prediction of some of their physical properties. In this section some previous theoretical and experimental work will be presented. Finally, an experiment especially designed in order to determine the strain status of Si-capped Ge quantum dots will be introduced.

3.2.1 Motivation and Previous Work

Vertically self-ordered QDs raise many fundamental questions concerning the nature of stress distribution. It is well established that stresses play an important role in both the mechanism and resulting structure of island vertical self-organization. It is of value, therefore, to examine the nature of stresses. In the last decade, several theoretical articles were published in order to explain the strain propagation from a single QD layer to subsequent layers after capping the first one. This effect is of great importance since understanding the strain propagation in the spacer is the key to perform multi-layer dot engineering.

Although there is a considerable amount of calculations concerning the strain propagation [1-6], only the approach used by *Makeev* and *Madhukar* (see Ref. [7]) will be presented here since it was considered the most instructive. Nevertheless, *Pryor et. al.* have made an interesting contribution by comparing different approaches to the strain determination problem [8].

Makeev and *Madhukar* reported an atomistic simulation study of the stresses induced by pyramidal island QDs buried in a matrix with emphasis on the dependence of the spacer-layer surface stress on the island volume and the spacer layer thickness. In Fig. 3.5 a sketch of the QDs studied is shown. Pyramidal QDs were used since most of the samples grown had this dot morphology. Their method of calculation is as follows: initially all the atoms are placed in the bulk Si(001) atomic positions. The system is relaxed to the minimum total energy state using the conjugate gradient minimization algorithm. The minimization was performed until the net force on each atom does not exceed a certain threshold. In their convention, tensile stress corre-

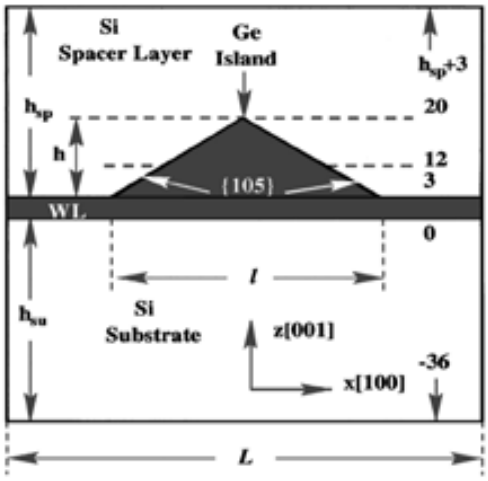

Figure 3.5: Schematic illustration of the modeled Ge QD system. Germanium island of height h (with WL of 3 ML underneath) is positioned on a Si(001) substrate of thickness h_{su} and covered by Si spacer layer of thickness h_{sp}. The lateral size of the simulation box is L=60a_{Si} and the lateral island size is l. Here a_{Si}= 5.430 Å is the lattice constant of Si. Numbers correspond to the z coordinate measured in ML, N_z. Extracted from Ref. [7].

sponds to positive sign and compressive to the negative one. The obtained stress on the cap layer is shown in Fig. 3.6. The stress on the cap layer is strongly dependent on the cap layer thickness, i.e., the stress on the cap reduces as this grows thicker. They have also shown that the strain within the QD is also directly related to the cap layer thickness, i.e., the internal strain of the dots rises as the cap layer thickness increases. This effect is usually known as *re-compression* of the island due to the presence of the cap layer. This work is very useful to understand the typical distances of decay of the strain field in these systems, thus, enabling the design of complex strain driven structures.

An interesting experimental approach to the problem of strain determination was carried out by *Teo et. al.* (see Ref. [9]). They have investigated the effect of a Si cap layer on pyramidal Ge dots. By measuring the zone center optical phonon pressure coefficient they were able to observe changes in the elastic properties of the dots covered with a Si cap layer. For this purpose they used the typical DAC high pressure technique described previously in this work. Fig. 3.7 shows typical spectra extracted from Ref. [9]. Around 300 cm^{-1} two peaks are observed arising from the second-order acoustical

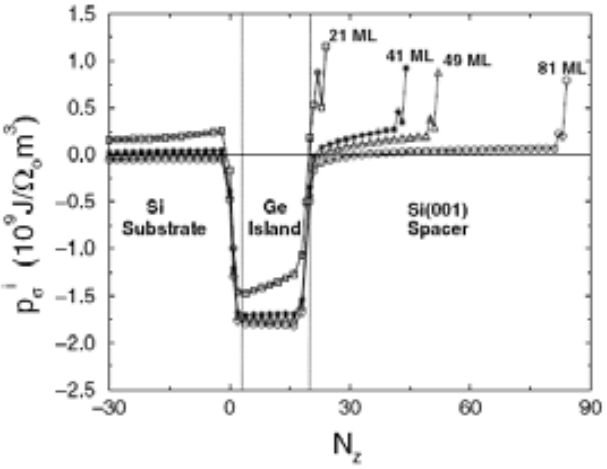

Figure 3.6: The hydrostatic stress p_σ^i variation with atomic plane number N_z along the line passing through the island base center and apex. Different curves are for different spacer layer thicknesses: $h_{sp} = 81$ ML (circles); $h_{sp} = 49$ ML (triangles); $h_{sp} = 41$ ML (stars); $h_{sp} = 21$ ML (squares). Dashed vertical lines mark the island base and top. Here, $\Omega_0 = \Omega/a_{Si}^3$, where Ω is the average atomic volume as defined in Ref. [12]. Extracted from Ref. [7].

phonon from the Si substrate (2TA, lower in energy and with $d\omega/dP < 0$) and from the Ge-Ge optical vibration (higher and with $d\omega/dP > 0$). After measuring several spectra for different applied pressures they were able to obtain $\omega(P)$ for the Ge-Ge optical phonon as:

$$\omega_{Ge}(P) = (308.5 \pm 0.4) + (2.9 \pm 0.3)P + (0.02 \pm 0.04) \times 10^{-3}P^2, \tag{3.7}$$

where P is the external applied pressure in GPa and the frequencies ω are measured in cm^{-1}.

In order to explain the importance of the previous equation we need an expression that relates the phonon pressure coefficient to its basic constituents, which can be written as follows:

$$\frac{d\omega}{dP} = -\frac{\omega_0}{6}(\tilde{K}_{11} + 2\tilde{K}_{12}) \left[\frac{1}{B_0^{Si}} + \varphi \left(\frac{1}{B_0^{Ge}} - \frac{1}{B_0^{Si}} \right) \right], \tag{3.8}$$

where $0 < \varphi < 1$ is a parameter describing the degree of relaxation of the dots. The deduction of this equation can be followed from Ref. [10].

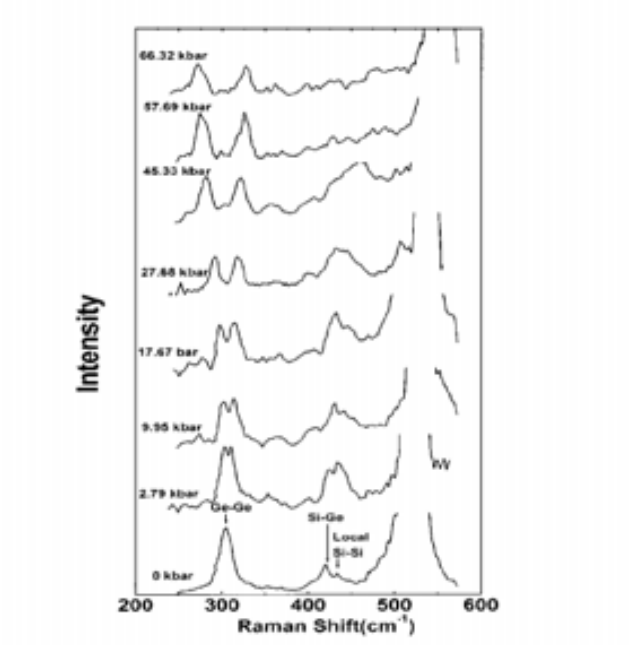

Figure 3.7: Room-temperature Raman spectra at various pressures for Si capped Ge QDs. Extracted from Ref. [9].

Two limiting cases are well established: i) When $\varphi = 1$ the QDs are totally relaxed and their pressure coefficient is the one given by the hydrostatic term $-\omega_0(\tilde{K}_{11} + 2\tilde{K}_{12})/6B_0^{Ge}$. In this case we obtain $d\omega/dP \approx 4$ cm^{-1}/GPa as in bulk Ge. ii) For the limiting case where the Ge dots are surrounded by a quasi-infinite Si medium $\varphi = 0$ and the obtained pressure coefficient is $d\omega/dP \approx 3.2$ cm^{-1}/GPa. These two cases were calculated using $\omega_0 \approx 300$ cm^{-1}, and the values for $\tilde{K}_{ij}$ were extracted from Ref. [11].

Teo et. al. have measured $d\omega/dP = 2.9 \pm 0.3$ cm^{-1}/GPa (linear term in Eq. (3.7)). Following the previous analysis this result corresponds to the case ii), the surrounding media is large enough in volume to impose its own elastic properties to the QDs. This result was confirmed in slightly different samples of Ge QDs and presented in a publication in the next section entitled *"Raman scattering of capped and uncapped carbon-induced Ge dots under hydrostatic pressure"* (Complementary Article: A).

The next step was to investigate the strain status of the QDs as a function of Si cap-layer thickness. For this purpose a series of samples with identical QDs but different cap layers with thicknesses between 3 and 200 nm were grown. A clear dependence of the pressure coefficient on cap layer thickness

was found, revealing a different strain status of the dots for each cap layer. A *biaxial* to *hydrostatic* strain status transition within the dots upon variation of the cap layer thickness was found. Thin cap layers corresponds to a *biaxial* strain status whereas thicker ones to an *hydrostatic* strain status in the dots. These results are presented in the next section in the article entitled *"Phonon pressure coefficient as a probe of the strain status of self-assembled quantum dots"* (Article Number: 3).

Finally, a third publication is also presented in the following section in which the results of the previous article (Article Number: 3) were used to study a sample with a bimodal distribution of Ge dots. Using the obtained dependence of the pressure coefficient on Si cap layer thickness we were able to correlate a double peak structure around the Ge-Ge mode with the bimodal dot distribution. The presented article is entitled *"Polarized Raman study of self-assembled Ge/Si dots under hydrostatic pressure"* (Article Number: 4).

3.2.2 Experiments and Results

Article n: 3

Title: Phonon pressure coefficient as a probe of the strain status of self-assembled quantum dots

Authors: J. S. Reparaz, A. Bernardi, A. R. Goñi, P. D. Lacharmoise, M. I. Alonso, M. Garriga, J. Novák, and I. Vávra.

Journal: Applied Physics Letters

Article n: 4

Title: Polarized Raman study of self-assembled Ge/Si dots under hydrostatic pressure

Authors: J. S. Reparaz, A. Bernardi, A. R. Goñi, M. I. Alonso, and M. Garriga.

Journal: Physica Status Solidi b

Complementary Article: A

Title: Raman scattering of capped and uncapped carbon-induced Ge dots under hydrostatic pressure

Authors: A. Bernardi, J. S. Reparaz, A. R. Goñi, M. I. Alonso, and M. Garriga.

Journal: Physica Status Solidi b

Phonon pressure coefficient as a probe of the strain status of self-assembled quantum dots

J. S. Reparaz,[a] A. Bernardi, A. R. Goñi, P. D. Lacharmoise, M. I. Alonso, and M. Garriga
Institut de Ciència de Materials de Barcelona-CSIC, Esfera UAB, 08193 Bellaterra, Spain

J. Novák and I. Vávra
Institute of Electrical Engineering, Slovak Academy of Sciences, 841 04 Bratislava, Slovakia

(Received 11 May 2007; accepted 31 July 2007; published online 23 August 2007)

The built-in strain in self-assembled quantum dots has large impact on their physical properties, but both its average value and degree of anisotropy are often unknown. The authors demonstrate that the pressure coefficient of optical phonons might be used as probe for the strain status of the dots. This method was applied to the case of Ge dots capped with Si layers of different thicknesses. The authors observe a transition from a strictly biaxial stress situation for uncapped dots to a status of quasihydrostatic strain for cap-layer thicknesses larger than a critical value of the order of the dot height. © *2007 American Institute of Physics*. [DOI: 10.1063/1.2773958]

Self-assembled quantum dots (QDs) are fundamental building blocks in optoelectronics nowadays[1] for their electronic, optical, and transport properties can be tailored by controlling dot parameters such as size, shape, and composition.[2] Another key parameter which is inherent to self-assembled growth and which has large influence on the optoelectronic properties of the dots is the residual built-in strain. Unfortunately, the strain status of the dots in the ready device is usually unknown. In this respect, Raman scattering has been demonstrated to be a powerful tool for measuring strain in compound semiconductor microstructures.[3] For the most frequent case of Raman measurements in backscattering geometry from the (001) surface, the strain is directly determined from the frequency shift of the Raman-allowed *singlet* component of the optical phonons according to[4,5] $\omega_s(x,\varepsilon)=\omega_0+b_s\varepsilon_\parallel$, where x is the alloy composition, $\varepsilon_\parallel$ is the in-plane strain, and b_s is the so-called strain-shift coefficient given by

$$b_s=\omega_0(-\tilde{K}_{11}\alpha/2+\tilde{K}_{12}). \tag{1}$$

Here, ω_0 is the frequency of the unstrained phonon mode, $\tilde{K}_{ij}$ are the dimensionless phonon deformation potentials, as defined in Ref. 3, and $\varepsilon_\perp=-\alpha\varepsilon_\parallel$ is the relation between in-plane strain and that in the growth direction.

Equation (1) was deduced for the case of a strictly biaxial stress like that in quantum wells, for which $\alpha=2C_{12}/C_{11}\approx 1$, where C_{ij} are the elastic constants of the material. It also holds for a purely hydrostatic strain just by setting $\alpha=-1$, because in this case all three strain components along the principal axes are the same. In the general case of dealing with a mixed stress tensor containing a hydrostatic and a biaxial component, one might, in principle, still be using Eq. (1) but with an unknown value of the parameter α lying between ±1. Such is too often the situation for self-assembled QDs depending on the aspect ratio and cap-layer thickness. Thus, it is not surprising to find in the literature a wide spread of values for the strain-shift coefficient b_s. For Ge/Si thin films and/or QDs, for instance, b_s ranges from about −400 to −800 cm^{-1}.[5–12] The conclusion is that in order to obtain sound quantitative results from Raman scattering for the residual strain in QD systems, it is crucial to know the strain situation, i.e., which is the pertinent value for α.

In this letter, we show that the pressure coefficient of the longitudinal optical phonon ($d\omega_s/dP$) can be regarded as a probe of the strain status of quantum dots. The main reason for using the pressure derivative of the phonon frequency instead of the frequency itself is that the former is to a very good approximation only sensitive to the strain distribution rather than QD composition, size, or even the presence of dislocations. For that purpose we have studied systematically the hydrostatic pressure coefficient of the optical phonon of a series of carbon-induced Ge dots capped with a layer of Si with different thicknesses ranging from 0 to 200 nm. With increasing cap-layer thickness we observe a steep decrease of the phonon-pressure coefficient followed by saturation. Based on the results of a simple elastic model which accounts for the pressure dependence of the phonon frequency, we interpret this behavior as indication of a transition from a purely biaxial stress situation for uncapped dots to a status of quasihydrostatic compression for dots embedded in the Si matrix.

Samples were grown by molecular beam epitaxy on Si(001) substrates according to the following sequence: after deposition of a 100-nm-thick Si buffer layer, a 4.8 Å thick Ge wetting layer was grown before depositing 0.1 ML of carbon to control the shape and density of the QDs.[13–15] In the next step, 15 Å of Ge were grown at 500 °C leading to dot formation. Finally, the Ge QDs were capped with either 0, 3, 10, 50, or 200 nm of Si also at 500 °C. The reference sample without cap layer was used to determine the dot shape and density using atomic force microscopy (AFM). As shown in Figs. 1(a) and 1(b), the average dot height is about $h=14$ nm, the base length is $b=120$ nm, and the areal density is about 40 dots/$\mu\mathrm{m}^2$. In Fig. 1(c), we show a representative transmission electron microscopy (TEM) image of a Ge dot. The cap layer can be easily identified, as it copies the QD shape.

Raman spectra were collected with a LabRam HR800 system in backscattering geometry at room temperature using the 514.5 nm line of an Ar^+ laser. Raman peak positions are determined with an error of less than 0.5 cm^{-1}. Measurements under pressure were carried out using the diamond

[a]Electronic mail: sebareparaz@hotmail.com

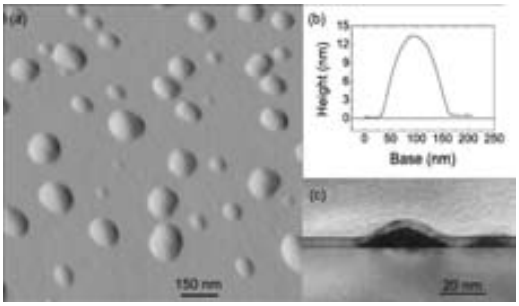

FIG. 1. (a) Topographic image by AFM of the uncapped sample and (b) line scan across a representative carbon-induced Ge quantum dot. (c) TEM image of the sample with 10-nm-thick cap layer showing one Ge dot in cross section.

anvil cell (DAC) technique. A 4:1 mixture of methanol and ethanol was employed as the pressure-transmitting medium. Pressure was monitored *in situ* by the shift of the Si longitudinal optical phonon, which was previously calibrated using the pressure shift of the ruby R1 line.[16] Samples loaded into the DAC were previously thinned to about 30 μm by mechanical polishing.

Figure 2 displays the dependence on hydrostatic pressure of the frequency of the Raman peak corresponding to the Ge optical phonon for five samples with cap-layer thickness, as indicated in the legend. We show only data in the pressure range up to 5 GPa, in which the pressure dependence of ω_s is well described by a straight line. The solid lines in Fig. 2 represent the results of least-squares fits to the data points using a linear relation.[17] The fit results are listed in Table I. The phonon pressure coefficient $(d\omega_s/dP)$ obtained from the fitted slopes exhibits a clear decreasing trend with increasing cap-layer thickness.

In Fig. 3 we have plotted the tabulated values of the phonon pressure coefficient as a function of cap-layer thickness. A fast exponential reduction of $d\omega_s/dP$ is observed for thicker Si caps. Preliminary results on smaller Ge QDs were published elsewhere.[18] To explain this behavior we developed a simple elastic model which takes into account the effects of the wetting layer (WL) and dot capping on the dot residual strain. We consider three contributions to the coefficient $d\omega_s/dP$. The obvious one is from the external hydrostatic pressure and the two arise from changes in the built-in strain of the QDs indirectly induced by the applied pressure due to the different compressibilities, i.e., bulk modulus of

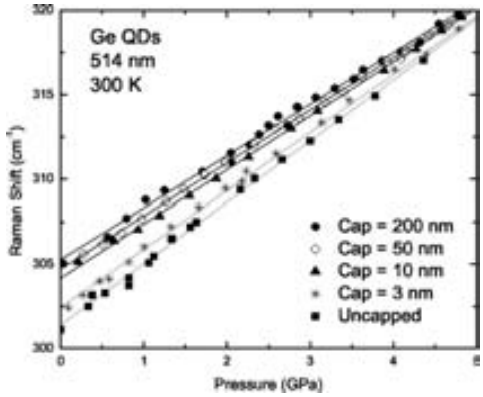

FIG. 2. Dependence on pressure of the frequency of the Ge longitudinal optical phonon mode for five samples with cap layer thicknesses of 0, 3, 10, 50, and 200 nm. Solid lines are results of least-squares fits to the data points using linear relations.

TABLE I. Coefficients describing the pressure dependence of the Raman-allowed optical phonon of Ge dots capped with a Si layer of different thicknesses t obtained from fits of a linear expression $\omega_s=\omega_0+(d\omega_s/dP)\cdot P$ to the experimental data. Error bars are indicated in parenthesis.

Cap (nm)	ω_0 (cm^{-1})	$d\omega_s/dP$ (cm^{-1}/GPa)
0	301.4(1)	3.72(4)
3	302.4(2)	3.54(3)
10	304.2(2)	3.29(3)
50	305.2(2)	3.16(3)
200	304.7(2)	3.20(3)

the dot and surrounding material which we labelled hereafter B and A, respectively. From the latter contributions one corresponds to the biaxial deformation caused by the wetting layer and the other comes from the recompression of the dots during capping.

For hydrostatic pressures up to a few gigapascals, the reduction in relative volume is proportional to the applied pressure, $\Delta V/V \approx -P/B_0$, where B_0 is the bulk modulus. The corresponding contribution to the phonon pressure coefficient is simply given by

$$\frac{d\omega_s^{(P)}}{dP} = -\frac{a}{B_0^B}, \quad \text{with } a = \frac{\omega_0}{6}(\tilde{K}_{11} + 2\tilde{K}_{12}), \tag{2}$$

the hydrostatic phonon deformation potential.[3] For $B \equiv$ Ge is $-a/B_0^{\mathrm{Ge}} \approx 4$ cm^{-1}/GPa,[19] which constitutes an upper bound for the phonon pressure coefficient of the dots.

Although the residual QD strain is not known *a priori*, the way it varies by applying hydrostatic pressure due to the different elastic properties of the dot and surrounding material is readily estimated as $d\varepsilon_{\parallel}/dP = 1/3(1/B_0^B - (1/B_0^A))$. In the present case, we have A $\equiv$ Si with $B_0^{\mathrm{Si}}=98$ GPa and $B \equiv$ Ge with $B_0^{\mathrm{Ge}}=75$ GPa.[20] Let us first consider the case of uncapped dots, for which there is a strictly biaxial stress situation due to the constraint of isomorphism to the Si substrate. Since such stress is transduced to the dot through the wetting layer, we call it the WL contribution. The dot, however, relaxes its strain by expanding laterally, as it grows in height h. Thus, the measured blueshift of the QD phonon would be smaller by a phenomenological factor φ than is mandatory after Eq. (1). This factor is expected to depend on aspect ratio and WL composition but not on pressure. Hence, the contribution of the biaxial stress to the phonon pressure coefficient can be written as

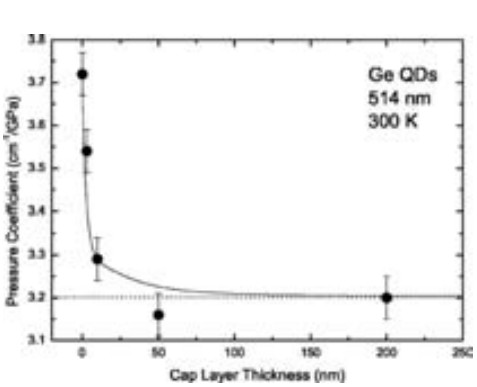

FIG. 3. Phonon pressure coefficient of Ge optical mode of the dots vs cap layer thickness as obtained from the slopes of the fits in Fig. 2. The solid curve represents the result of a fit to the data points using Eqs. (2), (3), and (5) with λ as adjustable parameter.

$$\frac{d\omega_s^{(\mathrm{WL})}}{dP} = \varphi b_s \frac{d\varepsilon_{\parallel}}{dP} = \frac{\varphi b_s}{3}\left(\frac{1}{B_0^B} - \frac{1}{B_0^A}\right). \tag{3}$$

The effect of capping the dots with a layer of thickness t is twofold: On the one hand, the cap layer produces a hydrostatic recompression of the dots and, on the other hand, the expansion in the growth direction due to the biaxial compression induced by the WL is gradually suppressed with increasing t. The latter supposes for the parameter φ a phenomenological dependence on t, $\varphi = \varphi_0 e^{-t/\lambda}$, with λ a critical cap-layer thickness. The amount of recompression caused by capping is a function of the ratio of the cap layer volume V_c to the volume of the dot V_d, in order to minimize the total elastic energy of the dot/cap system. Inspired by TEM pictures like that of Fig. 1(c) we consider for the calculation of the elastic energy a dot shape of a half revolution ellipsoid with an aspect ratio $f=b/h$ surrounded by a Si layer of thickness t ($g=t/h$). The minimum energy is attained for a dot strain of

$$\varepsilon_d = \frac{\varepsilon_{\parallel}}{1 + (V_d/V_c)(B_0^B/B_0^A)}, \quad \frac{V_d}{V_c} = \frac{f^2}{(f+g)^2}\frac{(1+g)^2}{(1+g)^3 - 1}. \tag{4}$$

Considering this strain as hydrostatic, it yields for the contribution of the cap layer to the phonon pressure coefficient the term

$$\frac{d\omega_s^{(\mathrm{cap})}}{dP} = \frac{a}{1 + (V_d/V_c)(B_0^B/B_0^A)}\left(\frac{1}{B_0^B} - \frac{1}{B_0^A}\right). \tag{5}$$

The solid line in Fig. 3 is the result of a least-squares fit to the experimental data of $d\omega_s/dP$ using the function which consists of the three terms given by Eqs. (2), (3), and (5). Here, λ is the only adjustable parameter, since φ_0 is determined by comparing the value of $d\omega_s/dP$ for the uncapped dots to that of bulk Ge. In spite of the crudeness of the model, we obtain a good description of the behavior of the phonon pressure coefficient with cap-layer thickness for $\lambda = 8$ nm. Even more important is the fact that the model provides further insight into the strain status of self-assembled dots, leading to a deeper understanding of the high pressure results. For example, the meaning of the saturation value of the pressure coefficient is the following: When $t \to \infty$, $\varphi \to 0$ and $V_d/V_c \to 0$ too. The term $d\omega_s/dP^{(\mathrm{WL})}$ vanishes and the other two yield $d\omega_s/dP = -a/B_0^A \approx 3.2\ \mathrm{cm}^{-1}/\mathrm{GPa}$ (A $\equiv$ Si), which is the pressure coefficient calculated with the hydrostatic deformation potential of Ge but using the bulk modulus of the Si matrix. In fact, a similar pressure coefficient has been reported by Teo *et al.* for a sample with Ge QDs capped with 200 nm of Si.[21] This led us to the conclusion that there is an abrupt transition from a strictly biaxial stress situation of uncapped dots to a fully hydrostatic (isotropic) three-dimensional compression state of the dots for cap layers thicker than the critical value λ (8 nm in the present case). We emphasize that this result is independent of the model; the latter is helpful to understand the underlying physics.

Obviously, λ depends on f. For very flat dots one expects $\lambda \to \infty$, thus, the dots, capped or uncapped, are always in a state of biaxial compression like the wetting layer. In fact, Raman measurements from the cleaved edge of a QD sample containing very flat dots ($h \approx 2$ nm) exhibit a clear singlet-doublet splitting,[6,8] which is evidence of biaxial strain. On the contrary, our sample with a 200-nm-thick cap layer does not display any splitting, being indicative of a hydrostatic (isotropic) compression of the Ge dots.

The practical importance of this work is to provide a means to infer the proper strain situation which applies for a given quantum dot structure, independent of the material system. Our pressure experiments indicate that for QDs with heights larger than about 5 nm or with steep facets like dome-shaped dots, if the cap layer is of the order of the dot height or above, then to consider a quasihydrostatic strain status is appropriate. On the contrary, for very flat or uncapped dots their deformation is better accounted for using a biaxial stress tensor. This would allow for the proper use of Eq. (1) with the correct value of the parameter α for the determination of the mean dot strain by Raman scattering.

One of the authors (J.S.R.) acknowledges financial support from the AlBan fellowship Program. Another author (A.B.) acknowledges an FPI fellowship and P.D.L. an I3P-CSIC grant. Another author (A.R.G.) is an ICREA Research Professor. This work was supported in part by the Spanish Ministerio de Educación y Ciencia through grant MAT2006-02680.

[1] *Nano-Optoelectronics*, edited by M. Grundmann (Springer, Berlin, 2002), pp. 299–428.
[2] J. Stangl, V. Holý, and G. Bauer, Rev. Mod. Phys. **76**, 725 (2004).
[3] E. Anastassakis and M. Cardona, Semicond. Semimetals **55**, 117 (1998) and references therein.
[4] F. Cerdeira, A. Pinczuk, L. C. Bean, B. Batlogg, and B. A. Wilson, Appl. Phys. Lett. **45**, 1138 (1984).
[5] M. Stoehr, D. Aubel, S. Juillaguet, J. L. Bischoff, L. Kubler, D. Bolmont, F. Hamdani, B. Fraisse, and R. Fourcade, Phys. Rev. B **53**, 6923 (1996).
[6] P. H. Tan, K. Brunner, D. Bougeard, and G. Abstreiter, Phys. Rev. B **68**, 125302 (2003).
[7] K. L. Teo, L. Qin, Z. X. Shen, and O. G. Schmidt, Appl. Phys. Lett. **80**, 2919 (2002).
[8] P. H. Tan, D. Bougeard, G. Abstreiter, and K. Brunner, J. Appl. Phys. **98**, 113517 (2005).
[9] A. V. Baranov, A. V. Fedorov, T. S. Perova, R. A. Moore, S. Solosin, V. Yam, D. Bouchier, and V. Le Thanh, J. Appl. Phys. **96**, 2857 (2004).
[10] A. V. Baranov, A. V. Fedorov, T. S. Perova, R. A. Moore, V. Yam, D. Bouchier, V. Le Thanh, and K. Berwick, Phys. Rev. B **73**, 075322 (2006).
[11] M. Ya. Valakh, V. O. Yukhymchuk, V. M. Dzhagan, O. S. Lytvyn, A. G. Milekhin, A. I. Nikiforov, O. P. Pchelyakov, F. Alsina, and J. Pascual, Nanotechnology **16**, 1464 (2005).
[12] V. A. Volodin, M. D. Efremov, A. S. Deryabin, and L. V. Sokolov, Semiconductors **40**, 1314 (2006).
[13] A. Bernardi, M. I. Alonso, A. R. Goñi, J. O. Ossó, and M. Garriga, Appl. Phys. Lett. **89**, 101921 (2006).
[14] A. Bernardi, J. O. Ossó, M. I. Alonso, A. R. Goñi, and M. Garriga, Nanotechnology **17**, 2602 (2006).
[15] A. Bernardi, M. I. Alonso, A. R. Goñi, J. O. Ossó, and M. Garriga, Surf. Sci. **601**, 2783 (2007).
[16] H. K. Mao, J. Xu, and P. M. Bell, J. Geophys. Res. **91**, 4673 (1986).
[17] At ambient pressure the frequency of the second-order Raman feature associated to scattering by two transverse acoustic phonons of Si (2TA) is similar to that of the Ge–Ge mode. Nevertheless, for our dots the Ge peak is about ten times more intense than the 2TA feature, thus, having no influence on the determination of the pressure coefficient of the Ge mode. Moreover, both peaks shift with pressure in opposite directions, leading to an increased peak separation with pressure.
[18] A. Bernardi, J. S. Reparaz, A. R. Goñi, M. I. Alonso, and M. Garriga, Phys. Status Solidi B **244**, 76 (2007).
[19] C. Ulrich, E. Anastassakis, K. Syassen, A. Debernardi, and M. Cardona, Phys. Rev. Lett. **78**, 1283 (1997).
[20] *Numerical Data and Functional Relationships in Science and Technology*, Landolt-Börnstein, New Series Vol. 17, edited by O. Madelung, H. Weiss, and M. Schulz (Springer, Heidelberg, 1982), Sec. 2, p. 64 and p. 107.
[21] K. L. Teo, L. Qin, I. M. Noordin, G. Karunasiri, Z. X. Shen, O. G. Schmidt, K. Eberl, and H. J. Queisser, Phys. Rev. B **63**, 121306 (2001).

Polarized Raman study of self-assembled Ge/Si dots under hydrostatic pressure

J. S. Reparaz*, A. Bernardi, A. R. Goñi, M. I. Alonso, and M. Garriga**

Institut de Ciència de Materials de Barcelona (ICMAB), CSIC, Esfera UAB, 08193 Bellaterra, Spain

Received zzz, revised zzz, accepted zzz
Published online zzz

PACS 78.30.Am, 74.62.Fj, 07.35.+k, 78.67.Hc

* Corresponding author: e-mail sebareparaz@hotmail.com
** ICREA Research Professor

We have studied the correlation between the morphology of Si-capped Ge islands grown on Si substrates and their vibrational properties as measured by Raman scattering at ambient and under high hydrostatic pressure. For this study we have grown by molecular beam epitaxy a sample that exhibits a size distribution with two distinct island types having different aspect ratios called pyramids and domes. In accordance, Raman spectra show a double-peak structure at the frequencies of the Ge-Ge vibrational mode (~300 cm^{-1}) as well as for the Si-Ge mode (around 400 cm^{-1}). Pairwise, different selection rules have been found for these modes depending upon the Raman polarization configurations, suggesting a correlation between both Ge dot sizes and the double peak structure in the Raman spectra. Finally, a different strain status of the dots was observed by studying the pressure coefficient of the Ge-Ge phonon mode, resulting in a value of 3.3 cm^{-1} and 3.6 cm^{-1}/GPa for pyramids and domes, respectively. The main conclusion of our work is that the double-peak structure observed in Raman spectra is indicative of a bimodal dot size distribution in contrast with what is proposed in previous work within the so-called *core-shell model* [M.Y. Valakh *et. al,* Nanotechnol. **16**, 1464 (2005)].

1 Introduction Quantum dot (QD) systems have been widely studied during the last decade due to their potential applications in the optoelectronic industry[1,2]. In particular, Ge/Si dots have attracted much attention due to their possible integration with the Si based technology. Different dot morphologies such as pyramids, domes, and super-domes were systematically grown and studied due to their distinct physical properties[3-5]. High pressure measurements as well as Raman scattering have proved to be powerful tools in strain and compositional characterization of these systems, as is shown in recent work[6-8]. Nevertheless, in several cases a confusing situation is found in literature concerning the assignment of certain quantum dot vibrational modes such as the Ge-Ge and Si-Ge optical phonons. A double-peak structure at the frequencies of the Ge-Ge as well as the Si-Ge vibrations was in some cases observed[7,9], leading to the so called *core-shell model* as a possible interpretation[9]. Within this model a single dot is divided in two regions, a core surrounded by a shell, each of which is considered responsible for one peak of the observed double-peak structure. This model is in clear contrast with the results presented by Bernardi *et. al.*[7], where the doublet is suggested to originate form dots of different morphology.

In this work we intend to clarify this situation by showing that, in fact, the doublets originate from dots with different aspect ratio and strain status. By combining polarized Raman scattering with high pressure measurements we have investigated a specially designed sample which contains a bimodal distribution of dots (domes and pyramids). We have found that the doublets of both, the Ge-Ge and Si-Ge vibrational modes, exhibit *pairwise* different Raman polarization selection rules. Moreover, each peak of the Ge-Ge doublet displays a slightly different dependence on hydrostatic pressure. Results from a previous high pressure study[6] tell us that this is indicative of a different strain status for pair. Our findings led us to the conclusion that each pair Ge-Ge and Si-Ge Raman peaks arises from different QDs, in contrast with the proposed *core-shell model* in which the doublets

are explained as arising from dots with a single morphology (pyramids).

2 Experiments Samples were grown by molecular beam epitaxy on Si(001) substrates according to the following sequence: After oxide desorption at 900 ºC and 100 nm-thick Si buffer layer deposition, the substrate temperature was set to 500 ºC. In the next step, 12 ML of Ge were grown leading to dot formation in the standard Stranski-Krastanow (SK) growth mode. Finally, part of the sample was capped with a 10 nm-thick Si layer in order to avoid oxidation of the dots. The cap layer was deposited at low temperature (300 ºC) in order not to significantly alter the shape and composition of the dots. Growth was monitored in situ by reflection high energy electron diffraction (RHEED). The uncapped region was used to study the sample topography using atomic force microscopy (AFM), as shown in Fig. 1, where the grey scale stands for facet inclination (steeper facets correspond to darker colour). Dots with different aspect ratio, named as pyramids (P) and domes (D) in the figure, were found to be of approximately 10 and 20 nm in height with aspect ratios of 0.1 and 0.2, respectively.

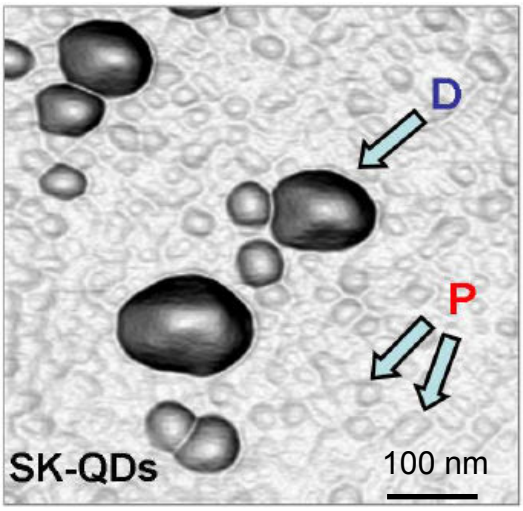

Figure 1 Topographic images of uncapped Ge/Si QDs. The grey scale indicates surface inclination (darker colour islands have steeper facets and higher aspect ratio). Labels refer to pyramids (P) and domes (D).

Raman spectra were collected with a LabRam HR800 system equipped with confocal microscope in backscattering geometry at room temperature using the 514.5 nm line of an Ar-ion laser. Light was focused onto the sample with a spot size of about 1 μm and a laser power of 4 mW. Polarized measurements were performed in -z(x,y)z and -z(x',y')z, where x,y,z are the [100], [010] and [001] crystallographic directions, and x',y' are axes rotated by 45º with respect to x,y ones. Measurements under pressure were carried out using the diamond anvil cell (DAC) technique. A 4:1 mixture of methanol and ethanol was employed as the pressure-transmitting medium. Pressure was monitored in situ by the shift of the Si longitudinal optical phonon, which was previously calibrated using the pressure shift of the ruby R1 line[10]. Samples loaded into the DAC were previously thinned to about 30 μm by mechanical polishing.

3 Results and Discussion Figure 2 shows the Raman spectra of the capped sample for two different polarization configurations. The -z(x,y)z configuration (upper spectrum) exhibits four peaks distributed in two spectral regions around 300 cm^{-1} and 400 cm^{-1}. The Raman peaks of the first and second region are attributed to Ge-Ge and Si-Ge vibrational modes of the quantum dots, respectively[11]. The observation of Si-Ge phonons is a consequence of a process of interdiffusion during growth. The overwhelming signal of the Si substrate is not shown in Fig. 2 for the sake of clarity in the discussion of the QD features. Since for all the cases we have used crossed polarization configurations, the signal from the second order Raman scattering by acoustic phonons of Si substrate is widely suppressed in the spectra. The line-shape analysis of the spectra was performed using four Gaussians. The dashed lines in Fig. 2 are an example of the deconvolution of the 300 cm^{-1} feature into two contributions. A preliminary assignment of the four peaks pairwise to domes and pyramids, as indicated in Fig. 2, is possible by considering the peak positions. A comparative study of the properties of conventional and carbon-induced self-assembled Ge QDs before and after capping[7] shows that domes are better able to relax strain elastically and exhibit less Si interdiffusion after capping than pyramids. Hence, the corresponding Raman features are expected to be blueshifted for pyramids with respect to domes.

For cubic materials the Raman selection rules state that in backscattering from the (001) crystal surface the longitudinal-optical zone-centre phonon is allowed in the -z(x,y)z but forbidden in the -z(x',y')z polarization configuration, as can be found elsewhere[12]. As illustrated in Fig. 2, when the -z(x',y')z polarization configuration is applied the peaks at 310 cm^{-1} and 420 cm^{-1} vanish with an extinction ratio of about 1:100. in contrast, the peaks at 300 cm^{-1} and 390 cm^{-1} decrease in signal only by a 1:5 ratio.

The behaviour of these double-peak structures with polarization provides a clue to understand their origin. Elastic strain relaxation by formation of domes is much more efficient than for pyramids. As a result, the parent cubic lattice is much more distorted within a dome. Besides, only pyramids are easily recompressed by the cap layer, remaining pseudomorphic to the substrate[13]. It is then expected that pyramids follow better the polarization selection rules than domes, since the cubic/tetragonal symmetry is locally distorted by strain within the domes, leading to the observed relaxation of the Raman selection rules. It follows that the pair of peaks at 300/390 cm^{-1} most

likely arises from the domes, whereas the pair at 310/420 cm^{-1} originates from the pyramids.

We rule out that this depolarization effect arises from refraction of the incident light entering the sample, which is slightly deviated from normal incidence due to the fact that the surface of the sample is not flat, particularly above the larger islands, i.e., domes. For this purpose we have grown a sample with similar domes but a much thicker cap layer of approximately 300 nm. In this case the sample surface is completely flat, thus, no deviation of the incident beam can occur. However, we obtained a similar depolarization in this case too, implying that the observed effect is intrinsic to the domes.

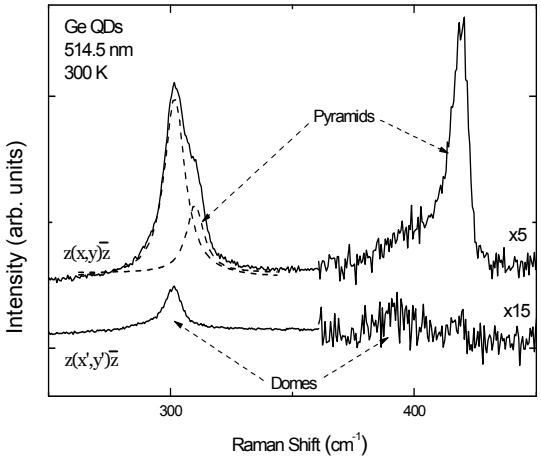

Figure 2 Raman Spectra of the QDs sample using two different polarization configurations: -z(x,y)z (upper), and -z(x',y')z (lower). The spectra in the region of the Si-Ge mode are multiplied by the given factors. Dashed lines represent the deconvolution of the spectral line shape using Gaussians.

As previously shown[14], the QD strain status can a be also studied by applying hydrostatic pressure and measuring the pressure coefficient of the Ge-Ge mode arising from both types of dots. In Fig. 3 we show three representative spectra for different pressures. As clearly observed, with increasing pressure the separation between both Ge-Ge peaks (domes and pyramids) decreases. In order to obtain the pressure coefficient of each dot ensemble type, we have restricted ourselves to the range between 0 and 2 GPa where the pressure dependence of the phonon frequency is essentially linear. In the inset to Fig. 3 we display the obtained results to determine the pressure coefficients. The points represent the position of the maximum of the Ge-Ge peak for the domes and pyramids and the straight line is a linear fit to the experimental data. Unfortunately, it was not possible to obtain the pressure coefficients of the Si-Ge modes because inside the DAC the signal was too low to distinguish these peaks (see Fig. 3). In addition, it should be pointed out that the pressure experiments were performed in strict backscattering configuration, so that the strong Raman signal from the diamond at 1332 cm^{-1} affects more the measurement of the Si-Ge than the Ge- Ge mode.

The obtained linear pressure coefficients of the Ge-Ge mode are 3.30(20) and 3.60(5) cm^{-1}/GPa for pyramids and domes, respectively. Numbers in parentheses represent error bars. Although these values are quite similar, the difference is beyond experimental uncertainty. As shown by Reparaz *et. al.*[14] the pressure coefficient of dots decreases in magnitude as the dot-to-cap-layer volume ratio decreases. Since the cap layer is the same for all dots in our sample, we expect that pyramids which are much smaller than domes have a lower pressure coefficient. Hence, the pressure results confirm the assignment of the Raman peaks already made based on the polarization behaviour.

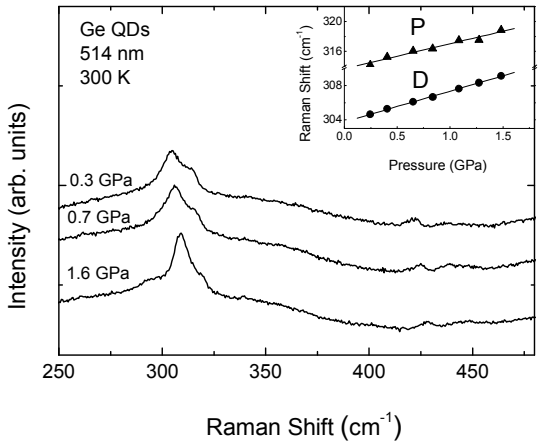

Figure 3 Pressure coefficient determination for the Ge-Ge mode for pyramids and domes. Inset: The points indicate the position of the measured peaks and the solid line is a linear fit of the data.

Our observations are not compatible with the interpretation of the double-peak structures as arising from the same QD ensemble but from different regions of the same dot, as proposed by Valakh *et. al.*[9], within the so called *core-shell* model. In this model it is considered that every QD consists of two distinct regions; a Ge-rich core and an outer intermixed shell, giving rise to two peaks in the Raman spectra. The lower-frequency Ge-Ge component is ascribed to the intermixed shell together with the most prominent Si-Ge peak at higher frequency. Our measurements demonstrate, however, that these peaks display different polarization behaviour, invalidating the assignment to the dot shell. Moreover, the same pressure coefficient is expected for core and shell region of the same dot because at high Ge contents the pressure coefficient is independent of composition[8].

3 Summary We have combined polarized Raman spectroscopy with high pressure measurements to establish the origin of the double-peak structures at the frequencies of the Ge-Ge and Si-Ge modes very often observed in self-assembled Ge/Si dot samples. We have shown that the lower frequency peaks and the higher frequency ones of the Ge-Ge and Si-Ge doublets are coupled to each other and that each of these pairs can be attributed to different dot types, domes and pyramids, indicating the existence of a bimodal size distribution. Our results are relevant for the interpretation of Raman spectra of quantum dot samples in general since they are valid for *any* material system besides Si/Ge.

Acknowledgements J.S.R. Acknowledges financial support from the AlBan fellowship Program. A.B. acknowledges an FPI fellowship. This work was supported in part by the Spanish Ministerio de Educación y Ciencia through grant MAT2006-02680. Measurements were performed at the Nanotechnology Laboratory of MATGAS 2000 A.I.E.

References

[1] J. Faist, F. Capasso, D. L. Sivco, C. Sirtori, A. L. Hutchinson and A. Y. Cho, *Science* **264**, 553 (1994).
[2] B. F. Levine, J. Appl. Phys. **74**, R1 (1993).
[3] Y.-W. Mo, D. E. Savage, B. S. Swartzentruber, and M. G. Lagally, Phys. Rev. Lett. **65,** 1020 (1990).
[4] G. Medeiros-Ribeiro, A. M. Bratkovski, T. I. Kamins, D. A. A. Ohlberg, and R. S. Williams, Science **279,** 353 (1998).
[5] M. Stoffel, A. Rastelli, J. Stangl, T. Merdzhanova, G. Bauer, and O.G. Schmidt, Phys. Rev. B **75,** 113307 (2007).
[6] J.S. Reparaz, A. Bernardi, A.R. Goñi, M.I. Alonso, and M.Garriga, Appl. Phys. Lett. **91,** 081914 (2007).
[7] A. Bernardi, M. I. Alonso, J. S. Reparaz, A. R. Goñi, P. D. Lacharmoise, J. O. Ossó, and M. Garriga, Nanotechnol. **18**, 475401 (2007).
[8] J. S. Reparaz, A. Bernardi, A. R. Goñi, M. I. Alonso, and M Garriga, Appl. Phys. Lett. **92**, 081909 (2008).
[9] M.Y. Valakh, V. Yukhymchuk, V.M. Dzhagan, O.S. Lytvyn, A.G. Milekhin, A.I. Nikiforov, O.P. Pchelyakov, F. Alsina, J. Pascual, Nanotechnol. **16**, 1464 (2005).
[10] H.K. Mao, J. Xu, and P.M. Bell, J. Geophy. Res. **91**, 4673 (1986).
[11] M. I. Alonso and K. Winer, Phys. Rev. B **39**, 10056 (1989).
[12] K. Mizoguchi and S. Nakashima, J. Appl. Phys. **65**, 2583 (1989).
[13] B. V. Kamenev, H. Grebel, L. Tsybeskov, T. I. Kamins, R. S. Williams, J. M. Baribeau, and D. J. Lockwood, Appl. Phys. Lett. **83**, 5035 (2003).
[14] J.S. Reparaz, A. Bernardi, A.R. Goñi, M.I. Alonso, and M.Garriga, Appl. Phys. Lett. **91,** 081914 (2007).

phys. stat. sol. (b) **244**, No. 1, 76–81 (2007) / **DOI** 10.1002/pssb.200672543

Raman scattering of capped and uncapped carbon-induced Ge dots under hydrostatic pressure

A. Bernardi[*], **J. S. Reparaz, A. R. Goñi**[**], **M. I. Alonso,** and **M. Garriga**

Institut de Ciència de Materials de Barcelona-CSIC, Esfera UAB, 08193 Bellaterra, Spain

Received 25 July 2006, accepted 8 August 2006
Published online 8 December 2006

PACS 62.50.+p, 63.22.+m, 78.30.Am, 78.67.Bf, 81.07.Ta

We compare results from Raman scattering for both capped and uncapped Ge quantum dots under hydrostatic pressure. The behavior of lattice vibrations and electronic transitions of the quantum dots are affected by the presence or absence of a cap layer. The pressure coefficient obtained for the Ge mode of relaxed, uncapped islands is close to the corresponding value in bulk, whereas it is reduced by ~20% in presence of a Si cap layer. This result can be understood by taking into account the change of the boundary condition imposed to the Ge lattice, which is constrained to match that of the silicon matrix. Measurements of the capped sample exhibit a resonant enhancement which is not appreciable for the uncapped dots. We relate this effect to the different lifetime of electronic states.

1 Introduction

Self-assembled Ge quantum dots (QDs) on Si(001) might, in the future, be considered as a candidate for optoelectronic applications by controlling the built-in strain which, in turn, allows to tailor the optical properties of nanostructures [1]. Raman scattering represents a powerful diagnostic tool to gather information on composition and strain in thin films and quantum dots. Moreover, due to the different compressibility of Si and Ge, experiments under hydrostatic pressure [2, 3] can also be used to tune the strain induced by the silicon matrix on the embedded Ge dots and, as a result, a shift of their interband electronic transitions can be obtained [4, 5]. Previous works on Ge dots under pressure focused on samples capped with thick layers (~200 nm) and reported pressure coefficients ($d\omega/dP$) for the optical Ge mode systematically lower than the value measured for the bulk material (3.9 cm^{-1}/GPa) [6–8]. Such discrepancy is discussed accounting for the different elastic properties of Ge and the surrounding silicon host matrix [9].

In this work, we investigated the case of uncapped quantum dots and we demonstrate that if the compression acting at the substrate/island interface (at the dot basis) is not affecting substantially the whole volume of the island, then the measured pressure coefficient tends to the value of bulk Ge. On the contrary, a really thin (10 nm) Si cap-layer is enough to achieve an important reduction (by ~20%) of the pressure coefficient, in analogy with data of the literature obtained for much thicker cap layers. Moreover, the presence of a thin cap layer enables the resonant enhancement of Raman scattering intensity to be observed, when an interband electronic transition of the Ge QDs is brought into resonance with the laser line by applying pressure. This effect is otherwise not detectable in uncapped samples due to a reduced lifetime of electronic states.

[*] Corresponding author: e-mail: abernardi@icmab.es, Fax: +34 93 580 57 29
[**] ICREA Research Professor

2 Experimental details

Samples were grown by solid-source molecular beam epitaxy according to the following procedure: after oxide desorption at 900 °C and 50 nm-thick Si buffer layer deposition, a ~4 Å thick Ge wetting layer was grown before depositing 0.1 monolayers (MLs) of carbon. This surface modification allows for the control of shape and density ($\sim 3 \times 10^9$ cm^{-2}) of islands in the next growth step, when ~6 Å of Ge are deposited at 500 °C. The resulting topography consists of dome-shaped dots 10–15 nm high [10]. For the capped sample, a 10 nm thick Si layer was subsequently grown at low temperature (300 °C) in order to avoid silicon intermixing and to preserve the island shape.

The Raman spectra were collected with a LabRam HR800 system in backscattering geometry at room temperature using different lines from an argon-ion laser. Measurements under pressure were carried out using the diamond anvil cell (DAC) technique. A 4:1 mixture of methanol and ethanol was employed as the pressure-transmitting medium. Pressure was monitored *in situ* by the shift of the ruby R1 line [12]. The samples loaded in the DAC were previously thinned to about 30 microns by mechanical polishing.

3 Results and discussion

3.1 Vibrational modes

Figure 1 shows Raman spectra measured at various pressures up to ~7 GPa in the capped sample. The Raman signal close to ~300 cm^{-1} is ascribed to the Ge–Ge phonon mode of the Ge dots. We note that these spectra were measured in crossed polarization $z(x, y)\,\bar{z}$, where x, y, and z are the [100], [010], and [001] crystallographic directions of the Si substrate, in order to suppress the second-order Raman signal of the transverse acoustical phonons of the Si substrate, which would interfere with the Ge dot mode. The very strong signal at ~520 cm^{-1} is attributed to the optical phonon of the Si substrate. Both modes shift to higher frequencies with increasing pressure and their intensities change due to resonance effects. The intensity decrease of the substrate mode is related to the shift of the E_1 electronic transition of Si to higher energies with increasing pressure.

The overall intensity of the spectra in the uncapped sample is much lower than for the capped one and no polarization analysis was made. However, the Ge–Ge mode and second order Si-2TA signal that almost overlap each other at $P = 0$ can be resolved under pressure, since they shift in opposite directions [7]. The frequency shift of the strong Si substrate signal at ~520 cm^{-1} can be used as internal wavenumber calibration of the spectra. The Raman shifts measured as a function of pressure are plotted in Fig. 2. A linear fit to the data gives the pressure coefficient $\mathrm{d}\omega/\mathrm{d}P = (3.9 \pm 0.1)$ cm^{-1}/GPa and the phonon frequency at

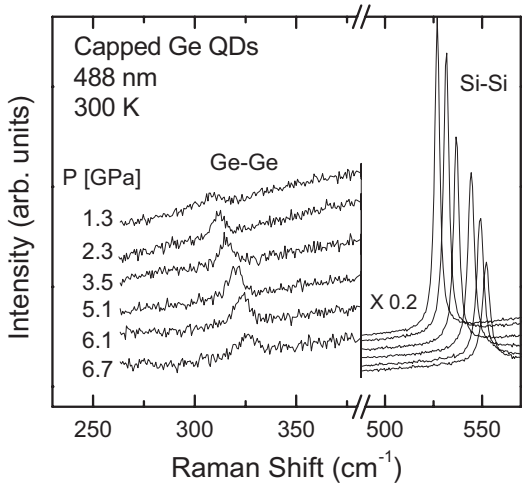

Fig. 1 Raman spectra of the capped QDs measured at different pressures. The peak at ~300 cm^{-1} (ambient pressure value) corresponds to the Ge–Ge phonon, whereas the very strong signal at ~520 cm^{-1} comes from the Si substrate.

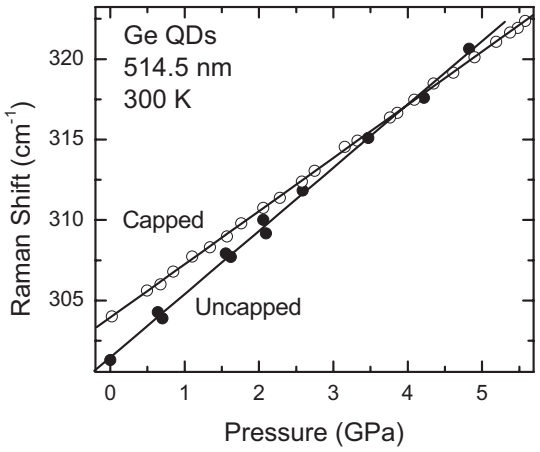

Fig. 2 Position of the Raman peaks observed in the two samples as a function of pressure. Open (closed) circles are results of the capped (uncapped) sample. Solid lines correspond to least-squares fits to the experimental data using a linear function.

zero pressure $\omega_0 = 301.5 \pm 0.2\ \mathrm{cm}^{-1}$ for the uncapped sample, and $\mathrm{d}\omega/\mathrm{d}P = 3.30 \pm 0.02\ \mathrm{cm}^{-1}/\mathrm{GPa}$ and $\omega_0 = 303.94 \pm 0.04\ \mathrm{cm}^{-1}$ for the capped sample. The values of ω_0 are different due to an increase in built-in strain for the capped QDs with respect to the relaxed, uncapped ones.

The pressure coefficient obtained for the uncapped sample is in very good agreement with the expected Ge bulk value. However, for the sample capped with 10 nm of Si we obtain instead a lower coefficient which is closer to the values reported for dots overgrown with much thicker Si cap-layers [7] or in superlattices [8].

The carbon-induced Ge dots under investigation are Ge rich (>90%) dome-shaped islands [10, 11], whose enhanced aspect-ratio leads to an efficient relaxation of the strain originating at the island/substrate interface due to the lattice mismatch between Ge and Si (~4%). Raman scattering spectroscopy gives information on the average Ge content and mean strain of the islands. In particular, the Ge–Ge mode is likely to steam mainly from the Ge-rich core of the islands, where holes are better confined. We thus expect that only a small contribution corresponds to the volume of material close and elastically coupled to the silicon substrate, for example, the wetting layer.

The different pressure coefficients obtained for samples with and without cap layer can be explained if we consider the boundary conditions applicable for each case. In general, the strain induced on the dot by applying external pressure can be decomposed in two terms:

$$\varepsilon(P) = \varepsilon^{\mathrm{hydro}}(P) + \varepsilon^{\mathrm{matrix}}(P)\,, \tag{1}$$

where the first term is the pure hydrostatic part of the Ge dot described by the Murnaghan equation of state (B_0^{Ge} is the bulk modulus of Ge)

$$\varepsilon^{\mathrm{hydro}}(P) = \frac{a^{\mathrm{Ge}}(P) - a_0^{\mathrm{Ge}}}{a_0^{\mathrm{Ge}}} = 1 + \left(\frac{B_0'}{B_0^{\mathrm{Ge}}}\,P + 1\right)^{-\frac{1}{3B_0'}} \cong -\frac{P}{3B_0^{\mathrm{Ge}}} + \ldots \tag{2}$$

When the dot is constrained into a host material the additional term accounts for the strain originating from the different compressibility of the dot and matrix material. It depends on the boundary condition which we express in terms of a parameter $0 < \varphi < 1$ to describe the degree of relaxation of the dot according to

$$\begin{aligned}\varepsilon^{\mathrm{matrix}}(P) &= \frac{a^{\mathrm{QD}}(P) - a^{\mathrm{Ge}}(P)}{a_0^{\mathrm{Ge}}} \\ &= \frac{[a^{\mathrm{Si}}(P) + \varphi(a^{\mathrm{Ge}}(P) - a^{\mathrm{Si}}(P))] - a^{\mathrm{Ge}}(P)}{a_0^{\mathrm{Ge}}} \qquad \begin{cases}\varphi = 0, & a^{\mathrm{QD}} = a^{\mathrm{Si}} \\ \varphi = 1, & a^{\mathrm{QD}} = a^{\mathrm{Ge}}\,.\end{cases}\end{aligned} \tag{3}$$

Combining Eqs. (1)–(3) we can obtain a general expression for the expected Raman frequency shift under pressure, with a constant term representing the shift due to the built-in strain (at applied pressure $P = 0$) and a linear term on P, whose slope is the pressure coefficient of the phonon mode (here $\tilde{K}_{ij}$ are the phonon deformation potentials for Ge):

$$\Delta\omega = \frac{\omega_0}{2}\left(\tilde{K}_{11} + 2\tilde{K}_{12}\right)\varepsilon(P) \approx \frac{\omega_0}{2}\left(\tilde{K}_{11} + 2\tilde{K}_{12}\right)\left[(1-\varphi)\,\frac{a_0^{\mathrm{Si}} - a_0^{\mathrm{Ge}}}{a_0^{\mathrm{Ge}}}\right] - \frac{\omega_0}{6}\left(\tilde{K}_{11} + 2\tilde{K}_{12}\right)\left[\frac{1}{B_0^{\mathrm{Si}}} + \varphi\left(\frac{1}{B_0^{\mathrm{Ge}}} - \frac{1}{B_0^{\mathrm{Si}}}\right)\right]P\,. \tag{4}$$

If we consider the sample with uncapped QDs and we assume that due to strain relaxation the average lattice parameter in the dot is $a^{\mathrm{QD}} \approx a^{\mathrm{Ge}}$ (corresponding to the case $\varphi \approx 1$), then there is no built-in strain and the pressure coefficient is given by the pure hydrostatic term, dependent on the bulk modulus of Ge. When a cap layer is present, the dot is compressed to adjust its lattice parameter to that of the host material, i.e. $a^{\mathrm{QD}} \approx a^{\mathrm{Si}}$ (if the dot is fully compressed then $\varphi \approx 0$). In this second case, as deduced from Eq. (4), only the bulk value of silicon enters in the calculation of the pressure coefficient and a constant frequency shift is arising from the built-in strain. From Eq. (4) follows that $(\mathrm{d}\omega/\mathrm{d}P)^{\mathrm{capped}}/(\mathrm{d}\omega/\mathrm{d}P)^{\mathrm{uncapped}} = B_0^{\mathrm{Ge}}/B_0^{\mathrm{Si}} = 0.77$, in good agreement with the experimental value (0.84).

3.2 Electronic states

The influence of pressure on the E_1 and $E_1 + \Delta_1$ electronic transitions of the QDs can be studied by resonant Raman measurements [13, 14]. When the energy of the exciting laser is close to that of the optical transitions, the resonance curve can be tuned by pressure. In our experiments we were able to measure a resonant enhancement of the Ge–Ge Raman phonon only on the sample with cap layer. The Raman intensity on the uncapped sample was rather low and remained constant within noise. This fact seems contradictory because these electronic transitions were measured by ellipsometry on the uncapped sample at $E_1 = 2.23$ eV and $E_1 + \Delta_1 = 2.43$ eV and are in the suitable spectral range. According to these energies, the QDs have an average composition $x = 0.92$ [10]. The Ge transition energies on the capped sample cannot be fitted clearly due to absorption by the Si cap, nevertheless, the QD composition should not be altered by the low T capping process. In order to understand the different resonance behavior with/without cap layer, we have modeled the shape and relative intensity of the two resonance curves by considering the expression of the Raman polarizability near the two-dimensional critical points E_1 and $E_1 + \Delta_1$ [15]:

$$|a|^2 \propto \left|\frac{d_{1,0}^5}{4\sqrt{2}}\,\frac{d(\chi^{E_1} + \chi^{E_1+\Delta_1})}{\mathrm{d}E_1} - d_{3,0}^5\left(\frac{\chi^{E_1} - \chi^{E_1+\Delta_1}}{\Delta_1}\right)\right|^2,$$
$$\chi^{E_j} = A_j\,\mathrm{e}^{i\phi_j}\,\frac{E_j^2}{E^2}\ln\left[1 - \left(\frac{E}{E_j - i\Gamma_j}\right)^2\right], \tag{5}$$

where χ^{E_j} is the electronic susceptibility and the critical-point parameters are the amplitude A_j, the width Γ_j and the phase ϕ_j. The latter are obtained from analysis of ellipsometric spectra. The pressure-tuned resonance curve is obtained at fixed laser energy $E = E_{\mathrm{L}} = 2.541$ eV. To introduce the dependence on pressure we take into account that both gaps shift with the same pressure coefficient α, that is, $E_j(P) = E_j(0) + \alpha P$. In this way, the pressure coefficient α can be evaluated from measurements using only one laser line.

The results for the resonant enhancement of the Ge-mode intensity for the capped sample are plotted in Fig. 3. Raman intensities are normalized relative to the maximum intensity at resonance and are given in arbitrary units. We fit the shape of the curve as a function of pressure having α as fit parameter. The

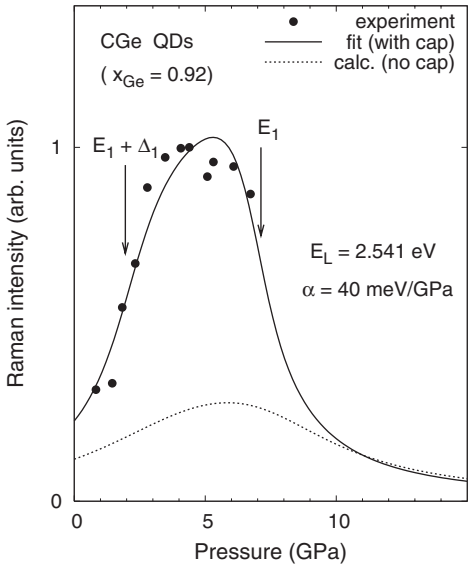

Fig. 3 Resonant Raman intensities of the Ge–Ge mode as a function of pressure for the capped dot sample (symbols). The solid (dotted) line is the calculated resonance curve for the capped (uncapped) dots, as explained in the text. Arrows indicate the pressure values for which the laser of energy E_L coincides with the corresponding optical transition.

actual transition energies are calculated from the known composition $x = 0.92$ and with a best-fit built-in biaxial strain $\varepsilon_{\parallel} = -0.6\%$. The rest of the needed quantities are taken from literature values for Ge [15]. In particular, the broadening of the gaps are taken as those of bulk Ge. For the uncapped sample, the broadening obtained from ellipsometry is about a factor of two larger. If we just calculate the resonance curve expected for the uncapped sample with larger broadening, the overall Raman intensity drops considerably, as shown in Fig. 3 by the dotted curve.

The value of $\alpha = 40 \pm 5$ meV/GPa obtained from the fit is similar to previous measurements in capped samples, reduced with respect to bulk Ge in the same way as the phonon pressure coefficient. It is likely that α in the uncapped sample should be closer to the bulk value but, unfortunately, it was not possible to be evaluated.

4 Conclusions

In this work we compared Raman scattering from Ge QDs under hydrostatic pressure when the dots are uncapped versus the situation where they are covered with a Si cap layer. We demonstrated that if the dots are not embedded in the Si matrix, then the measured pressure coefficient tends to the value of bulk Ge. On the contrary, just a very thin 10 nm Si cap layer is sufficient to reduce the coefficient by ~20% to values similar as previously obtained in literature for much thicker cap layers.

We considered the different boundary conditions to explain these two experimental situations, namely we dealt with the limiting cases of fully relaxed uncapped dots (highest $\mathrm{d}\omega/\mathrm{d}P$) and fully compressed capped dots (lowest $\mathrm{d}\omega/\mathrm{d}P$). Nevertheless, Eq. (4) also holds for a much more complex and generalized scenario, where an intermediate situation can be accounted for. Depending on the shape (aspect ratio) and on the size of the dots the degree of relaxation (φ) is expected to vary considerably and the DAC technique for the determination of pressure coefficients turns out to be a powerful diagnostic tool for studying the mechanisms of relaxation in self-assembled nanostructures.

Moreover, we observed that in uncapped dots no significant resonant enhancement of Raman scattering intensity can be observed, an effect clearly seen in presence of a thin cap layer. The increased lifetime (smaller broadening) of electronic states in capped samples is considered as a plausible explanation for this observation.

Acknowledgments We thank the spanish Ministerio de Educación y Ciencia for support through MAT2003-00738 and an FPI fellowship (A.B.). J.S.R. acknowledges an Alßan fellowship.

References

[1] J. Stangl, V. Holy, and G. Bauer, Rev. Mod. Phys. **76**, 725 (2004).
[2] Z. Sui, H. H. Burke, and I. P. Herman, Phys. Rev. B **48**, 2162 (1993).
[3] Z. Sui, I. P. Herman, and J. Bevk, Appl. Phys. Lett. **58**, 2351 (1991).
[4] Z. X. Liu, O. G. Schmidt, U. D. Venkateswaran, K. Eberl, and K. Syassen, Semicond. Sci. Technol. **15**, 155 (2000).
[5] K. L. Teo, S. H. Kwok, P. Y. Yu, and S. Guha, Phys. Rev. B **62**, 1584 (2000).
[6] M. Seon, M. Holtz, T.-R. Park, O. Brafman, and J. C. Bean, Phys. Rev. B **58**, 4779 (1998).
[7] K. L. Teo, L. Qin, Z. X. Shen, and O. G. Schmidt, Appl. Phys. Lett. **80**, 2919 (2002).
[8] L. Qin, K. L. Teo, Z. X. Shen, C. S. Peng, and J. M. Zhou, Phys. Rev. B **64**, 075312 (2001).
[9] L. Liu, K. L. Teo, Z. X. Shen, J. S. Sun, E. H. Ong, A. V. Kolobov, and Y. Maeda, Phys. Rev. B **69**, 125333 (2004).
[10] A. Bernardi, J. O. Ossó, M. I. Alonso, A. R. Goñi, and M. Garriga, Nanotechnology **17**, 2602 (2006).
[11] A. Bernardi, M. I. Alonso, A. R. Goñi, J. O. Ossó, and M. Garriga, Appl. Phys. Lett. **89**, 101921 (2006).
[12] H. K. Mao, J. Xu, and P. M. Bell, J. Geophy. Res. **91**, 4673 (1986).
[13] D. Bougeard, P. H. Tan, M. Sabathil, P. Vogl, G. Abstreiter, and K. Brunner, Physica E **21**, 312 (2004).
[14] A. B. Talochkin, S. A. Teys, and S. P. Suprun, Phys. Rev. B **72**, 115416 (2005).
[15] M. I. Alonso and M. Cardona, Phys. Rev. B **37**, 10107 (1988).

3.2.3 Conclusions

A new method to determine the strain status of quantum dot systems was presented. An important advantage of this method is that it is independent of the studied material system. In particular, it was used to study the strain status of Ge/Si dots as a function of the Si cap layer thickness. It was found that the Ge dots undergo a biaxial to hydrostatic strain status transition when increasing the Si cap layer thickness (critical thickness $\sim$ 10 nm). This is an important result since it provides a guide for an appropriate choice of the strain tensor in each particular situation.

This technique was also applied to a system with a bimodal distribution of Ge/Si dots. A different strain status was found for each dot distribution reflected in a different pressure coefficient. This provides an alternative explanation for the doulbe-peak structure often observed in Raman spectra of semiconductor QDs in clear contrast with the so-called *core-shell model*[12].

The presented method has proved to be appropriate to study the strain status of certain low dimensional structures. The optical phonon pressure coefficient determination, thus, provides a direct measurement of the strain status of these structures that would be rather complicated to perform using other techniques.

Bibliography

[1] S. Christiansen, M. Albrecht, H. P. Strunk, and H. J. Maier, Appl. Phys. Lett **64**, 3617 (1994).

[2] F. Liu S. E. Davenport, H. M. Evans, and M. G. Lagally, Phys. Rev. Lett. **82**, 2528 (1999), and references therein.

[3] V. Le Thanh, V. Yam, P. Boucaud, F. Fortuna, C. Ulysse, D. Bouchier, L. Vervoort, and J.-M. Lourtioz, Phys. Rev. B **60**, 5851 (1999).

[4] A. A. Darhuber, P. Schittenhelm, V. Hol, J. Stangl, G. Bauer, and G. Abstreiter, Phys. Rev. B **55**, 15652 (1997).

[5] O. G. Schmidt and K. Eberl, Phys. Rev. B **61**, 13 721 (2000)

[6] O. G. Schmidt, K. Eberl, and Y. Rau, Phys. Rev. B **62**, 16 715 (2000).

[7] M. A. Makeev, and A. Madhukar, Phys. Rev. Lett. **86**, 5542 (2001).

[8] C. Pryor, J. Kim, L. W. Wang, A. J. Williamson, and A. Zunger, J. Appl. Phys. **83**, 2548 (1998).

[9] K. L. Teo, L. Qin, I. M. Noordin, G. Karunasiri, Z. X. Shen, O. G. Schmidt, K. Eberl, and H. J. Queisser, Phys. Rev. B **63**, 121306(R) (2001).

[10] A. Bernardi, J. S. Reparaz, A. R. Goñi, M. I. Alonso, and M. Garriga, phys. stat. sol. (b) **244**, 76 (2007).

[11] J. S. Reparaz, A. Bernardi, A. R. Goñi, M. I. Alonso, and M. Garriga, Appl. Phys. Lett. **92**, 081909 (2008).

[12] M. Y. Valakh, V. Yukhymchuk, V. M. Dzhagan, O. S. Lytvyn, A. G. Milekhin, A. I. Nikiforov, O. P. Pchelyakov, F. Alsina, J. Pascual, Nanotechnol. **16**, 1464 (2005).

3.3 Strain Effect in CdSe Quantum Dots

Compound semiconductors of the II-VI family have been widely studied due to their potential applications in the optoelectronic industry. The advantage of these materials, in contrast to the III-V compounds, is their higher exciton binding energy and the wider energy band gap that they offer. In particular, self-assembled QDs are good candidates since they also provide spatial confinement of the excitons within the QDs. A great amount of work can be found in the literature for this system, like CdSe/ZnMnSe, CdSe/ZnBeSe, ZnCdSe/ZnSe, CdTe/ZnTe, and ZnSe/ZnS (see Refs. [1]-[9]). However, the control and reproducibility in the size of the QDs continue to be a drawback regarding future device applications. In this section, a recently developed system will be presented, whose mayor advantage is an improvement in the control and reproducibility of the QD size distribution. It will be further shown that by combining Raman spectroscopy with high pressure measurements its possible to obtain information about the strain status of this system too.

3.3.1 Motivation and Previous Work

In this section a brief introduction to a recently developed II-VI QDs system will be provided. Raman spectroscopy and high pressure measurements were used as characterization techniques. It is not the author's purpose to make a review of this field but instead to give a short description of the previously investigated physical properties of the studied samples. As was already mentioned, a major drawback of II-VI systems is the low degree of control and reproducibility of the QD size as compared to other systems like III-V compounds. In a recent publication [1] *Perez-Paz et. al.* presented a system with a high degree of reproducibility concerning its growth mechanism. The studied samples were CdSe QDs with $Zn_{0.38}Cd_{0.23}Mg_{0.39}Se$ barriers grown by molecular beam epitaxy. Fig. 3.8 shows the structure of the samples as well as a typical AFM image extracted from Ref. [1]. The QD height ranges between 3 and 7 monolayers (ML) of CdSe and the barrier is the same for all the cases.

Fig. 3.9 shows the PL spectra for five samples with different CdSe deposition times: 6 s (1.2 ML), 13 s (2.5 ML) , 18 s (3.6 ML), 24 s (4.8 ML), and 29 s (5.8 ML). The ZnCdMgSe barrier layers were grown with the same composition, thickness, and band gap of about 2.8 eV for all the samples. The nearly linear relation between the PL peak energy and the deposition time (t_D) is also shown in Fig. 3.9. Several sets of samples grown on different days indicate that a good control and reproducibility were achieved (different

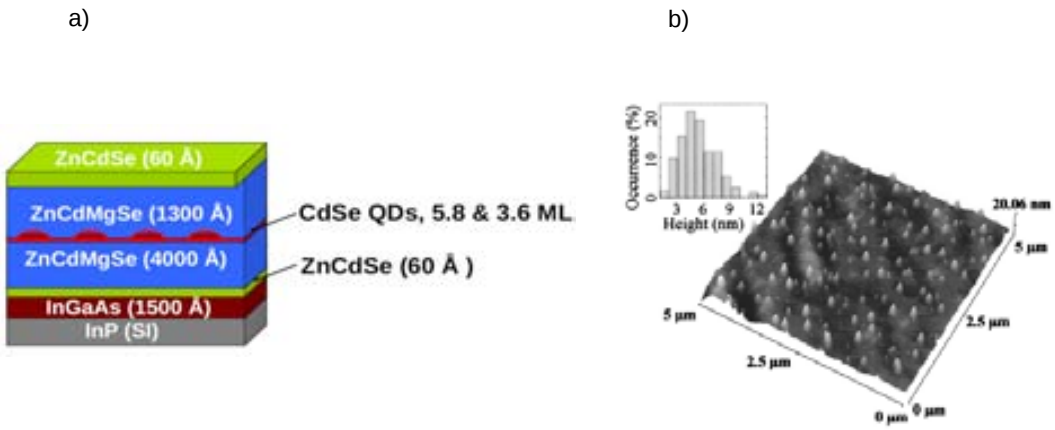

Figure 3.8: a) Sketch of the structure of the studied samples. b) Typical AFM image of CdSe dots with ZnCdMgSe barriers. The inset shows an histogram of the QD height. Extracted from Ref. [1].

points in Fig. 3.9, *left*).

As we have seen from the work of *Perez-Paz et. al.* this system allows for a tunning of the optical emission in almost all the visible range. In order to study the influence of the built-in strain on the optical properties the two following points were studied:

- Is built-in strain important concerning the tuning of the emission of the QDs? If this is the case, what is the contribution of this effect?
- How does the strain status of the dots depend on the dot size?

The influence of the built-in strain on the optical emission resulted in the publication presented in the next section: *"Size-dependent strain effects in self-assembled CdSe quantum dots with* $Zn_{0.38}Cd_{0.23}Mg_{0.39}Se$ *barriers"* (Article Number: 5). In this article the built-in strain of the QDs was determined and, thus, its influence on their optical properties. Interdiffusion of Mg from

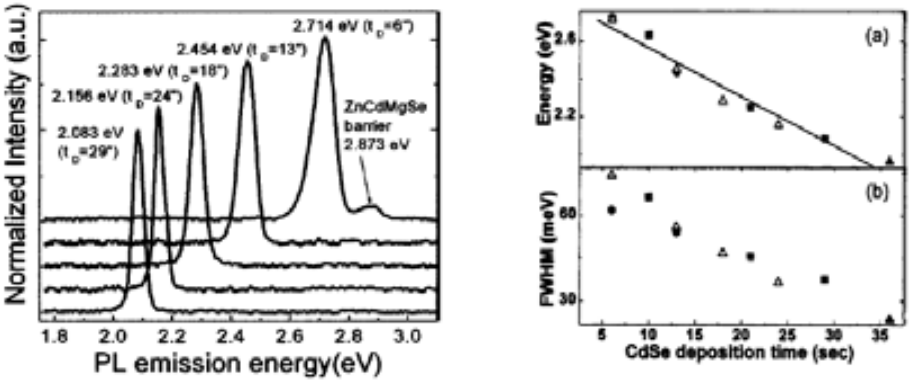

Figure 3.9: *Left:* PL spectra of five samples grown with different deposition time (t_D). The PL peak emission energy and t_D for each sample is indicated in parentheses. *Right:* (a) Variation of the PL emission energy and (b) of FWHM with t_D for several samples grown on different days. The different symbols indicate the different days the samples were grown. Extracted from Ref. [1].

the barrier into the QDs was detected and quantified. The second point was studied in a second article presented in the next section: *"Photoluminescence of CdSe quantum dots with $Zn_{0.38}Cd_{0.23}Mg_{0.39}Se$ barriers under hydrostatic pressure"* (Article Number: 6), where the pressure coefficient of the fundamental emission of dots with different height was studied.

3.3.2 Experiments and Results

Article n: 5

Title: Size-dependent strain effects in self-assembled CdSe quantum dots with $Zn_{0.38}Cd_{0.23}Mg_{0.39}Se$ barriers.

Authors: J. S. Reparaz, A. R. Goñi, M. I. Alonso, M. N. Perez-Paz, and M. C. Tamargo.

Journal: Applied Physics Letters

Article n: 6

Title: Photoluminescence of CdSe quantum dots with $Zn_{0.38}Cd_{0.23}Mg_{0.39}Se$ barriers under hydrostatic pressure.

Authors: J. S. Reparaz, A. R. Goñi, M. I. Alonso, M. N. Perez-Paz, and M. C. Tamargo.

Journal: Physica Status Solidi b

Size-dependent strain effects in self-assembled CdSe quantum dots with $Zn_{0.38}Cd_{0.23}Mg_{0.39}Se$ barriers

J. S. Reparaz,[a] A. R. Goñi, and M. I. Alonso
Institut de Ciència de Materials de Barcelona-CSIC, Esfera UAB, 08193 Bellaterra, Spain

M. N. Perez-Paz and M. C. Tamargo
Department of Chemistry, City College of The City University of New York, New York, New York 10031

(Received 14 August 2006; accepted 25 October 2006; published online 6 December 2006)

From resonant Raman scattering measurements under hydrostatic pressure the authors were able to identify both the strain-shifted longitudinal optical phonon of CdSe quantum dots with different average size embedded in a quaternary ZnCdMgSe material and a Mg-local dot mode due to interdiffusion from the barrier. They show that the large tunability of the light emission, which covers most of the visible spectrum, is not only due to a different degree of confinement but also to a size-dependent built-in strain. The frequency of the Mg mode allowed them also to roughly estimate the amount of Mg interdiffusion into the quantum dots. © *2006 American Institute of Physics*. [DOI: 10.1063/1.2402881]

Strain-driven low-dimensional heterostructures of group II-VI semiconductors have been extensively studied because of their potential applications in optoelectronics. In particular, quantum dot (QD) structures are expected to lead to improvement in the performance of light emitting diodes and semiconductor lasers.[1] Important advances in the fabrication of these zero-dimensional structures have been obtained using different methods.[2,3] The CdSe/ZnCdMgSe system, for instance, is particularly attractive due to its intense photoluminescence (PL) even at room temperature and the wide energy range it offers to tune the QD emission. Recently, great progress has been achieved in the degree of control and reproducibility of the growth process by introducing Mg into the barrier material.[4] In this way, dots with unimodal size distributions are obtained, in which the average dot size and hence the emission energy of the CdSe QDs can be easily adjusted by varying the CdSe deposition time. Furthermore, the large gap-energy difference of 1 eV between CdSe and the quaternary barrier material allows for the tuning of the QD PL throughout the visible spectrum from the red to the blue.

In this letter we show how we made explicit use of the resonant enhancement of the Raman scattering signal to identify vibrational modes stemming from CdSe/ZnCdMgSe QDs of different sizes, from which we were able to determine the built-in strain and degree of Mg interdiffusion into the dots. Different laser lines were brought into resonance with the fundamental optical transition of the CdSe dots by applying high hydrostatic pressures up to 6 GPa. An important result concerns the observation of size-dependent strain effects from which follows that the band-gap tunability of the CdSe/ZnCdMgSe dot system is due to a non-negligible part of at least 18% to the reduction of the built-in strain with decreasing average dot size.

The CdSe/ZnCdMgSe samples were grown by molecular beam epitaxy on InP (001) substrates. First a 150 nm thick lattice-matched InGaAs buffer layer was deposited followed by a Zn exposure for later reduction of the defect density in the ZnCdMgSe barrier. A 6 nm ZnCdSe layer is used to promote the two-dimensional nucleation after which 400 nm of $Zn_{0.38}Cd_{0.23}Mg_{0.39}Se$ was grown as barrier material. Finally, pure CdSe is deposited for dot growth in the Stranski-Krastanow mode followed by another 130 nm barrier of $Zn_{0.38}Cd_{0.23}Mg_{0.39}Se$. A 6 nm ZnCdSe cap layer was used to prevent the oxidation of the barrier material. The average base radius of the QDs is about 47 nm, whereas their height is ranging between 3 and 15 nm depending on the CdSe deposition time. The QD density is about 7×10^8 cm^{-2}. Here we present data from two samples with deposited thicknesses of 3.6 and 5.9 ML of CdSe and room temperature emission peaking at 2.23 and 2.03 eV, respectively. More details of the sample growth and their structural characterization are given elsewhere.[4]

Resonant Raman measurements were performed in backscattering geometry using two different laser lines for excitation, 514.5 and 632.5 nm. Spectra were acquired with a LabRam HR800 micro-Raman system. In order to meet resonance conditions in the different samples we applied high hydrostatic pressures using the standard diamond anvil cell (DAC) technique. Spectra under pressure were measured with crossed linear polarization to suppress the reflected laser beam from the DAC. A 4:1 mixture of methanol and ethanol was employed as pressure-transmitting medium. Pressure was monitored *in situ* by the shift of the ruby $R1$ line.[5] The samples loaded in the DAC were previously chemically etched to a thickness of about 1 μm. An etchant solution of 3:2 HCl to H_3PO_4 was used to selectively etch away the InP substrate.

Figure 1 shows Raman scattering spectra of samples A and B with nominally 3.6 and 5.9 ML of CdSe, respectively, measured at ambient temperature and pressure conditions using the red (1.96 eV) and green (2.41 eV) laser lines for excitation. Up to four peaks are apparent in Raman spectra, from which the one at around 220 cm^{-1} and the broader peak centered slightly above 300 cm^{-1} are identified as the longitudinal-optical (LO) phonon of the CdSe dots and a Mg local mode also from the QDs, respectively. This assignment is based on the fact that the LO CdSe mode is only observed under near resonance conditions of the laser with the fundamental PL emission from the dots, which is attained with the

[a]Electronic mail: sebareparaz@hotmail.com

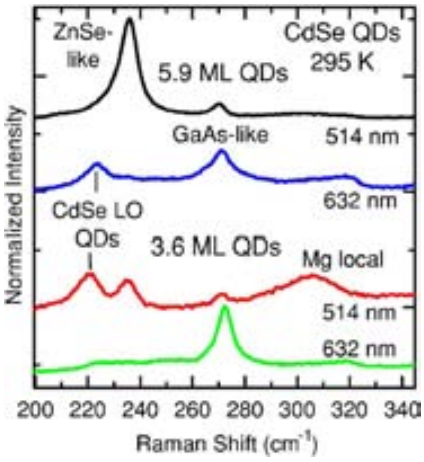

FIG. 1. (Color online) Polarized Raman spectra at ambient pressure and temperature conditions of samples A and B with nominally 3.6 and 5.9 ML of CdSe, respectively, using the red (632.5 nm) and green (514.5 nm) laser lines for excitation.

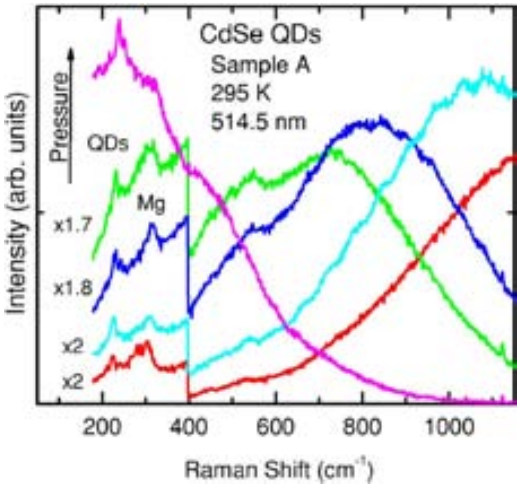

FIG. 2. (Color online) Evolution of the luminescence and resonant Raman peaks with hydrostatic pressure for sample A using the 514.5 nm laser line for excitation. The five spectra correspond to the pressure values: 0.8, 1.0, 1.8, 2.1, and 3.4 GPa.

green line for sample A and with the red line for sample B, as illustrated in Fig. 1. The 300 cm^{-1} Mg-local mode is also observed together with the 220 cm^{-1} peak for 514.5 nm excitation laser line, which suggests that Mg from the barrier is present inside the QDs. Although this peak is not observed when exciting with the red laser line, pressure measurements support this hypothesis. In contrast, both modes are absent in the Raman spectra of a control sample without CdSe dots but containing the barrier material, independently of the laser wavelength used for excitation. The peak at 235 cm^{-1}, which clearly resonates with green excitation in both samples, is attributed to the ZnSe-like LO mode of the 6 nm thick ZnCdSe cap layer, whereas the nonresonant Raman peak at 272 cm^{-1} corresponds to the GaAs-like LO phonon of the InGaAs buffer layer. We point out that the Raman selection rules measured with linearly polarized light at ambient pressure conditions are consistent with the previous assignment of the peaks.

In order to fully settle the issue of the identification of QD Raman modes, we have fine-tuned the fundamental PL emission of sample A to the energy of the 514 nm laser line by applying high hydrostatic pressure up to 6 GPa. In Fig. 2 we display several Raman spectra measured at small pressure steps in the range from 0.8 to 3.4 GPa. The broad band, which in this representation of the spectra as a function of relative wave numbers, shifts with increasing pressure towards the laser line corresponds to the PL emission from the CdSe dots. This is due to the strong increase with pressure of the energy of the fundamental optical transition of the dots with a slope of about 47 meV/GPa.[6] The only Raman peaks which resonate with the PL emission from the CdSe dots are the two ones previously assigned to the LO CdSe mode at around 220 cm^{-1} and the Mg-local mode near 300 cm^{-1}. Their Raman intensity is not only comparable to that of the dot PL but it also increases as these modes become more in outgoing resonance with the PL band, as the applied pressure increases. Interestingly, we observe a third Raman peak at around 520 cm^{-1} at low pressure, which is also in outgoing resonance with the CdSe QD emission (see Fig. 2). We believe that this Raman peak corresponds to exciton-mediated multiphonon scattering by a combination of the LO CdSe and the Mg-local mode due to strong electron-LO-phonon coupling in the highly polar II-VI compounds.[7]

Valuable information about the strain status of the CdSe dots is obtained from a quantitative analysis of the frequency and its pressure dependence of the QD vibrational modes. In Fig. 3 we have plotted for sample A the peak position of both QD phonon modes as a function of the applied pressure. The solid lines represent the result of least-squares fits to the data points using linear functions yielding

$$\omega_{\text{LO-CdSe}} = 219(1)\ \text{cm}^{-1} + 5.4(3)\ \frac{\text{cm}^{-1}}{\text{GPa}} \times P, \tag{1}$$

$$\omega_{\text{Mg-local}} = 301(2)\ \text{cm}^{-1} + 7.5(8)\ \frac{\text{cm}^{-1}}{\text{GPa}} \times P, \tag{2}$$

where P is the external hydrostatic pressure in GPa. The large difference in the pressure slopes is only apparent and almost vanishes after normalization by the mode frequency to calculate the mode Grüneisen parameter according to $\gamma_i = -(B_0/\omega_i(0))(\delta\omega_i/\delta P)$, where $B_0 = 53$ GPa is the bulk

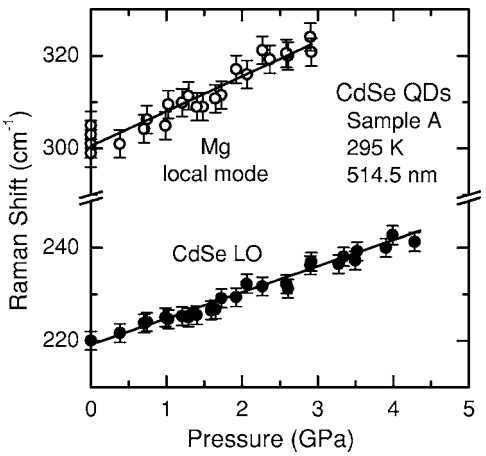

FIG. 3. Pressure dependence of the mode frequencies in sample A for the LO CdSe and Mg-local modes. The different values quoted at zero pressure for the Mg-local mode correspond to spectra measured outside the DAC with the four possible configurations of the linear polarization of incident and scattered beams.

modulus of CdSe (Ref. 8) and $\omega_i(0)$ is the mode frequency in cm^{-1} at zero pressure. For the LO CdSe and the Mg-local mode of the dots we obtain $\gamma=1.30\pm0.08$ and $\gamma=1.32\pm0.12$, respectively. The peak position of the broad band corresponding to the Mg-local mode at ambient pressure ranges from 300 to 305 cm^{-1} depending on the linear polarization configuration (see Fig. 3). The lower frequencies are obtained with crossed polarization, as for the Raman measurements under pressure, explaining why extrapolated value from the fit to the pressure data points at $P=0$ is at 301 cm^{-1}.

Both the frequency of the Mg-local mode at zero pressure and the coincidence of its Grüneisen parameter with that of the LO phonon indicate a low degree of Mg interdiffusion from the quaternary barrier into the nominally pure CdSe dots. Using a modified linear diatomic-chain model for the calculation of the Mg local-mode frequency in a zinc blende CdSe and ZnSe host[9] and by comparing with the only available data for $Zn_{1-x}Mg_xSe$ alloys,[10] the zero-pressure frequency of 305 cm^{-1} measured with parallel polarization at ambient pressure gives an upper bound for the Mg concentration in the QDs in the 1% range.

Returning to the LO mode of the CdSe QDs, its zero-pressure value of 219 cm^{-1} for sample A appears to be blueshifted by 14 cm^{-1} from the bulk value of 205 cm^{-1}.[11] This is due to the large built-in strain in the quantum dots.[12] Using the pressure coefficient of Eq. (1) we infer that the LO phonon of the dots senses an average compressive stress of about 2.6 GPa.[13] This huge internal pressure has an impact on the electronic as well as optical properties of the CdSe QDs. For instance, using the measured pressure coefficient for the PL dot emission of about 47 meV/GPa (Ref. 6) it turns out that the energy of the fundamental optical transition contains a strain-induced blueshift of approximately 120 meV.

A striking result is obtained by comparing the ambient pressure values of the LO phonon of the dots for sample A (219 cm^{-1}) and sample B (223 cm^{-1}). The small difference of 4 cm^{-1}, which is systematic and beyond experimental uncertainty, indicates that the built-in compressive stress in sample B is about 0.75 GPa larger than in sample A. This gives clear evidence that bigger dots are subjected to larger average internal stresses, as predicted by valence-force field calculations of the strain distribution in lattice mismatched dot structures.[14] These results indicate that the hydrostatic (main) component of the average built-in strain varies from $\approx\Delta\epsilon$, the lattice mismatch, for the case of very flat quantum dots with aspect ratios (base length over dot height) over 10 up to a value as high as $3\Delta\epsilon$ for large size dots for which the aspect ratio tends to unity. This reflects the change in strain status from a biaxially strained thin layer to a three-dimensional situation, where the dot is strained in all directions. Again, the 0.75 GPa stress difference between the larger QDs of sample B as compared with the smaller ones of sample A translates into an energy shift of 35 meV for the fundamental dot emission. Although this is only 18% of the actual energy difference of 200 meV between the PL peaks in both samples, which is mainly given by quantum confinement, it is now obvious that size-dependent strain effects cannot be neglected at all for an accurate tuning of the QD optical emission.

In summary, we have applied high hydrostatic pressure to samples of self-assembled CdSe quantum dots with ZnCdMgSe barriers in order to identify the vibrational modes of the dots by the resonant enhancement of their Raman intensity. This technique allowed us to detect a small amount of interdiffused Mg from the barriers and, what is more important, to probe the internal strain status of the dots. An interesting observation concerns the fact that the built-in strain of the CdSe QDs scales with their average size, an effect which ought to be considered along with quantum confinement for any quantitative analysis of the electronic, optical, and vibrational properties of this low-dimensional semiconductor system.

One of the authors (J.S.R.) acknowledges financial support from the AlBan Fellowship Program. This work was supported in part by the Spanish Ministerio de Educación y Ciencia through Grant No MAT2003-00738 Another author (A.R.G) is a ICREA Research professor.

[1] *Nano-Optoelectronics*, edited by M. Grundmann (Springer, Berlin, 2002).
[2] C. B. Murray, D. J. Norris, and M. G. Bawendi, J. Am. Chem. Soc. **115**, 8706 (1993).
[3] T. Tawara, S. Tanaka, H. Kumano, and I. Suemune, Appl. Phys. Lett. **75**, 235 (1999).
[4] M. N. Perez-Paz, X. C. Zhou, M. Munoz, H. Lu, M. Sohel, M. C. Tamargo, F. Jean-Mary, and D. L. Akins, Appl. Phys. Lett. **85**, 6395 (2004).
[5] H. K. Mao, J. Xu, and P. M. Bell, J. Geophys. Res. **91**, 4673 (1986).
[6] J. S. Reparaz, A. R. Goñi, M. I. Alonso, M. N. Perez-Paz, and M. C. Tamargo, Phys. Status Solidi B (to be publilshed).
[7] R. M. Martin and C. M. Varma, Phys. Rev. Lett. **26**, 1241 (1971); A. García-Cristobal, A. Cantarero, C. Trallero-Giner, and M. Cardona, Phys. Rev. B **49**, 13430 (1994).
[8] M. L. Cohen, Phys. Rev. B **32**, 7988 (1985).
[9] G. Lucovsky, M. H. Brodsky, and E. Burstein, Phys. Rev. B **2**, 3295 (1970).
[10] D. M. Huang, C. X. Jin, D. H. Wang, X. H. Liu, J. Wang, and X. Wang, Appl. Phys. Lett. **67**, 3611 (1995).
[11] A. P. Alivisatos, T. D. Harris, L. E. Brus, and A. Jayaraman, J. Chem. Phys. **89**, 5979 (1988).
[12] H. Rho, H. E. Jackson, S. Lee, M. Dobrowolska, and J. K. Furdyna, Phys. Rev. B **61**, 15641 (2000).
[13] Strain profiles calculated within different self-consistent elasticity theories indicate that the average hydrostatic strain in the central region of a quantum dot, as probed by Raman scattering, is in good approximation homogeneous. See, for example, C. Pryor, J. Kim, L. W. Wang, A. J. Williamson, and A. Zunger, J. Appl. Phys. **83**, 2548 (1998).
[14] C. Kristukat, Ph.D. thesis Technische Universität Berlin, Berlin, 2006; http://opus. kobv. de/tuberlin/volltexte/2006/1237/pdf/kristukat_christian. pdf.

Original Paper

phys. stat. sol. (b) **244**, No. 1, 397–401 (2007) / **DOI** 10.1002/pssb.200672523

Photoluminescence of CdSe quantum dots with $Zn_{0.38}Cd_{0.23}Mg_{0.39}Se$ barriers under hydrostatic pressure

J. S. Reparaz[*, 1], **A. R. Goñi**[**, 1], **M. I. Alonso**[1], **M. N. Perez-Paz**[2], and **M. C. Tamargo**[2]

[1] Institut de Ciència de Materials de Barcelona (ICMAB) – CSIC, Esfera UAB, 08193 Bellaterra, Spain
[2] Department of Chemistry, City College of The City University of New York, New York, NY 10031, USA

Received 4 July 2006, accepted 18 August 2006
Published online 27 November 2006

PACS 62.50.+p, 71.55.Gs, 78.55.Et, 78.67.Hc

We have investigated the pressure dependence of the room-temperature photoluminescence (PL) of self-assembled CdSe quantum dots (QDs) with quaternary ZnCdMgSe barriers. Four samples with different CdSe deposition times, i.e. different average dot size, were studied. Samples exhibit a very distinct emission energy covering the visible spectrum from the red to the blue. We found, however, a similar pressure coefficient of around 47 meV/GPa for the PL emission of all samples. This value is close to that of bulk CdSe, which gives evidence that dot and quaternary barrier material have a similar compressibility. In contrast, the PL linewidth displays a clear trend with respect to the emission energy, the PL line being broader for the smaller dots emitting in the blue. This is explained by taking into account the huge band-gap offset of ≈1 eV between dot and barrier and considering quantum confinement effects within a very simplistic infinitely deep square-well model.

1 Introduction

Self-assembled quantum dots (QDs) of II–VI semiconductor compounds have drawn increasing attention for their potential applications in optoelectronics, mainly in the green-blue spectral region [1, 2]. In particular, the CdSe/ZnCdMgSe system with a quaternary barrier material containing Mg appeared recently as a strong candidate for light emitters due to its intense photoluminescence (PL) even at room temperature and the wide energy range of tunability of the QD emission. The key development was the introduction of Mg into the barrier material, which allows for a reduction of the lattice mismatch between CdSe and the barrier but retaining their large band-gap difference. In this respect, great progress has been achieved in the degree of control and reproducibility of the growth process of the heterostructures containing Mg [3]. As a result, dots with unimodal size distributions are obtained, in which the average dot size and hence, the emission energy of the CdSe QDs, can be easily adjusted by varying the CdSe deposition time. Furthermore, the afore mentioned gap-energy difference of ~1 eV between CdSe and the quaternary barrier material allows for the tuning of the QD PL throughout the visible spectrum from the red to deep into the blue.

In this work we report on the pressure dependence of the PL emission of CdSe QDs with ZnCdMgSe barriers for pressures up to 6 GPa. We found that the pressure coefficients of four different samples with different CdSe deposition times (PL emission energies) are all very similar to the one of *bulk* CdSe. We interpret this effect as evidence that the bulk modulus of the dot and the quaternary barrier material are

* Corresponding author: e-mail: jsreparaz@icmab.es, Fax: +34 93 580 57 29
** ICREA Research Professor

close to each other. Furthermore, we observe that the linewidth of the PL emission increases with decreasing QD size. For very flat dots with aspect ratios (height over base length) below 0.1, like the ones we are dealing with here, such a behavior is explained as the result of the combined effects of strong confinement in growth direction with infinitely high barriers and localization in the base plane due to layer width fluctuations. The PL intensity of the CdSe dots also increases with increasing pressure, which is consistent with the excitonic character of the QD emission.

2 Experimental details

The CdSe/ZnCdMgSe samples were grown by molecular beam epitaxy on InP (001) substrates. First a 150 nm thick lattice-matched InGaAs buffer layer was deposited followed by a Zn exposure for later reduction of the defect density in the ZnCdMgSe barrier. A 6 nm ZnCdSe is used to promote the two dimensional nucleation after which 400 nm of $Zn_{0.38}Cd_{0.23}Mg_{0.39}Se$ as barrier material was grown. Pure CdSe is then deposited for the growth of the dots in the Stranski–Krastanow mode and capped with another 130 nm of $Zn_{0.38}Cd_{0.23}Mg_{0.39}Se$. A 6 nm ZnCdSe cap layer was used to prevent the oxidation of the barrier material. The average base radius of the QDs is 47 nm, whereas their height is ranging between about 3 to 15 nm depending on the CdSe deposition time. The QD density is about 7×10^8 cm^{-2}. Here we present data from four samples, with room temperature emission peaking at 2.23, 2.10, 2.03 and 1.91 eV, corresponding to equivalent CdSe coverages of 3.6, 4.8, 5.8, and 7.1 monolayers (MLs), respectively. A detailed description of the sample growth and their structural characterization is given elsewhere [3].

Luminescence spectra were acquired with a LabRam HR800 micro-Raman system using as excitation the 514.5 nm line of an Ar^+ laser. We applied high hydrostatic pressures using the standard diamond anvil cell (DAC) technique. A 4:1 mixture of methanol and ethanol was employed as the pressure-transmitting medium. Pressure was monitored *in situ* by the shift of the ruby R1 line [4]. The samples loaded in the DAC were previously thinned to about 1 micron by wet etching. The solution used to selectively etch away the InP substrate was a 3:2 HCl and H_3PO_4 mixture and the etching time was about 90 minutes.

3 Results and discussion

Figure 1 shows the pressure dependence of the PL emission for the four samples with 7.1, 5.8, 4.8 and 3.6 ML of CdSe, measured at room temperature and using as excitation the 514.5 nm laser line. Quadratic fits to the data points are also shown as solid lines and the corresponding parameters are listed in

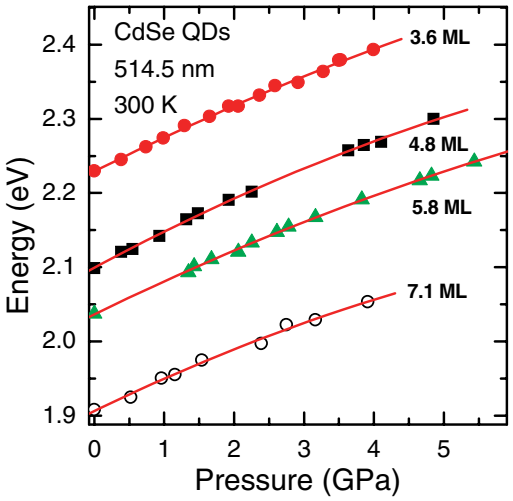

Fig. 1 (online colour at: www.pss-b.com) Energy position of the PL emission as a function of pressure at room temperature for the four samples with different average QD size expressed in nominally deposited CdSe monolayers. All spectra were measured using the 514.5 nm laser excitation line. Curves represent the results of quadratic fits to the data points.

Table 1 Parameters of the quadratic fits for the four samples.

sample	$E_{P=0}$ (eV)	dE/dP (eV/GPa)	d^2E/dP^2 (eV/GPa^2)
7.1 ML	1.906(4)	0.046(5)	−0.0020(3)
5.8 ML	2.036(2)	0.046(2)	−0.0015(3)
4.8 ML	2.100(2)	0.050(2)	−0.0020(4)
3.6 ML	2.230(3)	0.047(3)	−0.0015(6)

Table 1. Within experimental uncertainty the first order coefficients dE/dP are the same for all the samples, being in average 47 meV/GPa. Moreover, this value is in the range of pressure coefficients measured for bulk (wurtzite) CdSe [5].

These two apparently trivial results of the independence of the PL pressure coefficient on QD size and its similarity to the bulk value are at odds with what is known from optical transitions in InAs/GaAs dot systems [6, 7] and phonons in Ge/Si quantum dots [8, 9]. The former effect of the size independence of the PL pressure coefficient can be understood in terms of the large barrier height of the quantum well, that in our case is about 1 eV as maximum. Since the barrier gap is about 2.87 eV and the emission of the measured samples ranges between 1.9 and 2.23 eV, in all cases the discrete energy levels are deeply confined into the CdSe quantum dot. In other words, the wave function of the exciton is spatially fully confined within the QDs for all the samples. In other systems with shallower confining potential barriers such as InAs/GaAs [6, 7], there is substantial penetration of the exciton wave function into the barrier, which leads to an increase of the slope dE/dP with decreasing dot size. Measurements under pressure for smaller CdSe QDs are currently being performed to clarify this point.

The fact that the PL emission of the dots exhibits the same pressure coefficient as in bulk CdSe is also atypical. A common feature of self-assembled dots is that they are compressibly stressed by the barrier material which possess the lower lattice parameter. This, in turn, usually means a lower compressibility of the barrier with respect to the dot material. Under external hydrostatic pressure the elastic properties of the dot structure are determined by those of the barrier material, i.e. for the same pressure the volume change of the dots is smaller than for the bulk material without barrier surrounding it. In this way, a reduction up to 50% in the pressure coefficient of optical transitions or phonon modes is observed. Unfortunately, very little is known about the elastic properties of quaternary CdZnMgSe with such a high Mg concentration but the similarity of the pressure coefficient of the CdSe dot and bulk band gap is a strong indication that the bulk modulus of the barrier material matches that of CdSe.

Representative PL spectra of all four samples measured at room temperature and ambient pressure are shown in Fig. 2. Strikingly, the PL linewidth increases with decreasing QD size. This behavior is again

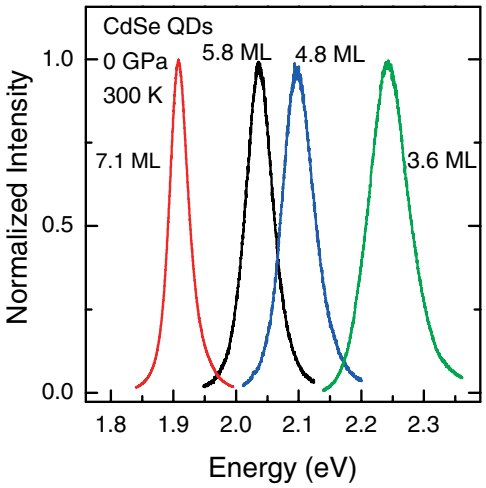

Fig. 2 (online colour at: www.pss-b.com) Photoluminescence spectra of the four samples taken at ambient pressure and temperature conditions using the 514.5 nm laser excitation line.

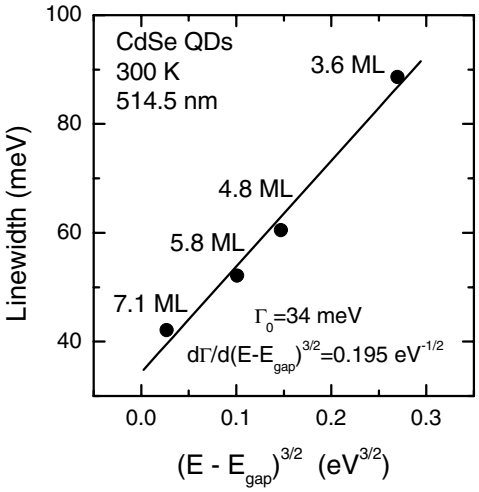

Fig. 3 PL linewidth at zero pressure and room temperature versus reduced energy. The solid line represents the prediction of the infinitely deep quantum well model.

opposite to what is observed in other systems, for instance, in InAs/GaAs [10]. The full-width half-maximum (FWHM) of the PL peaks at room temperature are plotted in Fig. 3 as a function of the emission energy for the four samples. The choice of variable for the *x*-axis is explained below. A similar observation was already made at lower temperatures (77 K) and a preliminary explanation in terms of enhanced interface effects in the smaller dots was given [3]. Here we show that dot-height fluctuations combined with exciton localization within the base plane of the dots are mainly responsible for this quantum size dependent broadening.

Generally speaking, the PL linewidth $\Gamma = \Gamma_Q + \Gamma_0$ can be separated into two contributions, a size-dependent part Γ_Q due to inhomogeneous broadening and the intrinsic part Γ_0 containing the homogeneous linewidth, broadening due to thermal effects (phonons and interlevel transitions) and spectral diffusion [11]. The physical picture of the processes contributing to Γ_Q is the following: We are dealing with dots characterized by very low aspect ratios, for which quantum confinement in the growth direction given by the height is at least one order of magnitude larger than in the base plane. Furthermore, excitons in CdSe possess a large binding energy, i.e. a very small Bohr radius of about 5 nm. Thus, excitons are very likely to become localized in the base plane of the dots due to height fluctuations in a totally similar manner as in a conventional thin quantum well [12]. The size-dependent broadening is then determined by the variations of the confinement energy due to dot-height fluctuations as $\Gamma_Q = |\Delta E_{PL}|$. Due to the huge band offsets of about 1 eV this contribution can be readily calculated for the ground state emission using a simple model of an infinitely deep quantum well of width L according to

$$E_{PL} = E_{gap} + \frac{\hbar^2\pi^2}{2\mu L^2} \rightarrow |\Delta E_{PL}| = \frac{\hbar^2\pi^2}{\mu L^3}\Delta L\,, \tag{1}$$

where $\hbar$ is the Planck constant, μ is the exciton reduced mass, and ΔL is the well-width fluctuation. By replacing in Eq. (1) L^{-3} by its expression in terms of the reduced energy $E - E_{gap}$ we finally obtain for the size-dependent broadening

$$\Gamma_Q = \frac{\sqrt{8\mu}}{\hbar\pi}\Delta L\,(E - E_{gap})^{3/2} \tag{2}$$

where E_{gap} is 1.82 eV for strained CdSe. As illustrated in Fig. 3, the experimental linewidths, when plotted as a function of $(E - E_{gap})^{3/2}$, are well fitted with a linear functions. The fitting parameters are given in the figure. From the slope of the linear fit and using Eq. (2) we obtain an estimate for the mean value of the dot height fluctuations of 0.2 nm corresponding to ≈ 0.7 MLs.

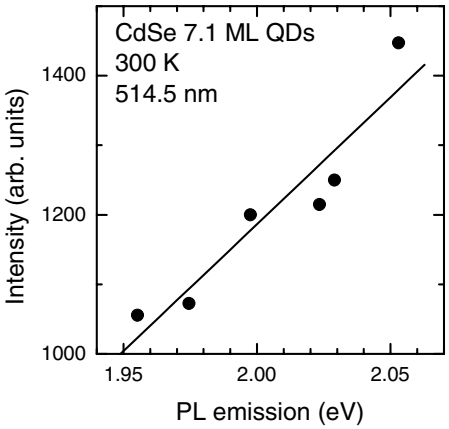

Fig. 4 PL intensity of the QD peak at room temperature as a function of the PL peak emission energy for the sample emitting in the red. The solid line represents the result of a linear fit to the data points.

We notice that Eq. (2) predicts an increase of the linewidth with pressure, since the reduced effective mass μ of the exciton is proportional to the gap energy, i.e. $E_{\mathrm{PL}}(P)$ [13]. Such pressure-induced broadening, however, is too small (≈1 meV) to be detected in the pressure range of our experiments. The PL intensity, in contrast, is expected also to increase but at an appreciable pace being proportional to $E_{\mathrm{PL}}^{3/2}(P)$ [13]. Figure 4 shows the peak intensity of the emission from the sample with the larger dots as a function of the emission energy. The PL intensity indeed increases linearly with pressure-tuned emission energy, as expected for excitonic transitions.

In summary, we have determined the pressure dependence of the PL emission of CdSe QDs of different size for pressures up to 6 GPa. From the similarity between the pressure coefficients of the dot and CdSe bulk optical transition energy we infer that the bulk modulus of the ZnCdMgSe barrier material is close to that of CdSe. Information about the linewidth was obtained from measurements at room temperature and zero pressure. The mechanism responsible for the peak broadening with decreasing the QDs size is explained in terms of localization effects and quantum width fluctuations within an infinite quantum well model.

Acknowledgements JSR acknowledges financial support by the AlBan fellowship Program. This work was supported in part by the Spanish Ministerio de Educación y Ciencia through grant MAT2003-00738.

References

[1] C. B. Murray, D. J. Norris, and M. G. Bawendi, J. Am. Chem. Soc. **115**, 8706 (1993).
[2] T. Tawara, S. Tanaka, H. Kumano, and I. Suemune, Appl. Phys. Lett. **75**, 235 (1999).
[3] M. N. Perez-Paz, X. C. Zhou, M. Munoz, H. Lu, M. Sohel, M. C. Tamargo, F. Jean-Mary, and D. L. Akins, Appl. Phys. Lett. **85**, 6395 (2004).
[4] H. K. Mao, J. Xu, and P. M. Bell, J. Geophys. Res. **91**, 4673 (1986).
[5] W. Shan, W. Walukiewicz, J. W. Ager III, K. M. Yu, and J. Wu, Appl. Phys. Lett. **84**, 67 (2004).
[6] F. Manjón, A. R. Goñi, K. Syassen, F. Heinrichsdorff, and C. Thomsen, phys. stat. sol. (b) **235**, 496 (2003).
[7] C. Kristukat, A. R. Goñi, K. Pötschke, D. Bimberg, and C. Thomsen, to be published in phys. stat. sol. (b) **244**, 53 (2007) (this issue).
[8] K. L. Teo, L. Qin, Z. X. Shen, and O. G. Schmidt, Appl. Phys. Lett. **80**, 2919 (2002).
[9] A. Bernardi, J. S. Reparaz, A. R. Goñi, M. I. Alonso, and M. Garriga, phys. stat. sol. (b) **244**, No. 1 (2007) (this issue).
[10] M. I. Alonso, M. Ilg, and K. H. Ploog, Phys. Rev. B **50**, 1628 (1994).
[11] S. A. Empedocles and M. G. Bawendi, J. Phys. Chem. B **103**, 1826 (1999).
[12] We rule out ordinary inhomogeneous broadening effects due to averaging the measured PL emission over the dot ensemble with different dot heights because of the very low areal density of the samples and the fact that the signal was collected with confocal optics, for which only seven dots lie within the laser spot of 1 micron.
[13] A. R. Goñi, A. Cantarero, K. Syassen, and M. Cardona, Phys. Rev. B **41**, 10111 (1990).

3.3.3 Conclusions

CdSe/ZnCdMgSe dots were studied by combining Raman spectroscopy with high pressure measurements. This system turns out to be of particular interest due its high degree of reproducibility concerning its growth mechanism. Different built-in strain for dots with different height were found and its contribution to the bandgap tuning resulted in about 18%. Interdiffusion of Mg from the barrier into the QDs was observed in resonant conditions, which were achieved using high pressure. Finally, no differences in the elastic properties of dots with different sizes were observed from the high pressure measurements.

Bibliography

[1] M. N. Perez-Paz, X. C. Zhou, M. Munoz, H. Lu, M. Sohel, M. C. Tamargo, F. Jean-Mary, and D. L. Akins, Appl. Phys. Lett. **85**, 6395 (2004).

[2] C. B. Murray, D. J. Norris, and M. G. Bawendi, J. Am. Chem. Soc. **115**, 8706 (1993).

[3] Y. H. Cho, B. J. Kwon, J. Barjon, J. Brault, B. Daudin, H. Mariette, and L. S. Dang, Appl. Phys. Lett. **81**, 4934 (2002).

[4] T. Tawara, S. Tanaka, H. Kumano, and I. Suemune, Appl. Phys. Lett. **75**, 235 (1999).

[5] F. Flack, V. Nikitin, P. A. Crowell, J. Shi, J. Levy, N. Samarth, and D. D. Awschalom, Phys. Rev. B **54**, R17312 (1996).

[6] M. Muñoz, S. Guo, X. Zhou, M. C. Tamargo, Y. S. Huang, C. Trallero-Giner, and A. H. Rodríguez, Appl. Phys. Lett. **83**, 4399 (2003).

[7] K. Arai, A. Ohtake, T. Hanada, S. Miwa, T. Yasuda, and T. Yao, Thin Solid Films **357**, 1 (1999).

[8] V. S. Bagaev, V. V. Zaitsev, E. E. Onishchenko, and Yu. G. Sadofyev, J. Cryst. Growth **214/215**, 250 (2000).

[9] T. Yao, M. Fujimoto, S. K. Chang, and H. Tanino, J. Cryst. Growth **823**, 111 (1991).

Chapter 4

Complementary Articles

Site-controlled growth of Ge nanostructures on Si(100) via pulsed laser deposition nanostenciling

C. V. Cojocaru
INRS—Énergie, Matériaux et Télécommunications, Université du Québec, 1650 Boul. Lionel-Boulet, Varennes, Quebec J3X 1S2, Canada

A. Bernardi, J. S. Reparaz, and M. I. Alonso
Institut de Ciència de Materials de Barcelona-CSIC, Esfera UAB, 08193 Bellaterra, Spain

J. M. MacLeod, C. Harnagea, and F. Rosei[a)]
INRS—Énergie, Matériaux et Télécommunications, Université du Québec, 1650 Boul. Lionel-Boulet, Varennes, Quebec J3X 1S2, Canada

(Received 12 July 2007; accepted 20 August 2007; published online 14 September 2007)

The authors combine nanostenciling and pulsed laser deposition to pattern germanium (Ge) nanostructures into desired architectures. They have analyzed the evolution of the Ge morphology with coverage. Following the formation of a wetting layer within each area defined by the stencil's apertures, Ge growth becomes three dimensional and the size and number of Ge nanocrystals evolve with coverage. Micro-Raman spectroscopy shows that the deposits are crystalline and epitaxial. This approach is promising for the parallel patterning of semiconductor nanostructures for optoelectronic applications. © *2007 American Institute of Physics*. [DOI: 10.1063/1.2783473]

The growth of germanium (Ge) thin films and structures on silicon (Si) surfaces has been the subject of extensive study due to the prospective device applications[1,2] and the fundamental research importance vis-à-vis the understanding of growth processes.[3–7] In the quest to expand integrated silicon technology, in particular, to applications in optoelectronics, Ge/Si nanoheterostructures[8] with engineered band structures have come under intense investigation as important candidates for light-emitting quantum dot (QD) based devices.

Abundant research efforts have been dedicated to the exploration of "dotlike" structures obtained via the Stranski-Krastanov (SK) growth mode, which comprises the formation of a wetting layer (WL) followed by three-dimensional island ("dot") formation that relaxes the strain induced by the 4.2% lattice mismatch between Ge and Si. To control the size, shape, and density, but mostly the spatial positioning of Ge dots, many strategies including combinations of lithography-based (top down) and spontaneous self-organization approaches (bottom up) have been pursued.[9–14] Much work has focused on the assisted organization of Ge dots grown on prepatterned Si or SiO_2 substrates either by chemical vapor deposition[15,16] (CVD) or molecular beam epitaxy (MBE).[17–19]

While CVD and MBE have been extensively used, pulsed laser deposition (PLD) emerged just recently[20] as a versatile tool to study the structural[21] and functional[22] properties of self-assembled Ge QDs on silicon substrates. A well-established technique developed mainly to grow high-quality epitaxial films of complex materials,[23] PLD offers additionally the possibility of fine tuning and controlling deposition parameters rather easily in the case of elemental materials. We previously investigated a promising unconventional patterning approach based on direct, selective PLD of functional materials at *room temperature* through solid-state, reusable nanostencils. This strategy leads to the organization of nanostructures without any pre patterning or complementary invasive process prior applied to the substrates.[24]

In this letter we describe the patterning of Ge/Si semiconductor heterostructures via PLD nanostenciling at *high temperature* (600 °C). The intent of this approach is twofold: first, to investigate the kinetic processes of PLD of Ge nanodots and ultimately to compare it with more studied processes such as MBE or CVD, and, second, to demonstrate a flexible approach to gain control over the positioning of ordered arrays of nanostructures with potential applications in device engineering.

To achieve precise positioning of Ge on Si(100), we used nanostencils with hexagonal arrays of circular apertures opened in freestanding, low-stress SiN membranes.[25] These miniature shadow masks were mechanically clamped onto the substrate and the substrate-stencil assembly mounted in front of a rotating Ge solid target (99% purity) [Fig. 1(a)]. Prior to deposition, Si(100) substrates (*n* type, Sb doped resistivity of 0.015 Ω cm) were cleaned in ultrasound solvent baths. The native oxide layer was chemically removed in a 5% HF solution. Ge deposition was performed in high vacuum ($\sim 10^{-5}$ mbar), using a GSI Lumonics KrF excimer laser ($\lambda = 248$ nm, $\tau = 15.4$ ns) at a repetition rate of 10 Hz and laser fluence on the target of 4 J/cm^2. The substrate temperature was set at 600 °C and the same stencil was used in consecutive depositions.[26]

Swift fabrication of ordered arrays of Ge structures was achieved in a single deposition step [Fig. 1(b)]. In the initial stages of growth (up to 250 laser ablation pulses) ordered arrays of Ge structures are formed as flat circular mounds, 350 nm in diameter and with a 700 nm periodicity [Fig. 1(c)], i.e., the replica of the design defined by the sieve's apertures. In Fig. 2, scanning electron microscopy (SEM) micrographs for four samples illustrate the patterned Ge islands obtained on Si(100) by varying the number of laser pulses between 250 and 1500 with an estimated rate of ~0.28 Å/pulse. SEM micrographs show that with increasing Ge thickness, the shapes of the obtained structures evolve

[a)]Electronic mail: rosei@emt.inrs.ca

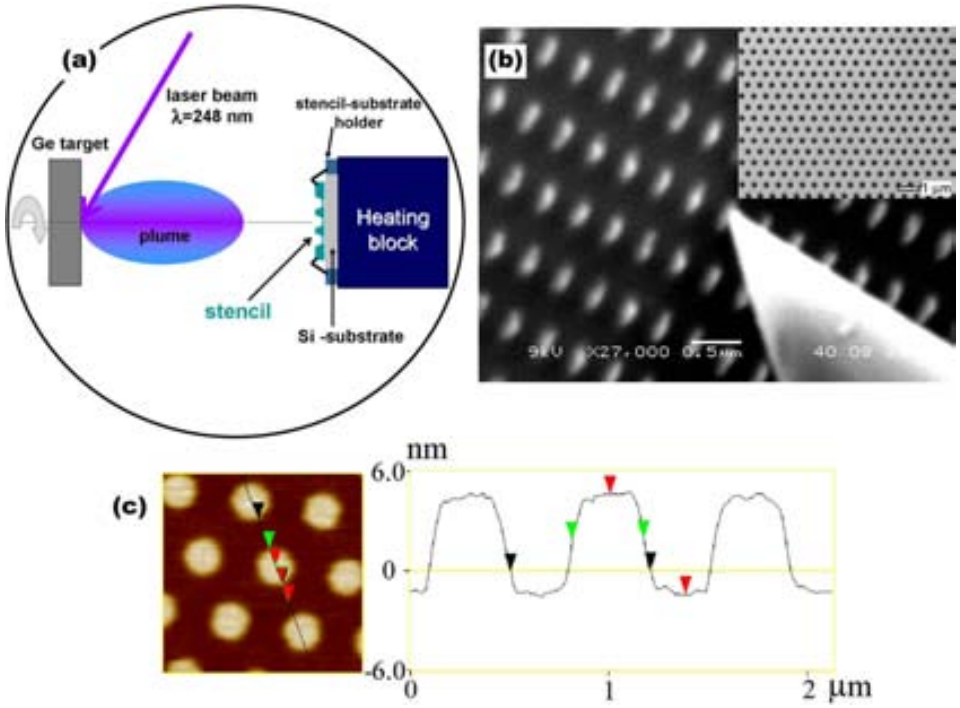

FIG. 1. (Color online) Experimental setup used for stencil deposition and further characterization of Ge ordered arrays: (a) schematic drawing of the PLD-based Ge direct patterning process achieved at high temperature through SiN stencils attached to the Si(100) substrates; (b) SEM micrograph showing an AFM tip scanning across the Ge patterned area in a JEOL-4500 UHV AFM-STM-SEM microscope. The inset shows a detail of a perforated freestanding SiN membrane built in the stencil chip; (c) AFM topography and Ge mound height profile obtained for 250 pulses deposited at 600 °C using a stencil with the architecture shown in the inset (b).

from the flat "two-dimensional (2D)-mound" type [Fig. 2(a)] to three-dimensional (3D) nanocrystalline agglomerations (10–100 nm in lateral size) formed on top of these mounds [Fig. 2(b)], undergoing further a transition to a "coffee-bean-like" grained structure [Fig. 2(c)], and finally coalescing into single nanocrystals [Fig. 2(d)]. Atomic force microscopy (AFM) and SEM images from Figs. 1 and 2 show that all islands are perfectly separated and well defined. The lateral extent of the deposits is always restricted to the range of the aperture areas defined in the stencil.

Micro-Raman spectroscopy was used to provide a structural characterization of the Ge clusters. The optical measurements were carried out by probing the patterned area with the 514.5 nm line of an Ar^+ ion laser focused with a spot size of about 1 μm, i.e., each Raman spectrum (Fig. 3) is collected from the region of two to three apertures. The spectral position and shape of the Ge–Ge phonon mode reveal that the Ge clusters are crystalline, and the absence of the Si–Ge phonon band around ~400 cm^{-1} (inset in Fig. 3) clearly indicates that there is no Si intermixing. Further, the Ge–Ge phonon peak becomes more intense with increased

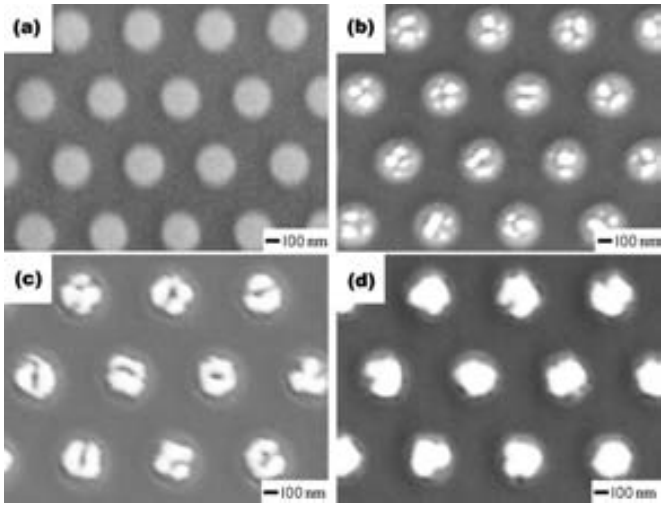

FIG. 2. Coverage dependence of Ge morphology: SEM micrographs showing ordered Ge nanostructures replicated on Si(100) by PLD at 600 °C, for (a) 250, (b) 750, (c) 1250, and (d) 1500 laser pulses with a fluence of 4 J/cm2, for a target-substrate distance of 6.5 cm.

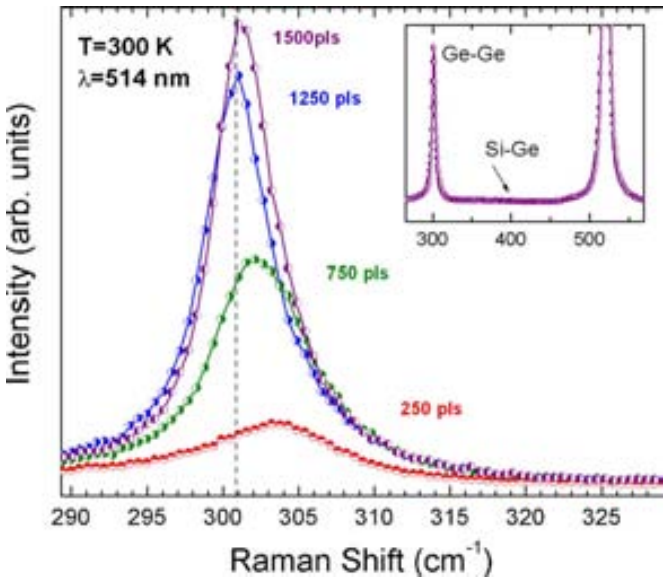

FIG. 3. (Color online) Raman spectra acquired by probing the Ge patterned areas with the 514.5 nm line of an Ar+ ion laser. The absence of the Si–Ge phonon band around ~400 cm^{-1} (see inset) indicates no trace of Si intermixing.

Ge coverage. Spectra recorded after the initial stages of growth exhibit a blueshifted Ge–Ge phonon frequency ($\sim 303\ \mathrm{cm}^{-1}$) attributed to compressive strain ($\varepsilon < -1\%$) at the island-substrate interface.[27] The strain is progressively relieved for taller clusters (i.e., higher Ge coverage) whose phonon frequency approaches the value expected for bulk Ge ($300.8\ \mathrm{cm}^{-1}$). The presence of built-in strain suggests that the Ge nanostructures match the Si substrate lattice. In fact, they retain the substrate crystallographic orientation, as confirmed by the phonon selection rules in polarized Raman measurements (not shown here).

The 2D mounds are reminiscent of the thin WL which normally precedes islanding in classical SK growth. AFM topographies indicate that the 2D mounds grow to a maximum height of 6–7 nm, roughly ten times thicker than the critical value for a conventional Ge WL.[28] The anomalous critical thickness for the onset of 3D nucleation can be explained by invoking the finite size of the deposited areas: the 2D mounds, acting as a WL, relieve strain at their periphery, delaying the strain-induced 3D nucleation of structures. Similar phenomenology was discussed in the case of self-assembling of Ge on lithography-patterned windows opened in ultrathin silicon oxide layers.[29]

The dots that initially nucleate on top of the 2D mounds [Fig. 2(b)] are round shaped and their aspect ratios (defined as the dot's height divided by the square root of the base area) range from ~0.16 to ~0.20. These dots are reminiscent of the dome-shaped islands observed in Ge/Si(001) heteroepitaxy.[30] The average aspect ratio of the dots increases with coverage to allow for more efficient strain relaxation. Above 500 pulses, we observe a shape transition from rounded to "coffee-bean" dots [Fig. 2(c)]. At this stage of growth, we detect both coalescence of grains and the formation of a depletion region at the center of the underlying 2D mounds, where we expect higher elastic compression. Finally, at higher Ge coverage (above 1000 ablation pulses), the depletion region disappears and is replaced by a single rounded cluster.

The number of Ge dots is of the order of tens per aperture for the samples deposited from 250 up to 500 pulses. For samples deposited up to 1000 pulses, the dots are larger and less numerous [e.g., three to five dots/aperture as shown in Fig. 2(b)]. This implies a feasible control over the number of dots per nominal location and thus their density in the whole patterned area.[31]

In summary, we showed that combining nanostenciling with PLD provides a flexible approach to grow and pattern crystalline Ge/Si nanostructures. The location of the Ge clusters is entirely controlled by the pattern of the nanostencil, and the density and physical dimensions of the dots can be further adjusted by varying the deposition parameters. The morphological evolution of the structures with coverage follows a modified Stranski-Krastanov growth mode due to the finite size of the WL in each aperture location. Raman spectroscopy indicates that the nanostructures are crystalline Ge and that they follow the substrate's crystallographic orientation. In future work we will establish a correlation between the deposition parameters such as laser fluence, substrate orientation and temperature, and the Ge dots' density per deposited site.

The authors acknowledge financial support from the Canada Foundation for Innovation, and NSERC of Canada. F.R. is grateful to FQRNT and the Canada Research Chairs program for salary support. A.B. acknowledges a FPI fellowship. J.S.R. acknowledges financial support from the AlBan fellowship Program. This work was supported in part by the Spanish Ministerio de Educación y Ciencia through Grant No. MAT2006-02680.

[1] J. Konle, H. Presting, H. Kibbel, K. Thonke, and R. Sauer, Solid-State Electron. **45**, 1921 (2001).
[2] D. L. Harame, S. J. Koester, G. Freeman, P. Cottrel, K. Rim, G. Dehlinger, D. Ahlgren, J. S. Dunn, D. Greenberg, A. Joseph, F. Anderson, J.-S. Rieh, S. A. S. T. Onge, D. Coolbaugh, V. Ramachandran, J. D. Cressler, and S. Subbanna, Appl. Surf. Sci. **224**, 9 (2004).
[3] D. J. Eaglesham and M. Cerullo, Phys. Rev. Lett. **64**, 1943 (1990).
[4] G. Medeiros-Ribeiro, A. M. Bratkovski, T. I. Kamins, D. A. A. Ohlberg, and R. S. Williams, Science **279**, 353 (1998).
[5] F. M. Ross, J. Tersoff, and R. M. Tromp, Phys. Rev. Lett. **80**, 984 (1998).
[6] J. Stangl, V. Holý, and G. Bauer, Rev. Mod. Phys. **76**, 725 (2004).
[7] F. Ratto, G. Costantini, A. Rastelli, O. G. Schmidt, K. Kern, and F. Rosei, J. Exp. Nanosci. **1**, 279 (2006).
[8] J. M. Baribeau, X. Wu, N. L. Rowell, and D. J. Lockwood, J. Phys.: Condens. Matter **18**, R139 (2006).
[9] J. R. Heath, R. S. Williams, J. J. Shiang, S. J. Wind, J. Chu, C. D'Emic, W. Chen, C. L. Stanis, and J. J. Bucchignano, J. Phys. Chem. **100**, 3144 (1996).
[10] T. I. Kamins and R. S. Williams, Appl. Phys. Lett. **71**, 1201 (1997).
[11] E. S. Kim, N. Usami, and Y. Shiraki, Appl. Phys. Lett. **72**, 1617 (1998).
[12] G. Capellini, M. de Seta, C. Spinella, and F. Evangelisti, Appl. Phys. Lett. **82**, 1772 (2003).
[13] A. Karmous, A. Cuenat, A. Ronda, I. Berbezier, S. Atha, and R. Hull, Appl. Phys. Lett. **85**, 6401 (2004).
[14] A. Bernardi, M. I. Alonso, A. R. Goñi, J. O. Ossó, and M. Garriga, Appl. Phys. Lett. **89**, 101921 (2006).
[15] T. I. Kamins, D. A. A. Ohlberg, R. S. Williams, W. Zhang, and S. Y. Chou, Appl. Phys. Lett. **74**, 1773 (1999).
[16] L. Vescan, Mater. Sci. Eng., A **302**, 6 (2001).
[17] O. G. Schmidt, N. Y. Jin-Phillipp, C. Lange, U. Denker, K. Eberl, R. Schreiner, H. Grabeldinger, and H. Schweizer, Appl. Phys. Lett. **77**, 4139 (2000).
[18] G. Jin, J. L. Liu, and K. L. Wang, Appl. Phys. Lett. **76**, 3591 (2000).
[19] Z. Zhong, A. Halilovic, M. Muhlberger, F. Schäffler, and G. Bauer, J. Appl. Phys. **93**, 6258 (2003).
[20] B. Shin, J. P. Leonard, J. W. McCamy, and M. J. Aziz, Appl. Phys. Lett. **87**, 181916 (2005).
[21] M. S. Hegazy and H. E. Elsayed-Ali, J. Appl. Phys. **99**, 054308 (2006).
[22] X. Ma, Z. Yan, B. Yuan, and B. Li, Nanotechnology **16**, 832 (2005).
[23] D. B. Chrisey and G. K. Hubler, *Pulsed Laser Deposition of Thin Films* (Wiley, New York, 1994).
[24] C. V. Cojocaru, C. Harnagea, A. Pignolet, and F. Rosei, IEEE Trans. Nanotechnol. **5**, 470 (2006).
[25] The stencil chip has 14 freestanding membranes, 2 mm in length and 100 μm in width; nominal diameter of the circular apertures is 350 nm and the pitch 700 nm; stencils fabricated at Aquamarijn Filtration, The Netherlands.
[26] Samples were prepared with various Ge thicknesses (coverages). In PLD, the deposited film thickness is controlled by varying the number of laser pulses for a certain target-substrate distance provided that desorption from the substrate is negligible.
[27] A. Bernardi, J. O. Ossó, M. I. Alonso, A. R. Goñi, and M. Garriga, Nanotechnology **17**, 2602 (2006).
[28] Typically 0.4–0.6-nm-thick for Ge on Si(001); Y.-W. Mo, D. E. Savage, B. S. Swartzentruber, and M. G. Lagally, Phys. Rev. Lett. **65**, 1020 (1990).
[29] L. Vescan, T. Stoica, B. Holländer, A. Nassiopoulou, A. Olzierski, I. Raptis, and E. Sutter, Appl. Phys. Lett. **82**, 3517 (2003).
[30] A. Rastelli, M. Stoffel, J. Tersoff, G. S. Kar, and O. G. Schmidt, Phys. Rev. Lett. **95**, 026103 (2005).
[31] For any given set of deposition parameters, the sizes of the dots are fairly narrowly distributed. Their density can be further tuned by using stencils with smaller or larger apertures and varying PLD parameters.

IOP PUBLISHING NANOTECHNOLOGY
Nanotechnology **18** (2007) 475401 (7pp) doi:10.1088/0957-4484/18/47/475401

Evolution of strain and composition during growth and capping of Ge quantum dots with different morphologies

A Bernardi, M I Alonso, J S Reparaz, A R Goñi[1], P D Lacharmoise, J O Ossó[2] and M Garriga

Institut de Ciència de Materials de Barcelona-CSIC, Esfera UAB, 08193 Bellaterra, Spain

E-mail: abernardi@icmab.es

Received 13 July 2007, in final form 26 September 2007
Published 17 October 2007
Online at stacks.iop.org/Nano/18/475401

Abstract
We follow the growth of islands with different shapes by monitoring the strain relaxation by reflection high energy electron diffraction (RHEED). Comparing a bimodal ensemble of pyramids and domes with a monomodal distribution of C-induced domes, we observe different relaxation pathways and a growth mode change from Stranski–Krastanow to Volmer–Weber. We also study the changes induced by the capping process with Si. Small strains in thin cap layers are revealed by spectroscopic ellipsometry. Raman spectroscopy is employed to probe the built-in strain and silicon intermixing in different types of islands, evidencing that smaller islands are enriched in Si and effectively recompressed, whereas bigger relaxed dots remain substantially unaffected.

(Some figures in this article are in colour only in the electronic version)

1. Introduction

The challenge of turning nanostructures like self-assembled quantum dots (QDs) into future nanoscale devices critically depends on the possibility to tailor the island shape, size distribution, composition and strain status [1–3]. In standard Ge/Si heteroepitaxy, 'anomalous' coarsening [4] and Si–Ge intermixing [5] compete as ways for elastic strain relaxation. The typical result is a broad dot-size distribution of coherent islands having different shapes [6–8] (shallow pyramids and steeper domes or barns). For large islands, called superdomes, there is a competition between elastic and plastic relaxation, which depends on the substrate temperature [9–11]. Classifications of island shapes and usual relaxation mechanisms are summarized in [8]. The population of domes and pyramids in an ensemble of islands is related to the total Ge coverage and the growth temperature [12], with bigger pyramids transforming into domes when a critical volume is reached. During annealing, the morphology of strained islands eventually oscillates [8, 13] between shallow and steeper shapes [14] so that the final dot topography is rather unpredictable. The drawback of the coexistence of islands with different shapes is that they are not only inhomogeneous in size but they also exhibit different composition [15] and elastic properties.

To achieve better dot uniformity there are different possible strategies. It is possible to remove large clusters and keep small pyramids by growth interruption and high temperature annealing [16]. In the Ge/Si system pyramids are strongly intermixed and dome-shaped islands with larger aspect ratios and Ge-rich compositions are preferred. In order to obtain small domes, a simple bottom-up strategy involves surface modification by addition of impurities [17–21], which affect the kinetics and alter the energetics of nucleation. Deposition of carbon during the process of QD growth enables a dramatic decrease of the diffusion length of adatoms and a modification of the strain field of the surface. Carbon promotes the growth of domes even at very low Ge coverage and in a wide temperature range [20, 22] without the coexistence of pyramids or hut clusters. The peculiar interplay of chemical interactions between Si, Ge and C and the resulting local enhancement of strain are responsible for

[1] ICREA Research Professor.
[2] Present address: MATGAS 2000 AIE, 08193 Bellaterra, Spain.

relevant changes in the growth mechanism. In addition to better sample homogeneity, size-reduced domes are attractive for the conception of quantum optoelectronic devices [1]. However, we point out that radiative recombination will typically be indirect in real space (type II), suitable for instance for photodetector operation. Type I structures suitable for stimulated emission are possible at even smaller sizes, as was demonstrated from submonolayer Ge QDs [23].

In the present work we describe an experimentally observed growth mode change from Stranski–Krastanow (SK) in the absence of C to Volmer–Weber (VW) when depositing Ge on a C-enriched Si substrate. The evolution of the surface lattice parameter is followed up to large Ge coverage where both elastic and plastic mechanisms of relaxation are active. We also study the process of capping the islands with silicon to understand how it affects the final composition and the elastic recompression of the dots. Finally, we also focus on the structural properties of the cap layer and obtain evidence of the existence of compressive stress induced by local strain fields associated with carbon-rich patches.

2. Experimental details

Samples under investigation were prepared by solid-source molecular beam epitaxy. After oxide desorption at 900 °C and 100 nm thick Si buffer layer deposition, the substrate temperature was set to 500 °C. Subsequently, ∼0.1 monolayers (MLs) of carbon were predeposited on the Si surface from a calibrated sublimation filament. The self-assembling of carbon-induced quantum dots (C-QDs) was achieved by evaporation of 12 MLs of Ge. A reference sample was prepared following exactly the same growth procedure as above, but omitting the step of carbon predeposition. As a result standard Stranski–Krastanow quantum dots (SK QDs) were obtained. Finally, part of the surface of the samples was capped with a 10 nm thick Si layer deposited at 300 °C, in order not to alter the shape of buried dots. Growth was monitored *in situ* by reflection high energy electron diffraction (RHEED) and the island topography was studied *ex situ* by atomic force microscopy. In order to evaluate the composition and residual strain, samples were characterized by optical measurements at room temperature. Raman spectroscopy was carried out with the 514.5 nm line of an Ar-ion laser for excitation. Light was focused onto the sample with a spot size of about 1 μm and a laser power of 4 mW. In order to suppress contributions from second-order processes, we used the scattering geometry $z(xy)\bar{z}$, where x, y and z are the [100], [010] and [001] crystallographic directions, respectively. The ellipsometric spectra were collected using a rotating polarizer ellipsometer in the 1.4–4.8 eV spectral range.

3. Results

3.1. Growth mode and dot topography

When comparing conventional island ensembles with C-induced QDs the first striking feature concerns the morphology. We use the same island shape denominations as those given in [8]. There are two equilibrium island shapes: shallow islands called pyramids (Ps) with {105} crystallographic planes and domes (Ds) with steeper {113} facets. The aspect ratios (defined as the dot height over the square root of the basis area) of these islands are different: pyramids have aspect ratios much smaller than 0.1 and well-developed domes have values around 0.2. The evolution P → D may be rather continuous and the transition islands are called transition domes (TDs), with aspect ratios around 0.15. By changing shapes, islands relax elastically, i.e., Ps and TDs are coherent islands. When TDs evolve into Ds reaching a critical size, plastic relaxation will set in [9, 10] giving rise to larger dome-shaped dislocated islands (superdomes).

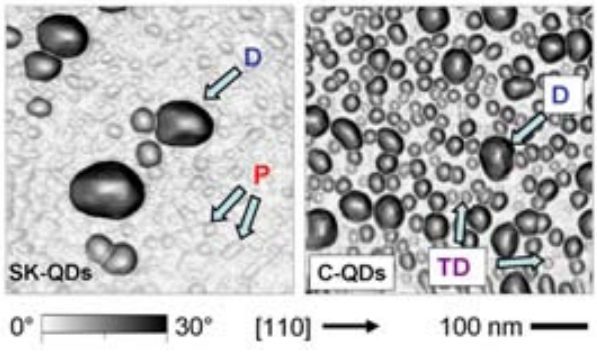

Figure 1. Topographic images of uncapped Stranski–Krastanow quantum dots (SK-QDs) (left) and carbon-induced QDs (C-QDs) (right). The grey scale indicates surface inclination (steeper facets correspond to darker color). Labels in figure refer to pyramids (Ps), transition domes (TDs) and domes (Ds).

We compare the different morphologies in figure 1. We choose a representation with the facet inclination as the z-scale, so that different grey-levels indicate different families of islands. That is, lighter dots are shallow pyramids and darker islands correspond to domes. Ordinary SK self-assembling of Ge islands on Si (left panel) leads to a broad bimodal distribution of pyramids and domes. Addition of carbon to the surface, due to the enhancement of strain fields, stabilizes the dome-shaped islands [24]. In the C-QD ensemble (right panel) even the smaller islands are dome-shaped, with aspect ratios increasing with the dot volume, from ∼0.1 for the smaller or transition domes to ∼0.2 for the bigger domes. It is evident that the use of carbon yields better island homogeneity with a much narrower dot size distribution, although in this example we go beyond optimal coverage on purpose.

In order to unravel the mechanism leading to such different dot topographies, we performed *in situ* RHEED experiments during the growth of the islands. In figure 2 we show the evolution from the streaky pattern of an atomically flat Si(001) surface to the spotty pattern associated with the surface roughening and nucleation of islands. Apart from a qualitative overview of the growth process from RHEED images it is possible to extract streak intensity profiles which allow us to obtain quantitative information [25] about the strain relaxation mechanism. The spacing of diffraction streaks gives the relative variation of the *in-plane* lattice parameter in real time [26–28].

The measured evolution of in-plane lattice parameter is plotted in figure 3. The top panel corresponds to SK self-assembling. In this case, during the first stage of Ge deposition

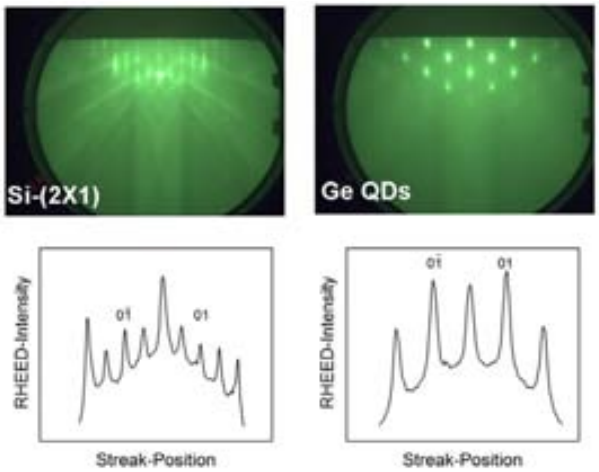

Figure 2. RHEED patterns (top panels) along a ⟨110⟩ azimuth of a flat (2 × 1)-reconstructed Si(001) surface and of transmission diffraction from 3D islands. The bottom panels show the corresponding streak intensity profiles extracted from RHEED images.

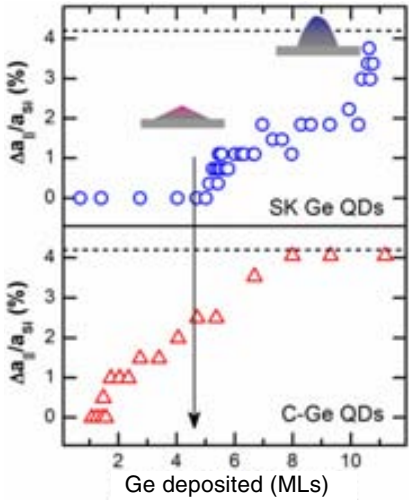

Figure 3. In-plane lattice parameter relaxation associated with the nucleation of 3D islands obtained from RHEED intensity profiles. The vertical arrow indicates the point where dot nucleation for the conventional Stranski–Krastanow islands sets in (top panel).

we do not observe any evolution of the lattice parameter, consistent with the growth of a flat pseudomorphically strained wetting layer (WL). After a critical coverage of 4–5 MLs the streaky pattern starts to evolve into a spotty pattern and from the streak spacing variation we infer a progressive increase of the lattice parameter, which indicates a strain relief associated with the transition from 2D growth to nucleation of 3D clusters. These observations are consistent with the expected Stranski–Krastanow (SK) growth mode. Moreover, from our data we can recognize clearly two stages of strain relaxation. A first plateau around the value $\frac{\Delta a_{\parallel}}{a_{\mathrm{Si}}} \lesssim 1\%$ can be attributed to the nucleation and growth of shallow pyramids, and progressive relaxation up to $\lesssim$2% corresponds to their shape transition into steeper domes [7, 12, 14]. After about 10 MLs of Ge coverage we observe a quicker relaxation, almost reaching the lattice mismatch value for Ge bulk (∼4%). This can be associated with a more efficient plastic strain relief leading to dislocated domes (also called superdomes). At the final coverage of 12 MLs all these islands coexist.

If we now consider the strain relaxation pathway for C-QDs shown in the bottom panel of figure 3, we observe that the lattice parameter starts to evolve from the very early stages of Ge deposition, indicating that 3D relaxation occurs without the formation of a flat strained WL. This strain relaxation dynamics confirms that the presence of C on the surface induces a change of growth mode from Stranski–Krastanow to Volmer–Weber (VW), as previously demonstrated by other RHEED experiments [29, 30] (qualitative study of the streaky–spotty transition) and scanning tunneling microscopy [31]. In our present quantitative RHEED data analysis of C-QDs growth we cannot appreciate sharply differentiated stages of strain relaxation, suggesting that there is no clear shape transition. This observation is consistent with the measured final AFM topography revealing dot homogeneity, without the presence of islands with different shapes. However, the quick lattice relaxation between 6–8 MLs is likely to involve dislocations.

3.2. Recompression of capped islands and Si intermixing

We now turn to discuss the effects of capping with Si, which changes the strain status of the dots [32, 33] and composition [34–36]. Knowledge of the complex strain field generated inside and outside the dots is determinant for predicting the properties of the nanostructures and for engineering the process of piling up a multistack of vertically correlated islands [2, 37, 38]. During capping, the additional strain is partially relieved by Si intermixing into the islands, so that the composition of the island is expected to change towards a Si enrichment [34]. Notice that capping is done here at substrate temperature of 300 °C, which we checked preserves the island shapes.

Raman spectroscopy is a surface sensitive technique useful to extract information about both composition and strain inside the QDs [10, 24, 35, 36, 39–41]. In figure 4(a) we show the Raman spectra for the investigated samples, where the dominant feature is the Ge–Ge phonon band near 300 cm^{-1}. We always observe that the uncapped samples are characterized by weaker peak intensities, possibly due to partial oxidation of the dots and to the presence of surface states that reduce the electronic lifetimes, affecting the resonant enhancement of the Raman intensity. In contrast, in the capped samples, larger Raman intensity close to resonance is possible in the absence of surface states [32]. Moreover, a Si–Ge band at ∼400 cm^{-1}, which was almost absent for uncapped samples (see inset to figure 4(a)), is apparent in the spectra of the capped samples. The relative intensity between Ge–Ge and Si–Ge phonon bands [42, 43] gives at a first glance information on the average composition: uncapped islands are almost pure Ge ($x_{\mathrm{Ge}} > 90\%$), whereas capped islands have a composition ranging from $x_{\mathrm{Ge}} \sim 80\%$ (for SK QDs) to $x_{\mathrm{Ge}} \sim 85\%$ (for C-QDs). The Si intermixing at relatively low temperature is driven by surface diffusion rather than by bulk processes [5, 44, 45], so the reduced adatom mobility associated with the presence of carbon may be the reason why capped C-QDs remain slightly Ge richer.

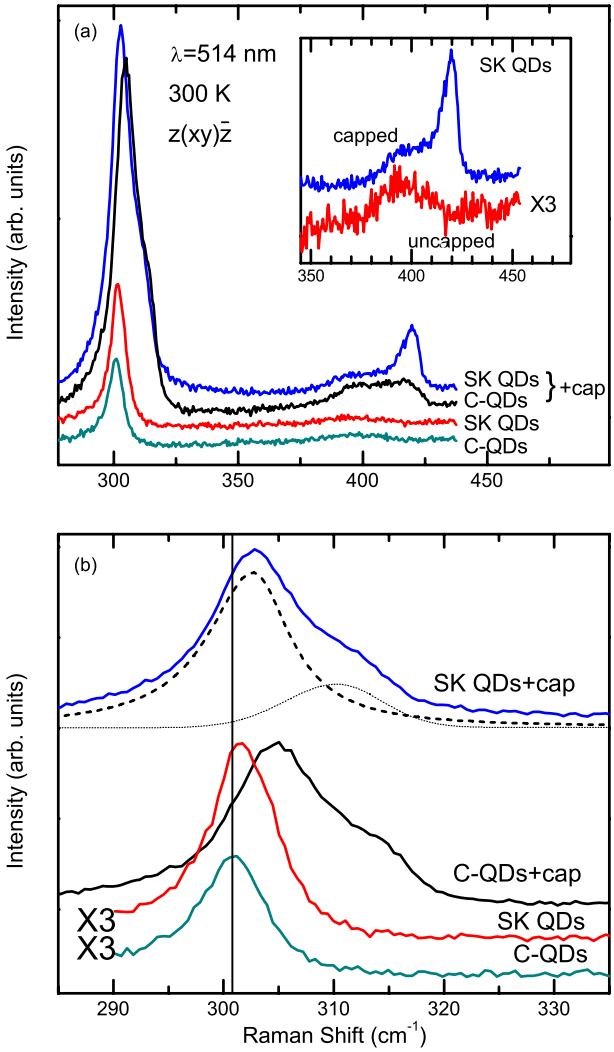

Figure 4. Raman spectra of C-induced and SK QDs for capped and uncapped samples (all with 12 MLs Ge). The inset shows the Si–Ge phonon mode associated with the Si intermixing during the capping process. The bottom panel represents a close-up of the spectra in the region of the Ge–Ge phonon mode. The spectra can be fitted with two asymmetric Gaussians (shown in the figure). The vertical line indicates the Ge–Ge phonon frequency for bulk Ge.

By fitting the peak positions of the phonon bands it is possible to obtain further insight into the nanostructure composition and especially in the strain status. The presence of some dislocated islands does not affect the subsequent analysis, which is completely general. Qualitatively, a red-shift of the Ge–Ge peak is associated with Si enrichment, and a blue-shift is indicative of compressive strain. In figure 4(b) the main Ge–Ge peak is shown with greater detail. The peak position for the Ge–Ge band of uncapped islands (∼301.3 cm^{-1}) is quite close to the frequency expected for relaxed Ge (300.8 cm^{-1}), whereas capped samples are characterized by a blue-shift of the Ge–Ge peak ascribed to the partial recompression of the dots. From figure 4(b) it is remarkable that after capping we are able to resolve two clear contributions to the phonon mode, which can be deconvoluted by fitting two Gaussian terms, giving a low frequency peak at $\omega_{\mathrm{Ge-Ge}} \lesssim 305$ cm^{-1} and a high frequency peak at $\omega_{\mathrm{Ge-Ge}} \gtrsim 310$ cm^{-1}. Similar features observed for nominally monomodal ensembles of dots were recently interpreted as the fingerprints stemming from an intermixed shell and a Ge-rich core, respectively [41]. This core/shell model does not hold for our experiment since the low frequency peak (associated with intermixing during encapsulation of islands) is already present for uncapped dots. Considering the topography of the present samples, we rather ascribe the two contributions to two different families of islands: the high frequency mode is associated with smaller compressed pyramids or transition domes, in the case of the C-QDs, whereas the low frequency peak is mainly related to the bigger relaxed domes with dislocations. Notice in figure 4(a) that the two spectral contributions to the Ge–Ge band can be related to those observed in the Si–Ge band spectral range, namely a lower frequency broad band at ∼390 cm^{-1} and a higher frequency peak at ∼420 cm^{-1}. The observation of two Ge–Ge modes and their two Si–Ge counterparts allows us to solve for values of composition and strain, as detailed below. The only combination that makes sense is to pair both lower frequency peaks (305 and 390 cm^{-1}) and both higher frequency peaks (310 and 420 cm^{-1}). Taking into account the experimental composition dependence for both the Ge–Ge and Si–Ge LO phonon bands [46], we obtain the following system of two equations where the unknowns are the composition x in $Si_{1-x}Ge_x$ and strain $\epsilon_\parallel$ [24, 10]:

$$\omega_{\mathrm{Ge-Ge}} = 284 + 5x + 12x^2 + b_{\mathrm{Ge-Ge}}\epsilon_\parallel, \quad (1)$$

$$\omega_{\mathrm{Si-Ge}} = 400 + 29x - 95x^2 + 213x^3 - 170x^4 + b_{\mathrm{Si-Ge}}\epsilon_\parallel, \quad (2)$$

provided the strain-shift coefficients b of the last terms of equations (1), (2) are known. The generalized expression is

$$b = \omega(x)(-\tilde{K}_{11}\alpha/2 + \tilde{K}_{12}). \quad (3)$$

In equation (3), $\tilde{K}_{ij}$ are the deformation potentials and $\alpha = -\epsilon_\perp/\epsilon_\parallel$ describes the strain field inside the dots. It is generally assumed that the Ge islands are biaxially strained [2] ($\alpha \simeq 0.75$) like a flat pseudomorphic layer, but this approximation might be inaccurate at least for capped dots with steeper facets (domes) that should tend to an hydrostatic strain field ($\alpha = -1$) [33]. Typical experimental values for $b_{\mathrm{Ge-Ge}}$ of $Si_{1-x}Ge_x$ alloys and Ge quantum dots reported in the literature [40, 42, 43, 47] show considerable dispersion, ranging from −400 to −1000 cm^{-1}, remarkably matching the values that can be obtained from equation (3), if we consider the limiting cases of biaxial and hydrostatic strain (assuming that the deformation potentials of Ge are $\tilde{K}_{11} = -1.57$ and $\tilde{K}_{12} = -2.07$)[Note 3]. Since the values of b directly affect the obtained $\epsilon_\parallel$, we conclude that the main source of uncertainty in determining the strain in the dots comes from the lack of consensus in choosing the proper elastic model to describe a compressed island. Therefore, in table 1 we report two results assuming both limiting cases of biaxial and hydrostatic strain fields.

The dot compositions obtained from this detailed analysis and reported in table 1 are compatible with the average compositions determined above from the peak intensity ratio between the Ge–Ge and Si–Ge modes. Uncapped samples consist of Ge-rich islands (∼90%) and are almost fully relaxed.

[3] Our measurement, unpublished.

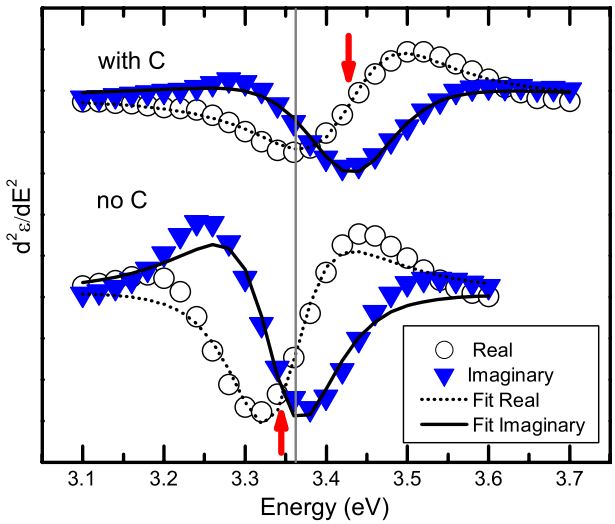

Figure 5. Second derivative with respect to energy of the dielectric function (imaginary and real parts) of the Si cap layer as obtained from the ellipsometry spectra. Arrows represent the fitted energies for the electronic transition E_1. The vertical line shows the E_1 energy for unstrained silicon, and a blue-shift (red-shift) corresponds to compressive (tensile) strain.

Table 1. Composition and strain obtained from the peak positions of the Ge–Ge and Si–Ge phonon modes. For capped samples the results refer to both the high and low frequency contributions to the Raman spectra. We calculate strain assuming both limiting cases of biaxial and hydrostatic strain. In the last column we report as a reference the maximum strain given by the lattice mismatch for each composition.

	x_{Ge} (%)	$\epsilon_{\parallel}^{biaxial}$ (%)	$\epsilon_{\parallel}^{hydrostatic}$ (%)	$\epsilon_{\parallel}^{max}$ (%)
SK QDs	92 ± 2	-1.0	-0.4	-3.7
SK QDs + cap	77 ± 15	-3.0	-1.6	-3.0
	89 ± 3	-1.1	-0.5	-3.5
C-QDs	92 ± 2	-0.8	-0.3	-3.7
C-QDs + cap	82 ± 15	-3.2	-1.9	-3.2
	94 ± 2	-1.3	-0.6	-3.8

After capping, there are two distinct regions showing not only different intermixing but also different strain. This means that some of the islands, presumably the smaller dots, become ∼10% richer in silicon and are strongly compressed. In fact, accepting that strain in small islands is well described by a biaxial model [33], then they turn out to be fully compressed upon capping. In contrast, the family of bigger islands remains Ge rich and only slightly recompressed by the cap layer. Results obtained by Raman spectroscopy confirm that the intermixing process during capping is strain-driven and affects mostly the smaller (Ps and TDs) coherent islands.

3.3. Structural properties of the cap layer

Characterization by spectroscopic ellipsometry, complementing the results from RHEED and Raman, is useful in understanding the inhomogeneity of the strain field of the cap layer in the regions above the islands and in between them [37, 48].

Spectroscopic ellipsometry represents a powerful complementary diagnostic tool allowing one, in particular, to probe the thin layer of silicon covering the islands. From the ellipsometric measurement we determine the thickness of deposited

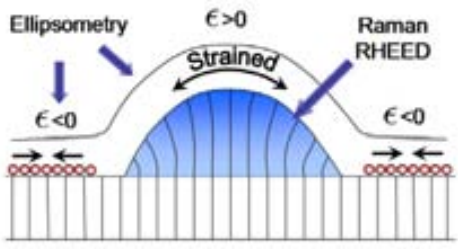

Figure 6. Sketch of the inhomogeneous strain field associated with a C-QD. Relaxed islands induce a tensile strain in the thin cap layer. Nevertheless, the presence of C-rich patches introduces compressive strain in the region of cap layer surrounding the islands.

cap layer and extract its dielectric function with an accurate fitting procedure and inversion algorithm, as discussed elsewhere [10]. By fitting the second derivative spectra of the cap layer dielectric function, we obtain the energy of the E_1 electronic transition [49], indicated by vertical arrows in figure 5. In the reference sample grown without carbon predeposition the E_1 transition is found to be slightly red-shifted compared to bulk Si, indicating the presence of average tensile strain in the cap layer induced by the Ge dots (see the sketch in figure 6). Surprisingly, the E_1 energy for the cap layer deposited on the C-QD sample is blue-shifted, thus reflecting the presence of average compressive strain, in spite of the presence of buried Ge islands which are expected to induce local tensile strain in the overgrown silicon. The structural information obtained by ellipsometry is an areal average of all the sample surface and in contrast to RHEED and Raman measurements does not provide local information related only to the dots. The results indicate that the silicon layer that grows on the C-alloyed surface which surrounds the islands must be compressively strained.

4. Discussion

By using complementary surface science tools we were able to study different aspects of the growth of strained Ge/Si islands. RHEED was used to *in situ* monitor the evolution of the *in-plane* lattice parameter, allowing us to determine the set in of strain relaxation due to nucleation of 3D clusters. In the absence of C, we observed the formation of a flat 2D layer (WL), taking place before the gain in elastic energy becomes dominant over the energetic term associated with the increase of surface (SK growth). In this case, the first stage of island growth accounts for the relaxation of less than 50% of the lattice mismatch and it can be attributed to the nucleation of small and shallow pyramids. When the islands get bigger, they transform into domes or dislocated Ge clusters that can efficiently relax the strain, so that after 10 MLs of coverage we already measure a lattice parameter approaching the value of bulk Ge.

The strain-relaxation pathway changes quite dramatically when carbon is used to engineer the dot topography. In this case, the presence of carbon-rich patches and the repulsive Ge–C interaction prevent the formation of a WL, i.e., it is energetically more convenient to increase the Ge surface with nucleation of 3D clusters, rather than wetting the

carbon-alloyed surface. As a result, the lattice parameter relaxation associated with the 3D nucleation can be observed starting from the very first stages of Ge deposition which is experimental evidence of the growth mode change from Stranski–Krastanow to Volmer–Weber. In the case of C-QDs, we do not observe two regimes of strain relaxation (shallow and steeper islands) but a continuous progressive evolution of the lattice parameter, and this observation is consistent with the AFM topography characterized only by dome-shaped clusters. The density of domes is exceptionally high ($\sim 10^{11}$ cm^{-2}) due to reduced mobility of Ge on a roughened carbon-alloyed surface. Surprisingly, the smaller domes have volumes much below the typical threshold value expected for the pyramid-to-dome shape transition, i.e., the presence of carbon reduces drastically the critical volume associated with the 'anomalous' coarsening. This experimental observation can be accounted for by the enhanced effective mismatch between the substrate and the overlayers [24], without the need to invoke differences of the surface energy between shallower and steeper facets related to the presence of carbon, since the carbon is arranged in patches outside the islands. The reduced surface diffusion that explains the high dot density is likely to be also responsible for the quenching of Si intermixing in the islands. Both island morphology and composition keep evolving while the growth or annealing proceeds. Intermixing dynamics is thought to be dominated by surface rather than bulk diffusion [5, 44], especially at temperatures below 500 °C. Therefore, it is possible that in the presence of C the process of Si intermixing is kinetically limited. Then, capped C-QDs are less intermixed and retain larger strain than SK-QDs, as experimentally observed (see table 1). The limited intermixing as a partial strain-reliever and the presence of local inhomogeneous strain fields are both consistent with the extreme decrease of the critical volume for the pyramid-to-dome transition, to the point where only dome-shaped clusters can be observed.

As a result of the deposition of 12 MLs of Ge, the dots completely relax their strain towards their apex, as can be measured by RHEED probing the topmost atomic layers. Raman spectroscopy becomes a useful tool to study instead the average strain distribution inside the volume of the islands. The relevant question arising when evaluating the Raman results is to decide which is the adequate elastic model to describe the strain status of a quantum dot. Once we have measured the LO phonon frequency shift associated with the lattice deformation, in order to quantify the strain, we need to know the relation existing between the *in-plane* ($\epsilon_{\parallel}$) and *out-of-plane* ($\epsilon_{\perp}$) components. A tiny shallow island is somehow similar to a pseudomorphic 2D layer and its strain status is likely described by a biaxial model (i.e., the lattice is compressed in the *in-plane* direction and it is free to expand in the *out-of-plane* direction, according to Hooke's law). For steeper islands embedded in a matrix (capped dots) [32, 33], the strain status of dots can be rather described by a hydrostatic model ($\epsilon_{\perp} = \epsilon_{\parallel}$). According to the results listed in table 1 the uncapped dots (both SK and C-QDs) retain only between 10% and 30% of the strain, depending on whether we consider a hydrostatic or biaxial model, respectively.

After capping with a 10 nm thick Si layer, the islands are recompressed and we can clearly recognize in Raman spectra features corresponding to two contributions from portions of material with different composition and strain. The experimental piece of evidence is that we are probing regions of material with rather different structural properties; thus, it is unlikely that they refer to different portions of the same island. This argument leads us to ascribe the contributions to two separate families of islands: the smaller coherent islands are fully recompressed (according to the biaxial model) whereas the bigger relaxed domes are less affected by the thin cap layer [33]. Raman spectroscopy turns out to be a powerful technique capable of pointing out the presence of local structural inhomogeneities of the quantum dots, complementing the information achieved by RHEED analysis. When probing dot ensembles most of the characterization tools are sensitive to the 3D clusters due to the grazing incidence geometry and shadowing (this is the case of RHEED) or for confinement of carriers in the islands and the absence of a signal collectable from the WL (like in Raman spectroscopy [24, 40]). In this context, ellipsometry provides unique information on the average strain field of the silicon cap layer, which indicates a local compressive strain in the regions between islands associated with the carbon-rich patches.

5. Conclusions

In summary, we have studied the strain relaxation mechanism during self-assembling of Ge QDs, comparing the conventional Ge/Si heteroepitaxy with the carbon-engineered growth. RHEED analysis permitted us to recognize three stages of strain relaxation after the growth of a pseudomorphic WL, corresponding to the nucleation of pyramids, the shape transition to domes, and dislocation formation. For the sample obtained after pre-depositing carbon on the silicon substrate, we found instead experimental evidence for a growth mode change from Stranski–Krastanow to Volmer–Weber. An ellipsometric study of the silicon cap layer was helpful to point out the presence of compressive strain associated with the local strain field in proximity of the carbon-rich patches in between the islands.

The topography of the quantum dot ensembles was correlated to the structural properties (i.e., strain and composition) measured by Raman spectroscopy. In particular, the capping process put in evidence two distinct regions of the sample with different local composition and elastic properties. We interpreted our experimental results as signals coming from two families of islands, i.e., smaller intermixed dots that get highly recompressed and bigger domes only slightly affected by the deposition of the silicon cap layer.

Optical techniques combined with RHEED and AFM permit one to obtain an overall insight into the growth mechanism of SK and C-QDs, with the possibility to capture features which hint at the local structure of single quantum dots. Nevertheless, in order to unravel the complete accurate picture, single dot spectroscopy or experiments on perfectly monomodal dot ensembles would be required.

Acknowledgments

We are grateful to M S Hegazy for fruitful discussions on RHEED analysis. We acknowledge financial support from the Dirección General de Investigación from Spain under

project MAT2006-02680. AB is also grateful to the Spanish Ministry of Education and Science for a FPI fellowship, JSR acknowledges the Alßan program, and PDL the Spanish Research Council (CSIC) for an I3P fellowship.

References

[1] Baribeau J M, Wu X, Rowell N L and Lockwood D J 2006 *J. Phys.: Condens. Matter* **18** R139
[2] Brunner K 2002 *Rep. Prog. Phys.* **65** 27
[3] Stangl J, Holý V and Bauer G 2004 *Rev. Mod. Phys.* **76** 725
[4] Ross F M, Tersoff J and Tromp R M 1998 *Phys. Rev. Lett.* **80** 984
[5] Ratto F, Costantini G, Rastelli A, Schmidt O G, Kern K and Rosei F 2006 *J. Exp. Nanosci.* **1** 279
[6] Mo Y-W, Savage D E, Swartzentruber B S and Lagally M G 1990 *Phys. Rev. Lett.* **65** 1020
[7] Medeiros-Ribeiro G, Bratkovski A M, Kamins T I, Ohlberg D A A and Williams R S 1998 *Science* **279** 353
[8] Stoffel M, Rastelli A, Stangl J, Merdzhanova T, Bauer G and Schmidt O G 2007 *Phys. Rev.* B **75** 113307
[9] LeGoues F K, Reuter M C, Tersoff J, Hammar M and Tromp R M 1994 *Phys. Rev. Lett.* **73** 300
[10] Alonso M I, de la Calle M, Ossó J O, Garriga M and Goñi A R 2005 *J. Appl. Phys.* **98** 033530
[11] Merdzhanova T, Kiravittaya S, Rastelli A, Stoffel M, Denker U and Schmidt O G 2006 *Phys. Rev. Lett.* **96** 226103
[12] Rudd R E, Briggs G A D, Sutton A P, Medeiros-Ribeiro G and Williams R S 2003 *Phys. Rev. Lett.* **90** 146101
[13] Ledentsov N N, Shchukin V A, Bimberg D, Ustinov V M, Cherkashin N A, Musikhin Y G, Volovik B V, Cirlin G E and Alferov Z I 2001 *Semicond. Sci. Technol.* **16** 502
[14] Rastelli A, Kummer M and von Känel H 2001 *Phys. Rev. Lett.* **87** 256101
[15] Ratto F, Locatelli A, Fontana S, Kharrazi S, Ashtaputre S, Kulkarni S, Heun S and Rosei F 2006 *Small* **2** 401
[16] Ledentsov N N *et al* 2000 *Semicond. Sci. Technol.* **15** 604
[17] Schmidt O G, Lange C, Eberl K, Kienzle O and Ernst F 1997 *Appl. Phys. Lett.* **71** 2340
[18] Beyer A, Muller E, Sigg H, Stutz S, Grutzmacher D, Leifeld O and Ensslin K 2000 *Appl. Phys. Lett.* **77** 3218
[19] Wakayama Y, Gerth G, Werner P, Gösele U and Sokolov L V 2000 *Appl. Phys. Lett.* **77** 2328
[20] Kim J Y, Ihm S H, Seok J H, Lee C H, Lee Y H, Suh E K and Lee H J 2000 *Thin Solid Films* **369** 96
[21] Jernigan G G and Thompson P E 2005 *Thin Solid Films* **472** 16
[22] Wakayama Y, Sokolov L V, Zakharov N, Werner P and Gösele U 2003 *Appl. Surf. Sci.* **216** 419
[23] Makarov A G, Ledentsov N N, Tsatsul'nikov A F, Cirlin G E, Egorov V A, Ustinov V M, Zakharov N D and Werner P 2003 *Semiconductors* **37** 210
[24] Bernardi A, Ossó J O, Alonso M I, Goñi A R and Garriga M 2006 *Nanotechnology* **17** 2602
[25] Wei X H, Li Y R, Zhu J, Zhang Y, Liang Z and Huang W 2005 *J. Phys. D: Appl. Phys.* **38** 4222
[26] Bernardi A, Alonso M I, Goñi A R, Ossó J O and Garriga M 2007 *Surf. Sci.* **601** 2783
[27] Nikiforov A I, Cherepanov V A, Pchelyakov O P, Dvurechenskii A V and Yakimov A I 2000 *Thin Solid Films* **380** 158
[28] Osten H J and Klatt J 1994 *Appl. Phys. Lett.* **65** 630
[29] Dentel D, Bischoff J L, Kubler L, Stoffel M and Castelein G 2003 *J. Appl. Phys.* **93** 5069
[30] Stoffel M, Simon L, Bischoff J L, Aubel D, Kubler L and Castelein G 2000 *Thin Solid Films* **380** 32
[31] Leifeld O, Beyer A, Grutzmacher D and Kern K 2002 *Phys. Rev.* B **66** 125312
[32] Bernardi A, Reparaz J S, Goñi A R, Alonso M I and Garriga M 2007 *Phys. Status Solidi* b **244** 76
[33] Reparaz J S, Bernardi A, Goñi A R, Lacharmoise P D, Alonso M I, Garriga M, Novák J and Vávra I 2007 *Appl. Phys. Lett.* **91** 081914
[34] Lin J H, Yang H B, Qin J, Zhang B, Fan Y L, Yang X J and Jiang Z M 2007 *J. Appl. Phys.* **101** 083528
[35] Baranov A V, Fedorov A V, Perova T S, Moore R A, Yam V, Bouchier D, Thanh V L and Berwick K 2006 *Phys. Rev.* B **73** 075322
[36] Kolobov A V, Morita K, Itoh K M and Haller E E 2002 *Appl. Phys. Lett.* **81** 3855
[37] Tersoff J, Teichert C and Lagally M G 1996 *Phys. Rev. Lett.* **76** 1675
[38] Schmidt O G, Denker U, Christiansen S and Ernst F 2002 *Appl. Phys. Lett.* **81** 2614
[39] Bernardi A, Alonso M I, Goñi A R, Ossó J O and Garriga M 2006 *Appl. Phys. Lett.* **89** 101921
[40] Tan P H, Brunner K, Bougeard D and Abstreiter G 2003 *Phys. Rev.* B **68** 125302
[41] Valakh M Y, Yukhymchuk V, Dzhagan V M, Lytvyn O S, Milekhin A G, Nikiforov A I, Pchelyakov O P, Alsina F and Pascual J 2005 *Nanotechnology* **16** 1464
[42] Tsang J C, Mooney P M, Dacol F and Chu J O 1994 *J. Appl. Phys.* **75** 8098
[43] Volodin V A, Efremov M D, Deryabin A S and Sokolov L V 2006 *Semiconductors* **40** 1314
[44] Leite M S, Medeiros-Ribeiro G, Kamins T I and Williams R S 2007 *Phys. Rev. Lett.* **98** 165901
[45] Katsaros G, Costantini G, Stoffel M, Esteban R, Bittner A M, Rastelli A, Denker U, Schmidt O G and Kern K 2005 *Phys. Rev.* B **72** 195320
[46] Alonso M I and Winer K 1989 *Phys. Rev.* B **39** 10056
[47] Stoehr M, Aubel D, Juillaguet S, Bischoff J, Kubler L, Bolmont D, Hamdani F, Fraisse B and Fourcade R 1996 *Phys. Rev.* B **53** 6923
[48] Marchetti R, Montalenti F, Miglio L, Capellini G, De Seta M and Evangelisti F 2005 *Appl. Phys. Lett.* **87** 261919
[49] See, for instance, Yu P Y and Cardona M 1996 *Fundamentals of Semiconductors* (Berlin: Springer)

Acknowledgments

En primer lugar quiero expresar mi agradecimiento a todos los miembros del grupo de Propiedades Ópticas con los cuales compartí la evolución de mi tesis doctoral ya que de todos ellos aprendí muchas cosas en el transcurso de estos años: Alejandro Goñi, Isabel Alonso, Miquel Garriga, Paul Lacharmoise y Alessandro Bernardi. Quisiera expresar mi agradecimiento por la libertad que se me ha concedido para trabajar, estudiar y pensar, cosa poco frecuente en estos días. También debo mencionar que a nivel personal me he sentido como dentro de una pequeña familia... creo que recordaré por largo tiempo muchas de las cosas ocurridas en estos años!!..gracias a todos por eso. La sensación que resume todo esto es un sentimiento de tristeza al pensar en abandonar el grupo y seguir mi camino...pero bue... la fiesta continúa y el que no baila se lo pierde!!.

En particular quisiera expresar mi profundo agradecimiento a Alejandro Goñi, director de mi Tesis, quien en estos años me enseñó el camino que debe transitarse para ser un buen científico... espero haberlo entendido bien!!.. ;-). No solamente dedicó más que mucho tiempo a enseñarme miles de cosas sino también se ha convertido en el transcurso de estos años en un amigo para mi. Gracias Ale!!!. Solamente lamento muchiiismo tener que dejar el laboratorio porque unos de los placeres mas intensos que disfruté ha sido torturar al Goñi intentando *bandalizar* todos y cada uno de los equipos!!!

Isabel y Miquel. Mucho mas que muchas gracias por estos años, no solo por haberme enseñado muchas cosas sino por la forma en que me trataron a nivel personal, sobre todo por la paciencia que me tuvieron. Lamento mucho que el doctorado termine justo cuando uno empieza a entender algo!!..pero bue...los directores de tesis se llevan la peor parte de la historia...jaa!!!... Viva el pingüino!!....cuac!!..

Paul y Alessandro, compañeros de doctorado con los que compartí muchos buenos momentos en estos años, no solo dentro del laboratorio, sino también en tabernas y *whiskerías* de la región!!!. Gracias a ustedes también. Creo que hemos formado un buen equipo. Recordaré algunas de las discusiones por mucho tiempo.

Finalmente, y a pesar que mis años de doctorado no han sido precisamente fáciles para mí en lo personal, espero haber aportado lo mejor de mí a todos vosotros. Deseo profundamente que el grupo siga creciendo y que ustedes, los jefes, sigan aprendiendo a manejarlo cada vez mejor ya que creo que han comenzado mas que bien generando un grupo que fomenta las ideas y el desarrollo continuo de sus estudiantes.

Gracias a todos!!!